
Ionization and Triggered Star Formation in Turbulent Molecular Clouds

Matthias Gritschneider



München 2009

Ionization and Triggered Star Formation in Turbulent Molecular Clouds

Matthias Gritschneider

Dissertation
an der Fakultät für Physik
der Ludwig–Maximilians–Universität
München

vorgelegt von
Matthias Gritschneider
geb. am 07. August 1978 in München

München, den 11.05.2009

Erstgutachter: Prof. Dr. Andreas Burkert

Zweitgutachter: Prof. Dr. Harald Lesch

Tag der mündlichen Prüfung: 25.06.2009

Contents

Zusammenfassung	xi
1 Introduction	1
1.1 Properties of Molecular Clouds	3
1.2 The Feedback of Massive Stars	5
2 Theoretical Background	9
2.1 Fluid Dynamics	9
2.1.1 Mean Free Path and Relaxation Timescales	9
2.1.2 The Fluid Dynamic Equations	11
2.1.3 Fully Developed Turbulence	13
2.2 Radiative Transfer and Ionization	15
2.2.1 The Radiative Transfer Equation	15
2.2.2 Ionization of a Static Cloud	17
2.3 Evolution of an HII region	22
2.3.1 The Strömgren-Sphere	22
2.3.2 Jump Conditions for Ionization Fronts	23
2.3.3 Expansion of an HII region	24
2.4 Physical Timescales, Heating and Cooling	26
3 Numerical Implementation	29
3.1 The Method SPH	29
3.1.1 Basic Equations	29
3.1.2 Time Stepping and Tree Accuracy	32
3.2 Implementation of Ionizing Radiation	34
3.2.1 Casting of Rays	34
3.2.2 Calculation of the Ionization Degree	35
3.2.3 Equation of State and Modification of the Time-step Criterion	38
4 iVINE - Ionization in the parallel tree/SPH code VINE	39
4.1 Introduction	39
4.2 Numerical Method	41
4.2.1 Prescription of Ionizing Radiation	41

4.2.2	Implementation	43
4.2.3	Modification of the Time-step Criterion	44
4.3	Numerical Tests	45
4.3.1	Ionization without Hydrodynamics	45
4.3.2	Ionization with Hydrodynamics	50
4.3.3	Performance	53
4.4	Radiation Driven Implosion	53
4.4.1	Dynamical Evolution	54
4.4.2	Structure, Collapse Timescales and Final Mass Assembled	55
4.5	Summary and Discussion	59
5	Driving Turbulence and Triggering Star Formation by Ionizing Radiation	61
5.1	Introduction	61
5.2	Initial Conditions	62
5.3	Results	65
5.3.1	Morphology and Formation of Cores	65
5.3.2	Turbulent Evolution	66
5.4	Discussion	68
6	Detailed Numerical Simulations on the Formation of Pillars around HII regions	71
6.1	Introduction	71
6.2	Basic Approach and Initial Conditions	73
6.2.1	Ionizing Radiation	73
6.2.2	Numerical Method and First Tests	75
6.2.3	Initial Conditions	75
6.3	Results of the Parameter Study	78
6.3.1	General Properties	78
6.3.2	Resolution and Boundary Conditions	81
6.3.3	Temperature and Pressure	81
6.3.4	Initial Flux and Density	82
6.3.5	Turbulent Mach Number	84
6.3.6	Turbulent Scale	84
6.3.7	Star Formation	86
6.4	Comparison to Observations	87
6.4.1	General Properties	87
6.4.2	Velocity Field of a Singular Pillar	88
6.5	Discussion	92
7	Conclusions and Outlook	95
	Acknowledgments / Danksagung	105
	Curriculum Vitae	107

List of Figures

1.1	The pillars of creation in the Eagle Nebula (M16)	2
1.2	Molecular clouds - dark and illuminated	3
1.3	The many colors of the Eagle Nebula	4
1.4	Morphology and star formation in M16	5
1.5	The detailed structure of M16 and the complex feedback of Orion	6
2.1	Energy-level diagram of HI	18
3.1	Schematic depiction of the sorting of the particles into the rays	35
4.1	Time evolution of the ionization degree η	47
4.2	Ionization degree η and neutral gas fraction $\chi = 1 - \eta$ versus position	47
4.3	Position of the ionization front versus time	49
4.4	Effect of the refinement on a diagonal density step	50
4.5	Number density versus position for the steady propagation of an ionizing front	52
4.6	Time evolution of the driven collapse of a Bonnor-Ebert sphere	56
4.7	Final stage of the three simulations	58
4.8	Maximum number density versus time for the three simulations	59
5.1	Evolution of the turbulent ISM under the influence of UV-radiation	64
5.2	Evolution of the density weighted power spectra	67
6.1	Front position versus time for the three test simulations with a different flux	76
6.2	Surface density of all simulations of the comparison study	79
6.3	Change of the mean density in the hot gas versus time	83
6.4	Projected surface density along the x-axis for two simulations	85
6.5	Surface density of the most prominent structure	88
6.6	The pillars of creation in M16	89
6.7	Line-of-sight velocities for the z-component	90
6.8	Map of HCO ⁺ profiles over the Dancing Queen Trunk	90
6.9	Line-of-sight velocities for the y-component	91
6.10	Velocity field in the y-z plane.	91

List of Tables

- 4.1 Comparison of analytical and numerical results 52
- 6.1 Listing of the different initial conditions 77
- 6.2 Results of the parameter study 80
- 6.3 Listing of the proto-stellar cores forming 86

Zusammenfassung

Einige der spektakulärsten Beobachtungen unserer Milchstrasse zeigen die filamentären Strukturen in der Umgebung von heissen massereichen O-Sternen. Sobald diese Sterne beginnen zu leuchten, ionisiert ihre ultraviolette Strahlung das umgebende Gas und erzeugt eine heisse HII-Region. Das erhitzte Gas expandiert in die umgebende kalte Molekülwolke. Die dabei entstehende Schockwelle komprimiert das kalte Gas in die auffälligen Strukturen. An den Spitzen dieser Strukturen entstehen neue, masseärmere Sterne. Bis heute ist die präzise Entstehung dieser Regionen nicht vollständig verstanden.

Ziel dieser Arbeit ist die Simulation dieser Entwicklung anhand hydrodynamischer Methoden. Dazu wird ionisierende Strahlung in einen Smoothed Particle Hydrodynamics (SPH) Code namens VINE, der vollständig OpenMP-parallelisiert ist, implementiert. Für die Berechnung der Ionisation wird angenommen, dass die betrachtete Region so weit von dem Stern entfernt ist, dass die Strahlung näherungsweise plan-parallel eintrifft. Zunächst wird die Eintrittsfläche in gleich grosse Strahlen unterteilt. Dann wird die Ionisation entlang dieser Strahlen propagiert. Die neue Implementation ist vollständig parallelisiert und trägt den Namen iVINE.

Zuerst wird anhand mehrerer Tests die Übereinstimmung von iVINE mit bekannten analytischen Lösungen gezeigt. Danach wird der durch Ionisation induzierte gravitative Kollaps einer marginal stabilen Sphäre untersucht. In allen drei simulierten Fällen mit unterschiedlichem einfallenden ionisierenden Fluss kollabiert die Sphäre. Zusätzlich kann die beobachtete Tendenz, dass jüngere Sterne weiter entfernt von der Quelle der Ionisation entstehen, bestätigt werden.

Desweiteren werden Simulationen über den Einfluss ionisierender Strahlung auf turbulente Molekülwolken durchgeführt. Hier zeigt sich, dass die beobachteten, komplexen Strukturen durch die Kombination von Ionisation, Hydrodynamik und Gravitation reproduziert werden können. An den Spitzen der Strukturen wird das Gas stark komprimiert und kollabiert unter dem Einfluss seiner Eigengravitation, genau wie beobachtet. Gleichzeitig treibt die ionisierende Strahlung die Turbulenz im kalten Gas weit stärker als bisher angenommen. Anhand von einer Parameterstudie folgt, dass die entstehenden Strukturen kritisch von dem jeweiligen Anfangsstadium der Wolke zur Zeit der Zündung des O-Sterns abhängen. Dies ergibt die einmalige Gelegenheit, zusätzliche Informationen über Molekülwolken, die ansonsten schwierig zu beobachten sind, in den von O-Sternen stark illuminierten Regionen zu erhalten.

Die Implementation ionisierender Strahlung im Rahmen dieser Doktorarbeit ermöglicht die Untersuchung der Einwirkung massereicher Sterne auf ihre Umgebung in bislang unerreichter Genauigkeit. Die durchgeführten Simulationen vertiefen unser Verständnis der Wechselwirkung von Turbulenz und Gravitation im Rahmen der Sternentstehung. Weitere erstrebenswerte Schritte wären die genauere Berücksichtigung der Kühlprozesse innerhalb der Molekülwolke und die Implementation der Winde massereicher O-Sterne.

Chapter 1

Introduction

O type stars are the most massive stars in the present day universe. Their masses exceed $40M_{\odot}$ and their surface temperature is higher than 3×10^4 K. Like other stars they form in molecular clouds (MCs). Due to their high temperature and mass the feedback of O stars substantially affects the parental cloud. On small scales, stellar winds are driven into the MC by radiation pressure on the resonance absorption lines of heavy elements. In addition, the high temperature surface of O stars emits ultraviolet (UV) radiation that ionizes the surrounding gas, creating a so called HII region with gas at temperatures of 10^4 K. By these two feedback mechanisms some of the most fascinating observed structures in the interstellar medium (ISM) are formed. Among the most famous observations of the peculiar structures surrounding HII regions are the Horsehead nebula (B33) and the pillars of creation in M16 (see Fig. 1.1). All these regions share a common head to tail structure with the head pointing towards the source of ionization. Within the tips, star formation is frequently detected. This secondary generation of stars is likely to be triggered by the massive star.

HII regions provide a fascinating tool to understand the intriguing properties of the ISM. This is due to the fact that the MCs at the border of HII regions are highly illuminated and lend themselves much easier to observations than quiescent MCs. Furthermore, if the intrinsic properties of the parental MCs determine the size and fundamental properties of the forming pillars they work as a kind of magnifying glass on the initial stage of a MCs. In addition, a wealth of infrared observations on cores and stars forming in almost any observed pillar-like structure has become available since the launch of the Spitzer Space Telescope. However, a full theoretical understanding of the formation of these regions and the stars within, as well as the efficiency and mass range of triggered star formation is still missing. Thus, it is the aim of this work to implement ionizing radiation into a hydrodynamical code and perform simulations to further our understanding of this peculiar regions.

The formal structure of this cumulative thesis is as follows. In chapter 1, the most important observations of MCs and HII regions are reviewed. Chapter 2 gives the underlying physical foundation for the treatment of MCs, a derivation of the equations of fluid dynamics and a short review of fully evolved turbulence. In addition, the equations of radiative transfer are deduced and the evolution of an HII region is outlined. The chapter is concluded by a short review of the important physical timescales involved. In chapter 3 we present iVINE, the implementation of

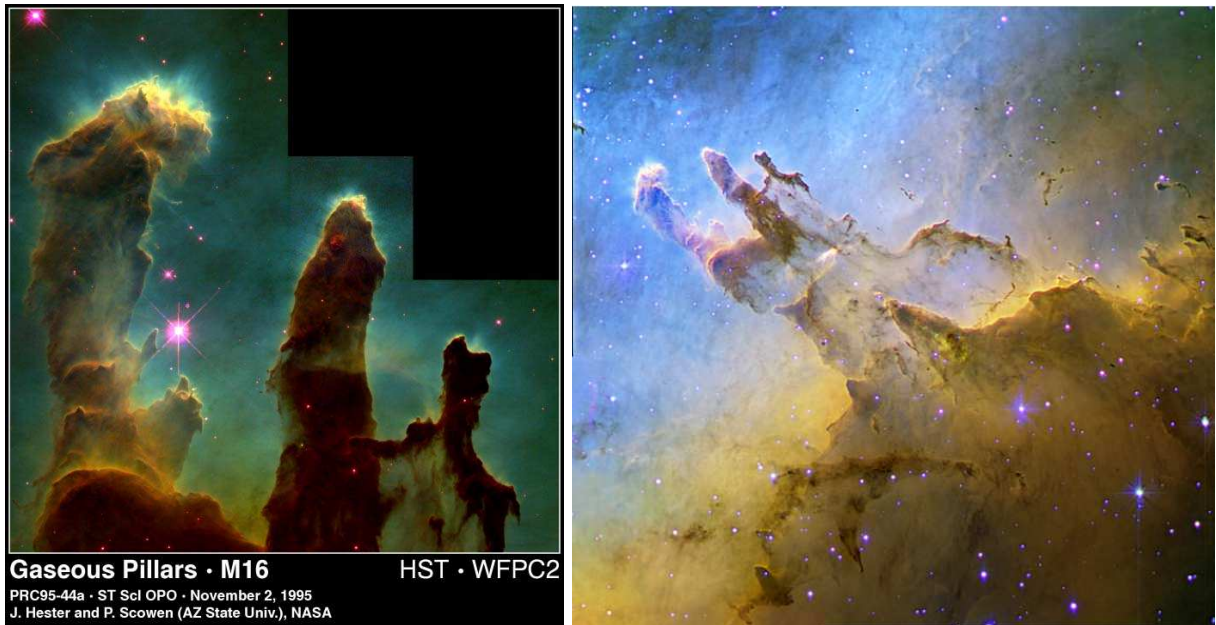


Figure 1.1: The pillars of creation in the Eagle Nebula (M16). Left: The famous Hubble Space Telescope (HST) image in the optical band. Image credit: J. Hester & P. Scowen, NASA. Right: A greater subset of the region. The high amount of detail results from combining the lines of $H\alpha$ (green), $[OIII]$ (blue) and $[SII]$ (red). Image credit: Daniel Lopez, IAC.

ionizing radiation into the tree/SPH-code VINE. First, the basic concepts of SPH are reviewed. We then go on to explain the ray-shooting algorithm and the iteration of the ionization degree in detail. Chapter 4 is the first publication¹, focusing on the implementation and numerical tests of the new code iVINE. In addition, first results on the radiation driven implosion of preexisting, marginally stable spheres into gravitational collapse are presented. In chapter 5 we present the second paper². Here, a part of a turbulent MC is ionized. The ionization acts as a small-scale driver of turbulence. Furthermore, the resulting morphology is remarkably similar to the observed structures. The third paper³, presented in chapter 6, follows this ansatz. An entire parameter study is performed, which enables us to disentangle the influence of different initial conditions on the shape of the structures forming. Besides, core formation is detected frequently in several simulations with the properties of the cores matching the observations. Finally, in chapter 7 the conclusions are drawn and a short outlook is given.

¹Gritschneider et al. (2009a)

²Gritschneider et al. (2009b)

³Gritschneider et al. (2009c, to be submitted)

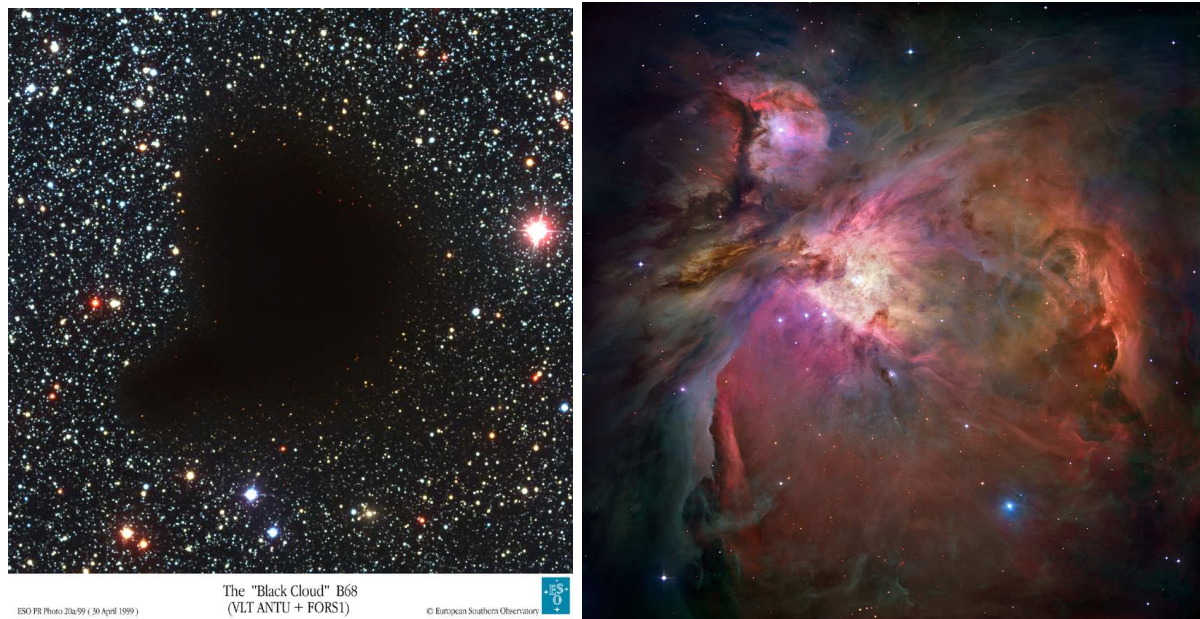


Figure 1.2: Molecular clouds - dark and illuminated. Left: VLT image of Barnard 68, a dark MC of ≈ 0.5 pc diameter which absorbs almost all background light in the optical band. Image credit: FORS Team, 8.2-meter VLT Antu, ESO. Right: Combined HST/LaSilla optical image of a subsection of the Orion Nebula (M42), a MC of ≈ 10 pc diameter. The border of this cloud is illuminated by newly formed stars. Image credit: NASA, ESA, M. Robberto (STScI/ESA).

1.1 Properties of Molecular Clouds

Molecular clouds (MCs) are the birthplace of stars. They are observed on a wide range of scales. The most massive giant MCs have masses of up to $10^6 M_{\odot}$ and sizes of 10-60 pc. They are rather cold (10-100 K) and have average densities of 10^2 - 10^3 cm^{-3} . At these temperatures and densities the formation of molecules, mainly molecular hydrogen (H_2), is possible, which gives these clouds their name. From an observational point of view, H_2 is hard to observe. It has no permanent dipole moment, its rotational transitions are weak and even its low level excitation states are at mid-infrared wavelength, which can not be excited by collisions at the temperatures present in MCs. Thus, often tracers, such as the CO-molecule are used. Since a constant ratio of CO to H over the entire cloud may be doubtful, this does not give certain mass estimates. A more stable tracer of molecular gas seems to be dust, as the gas-to-dust ratio (100:1) is rather constant. The best measurements are provided by dust absorption or scattering, since these processes are independent of the dust temperature. These measurements of course need some source, e.g. star light to absorb or scatter. The contrast between Barnard 68, a dark cloud with no star formation detected, and the Orion Nebula, which is illuminated by stars forming at the border, is depicted in Fig. 1.2. Furthermore, observations in more than two wavelengths are desirable to get different tracers for accurate column density measurements (see e.g. Lombardi & Alves, 2001). A sample of the Spitzer observations of M16 in several wavelengths is included in Fig. 1.3.

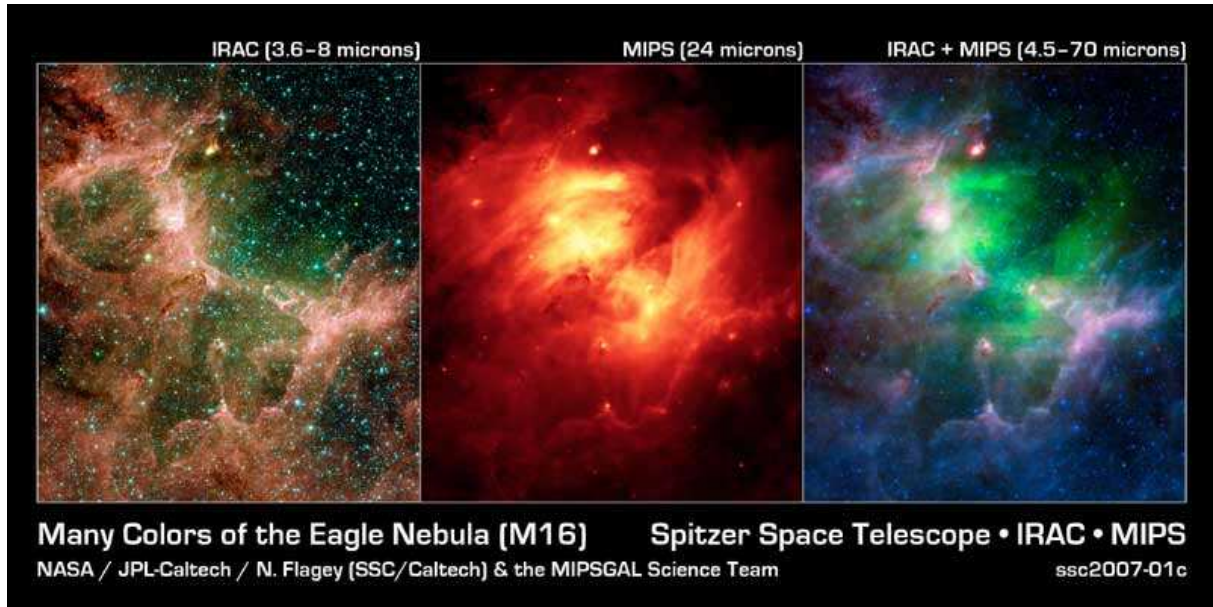


Figure 1.3: The Eagle Nebula (M16) in different infrared bands by the Spitzer Space Telescope. Again, the three pillars are visible close to the center of each picture. Left: Dust and stars in small IR-bands. Middle: Dust temperature. The hot dust, depicted in yellow is aligned in a shell-like structure. Right: Composite image, the dusty cloud surrounds the heated dust (now depicted in green). Image credit: NASA/JPL-Caltech/N. Flagey/MIPSGAL Science Team.

The observations reveal that MCs are highly turbulent structures. Their velocity dispersion σ scales with the cloud size L similar to $\sigma \propto L^{1/3}$, the scaling implied by ideal, incompressible turbulence (see §2.1.3, Kolmogorov 1941). This is called Larson’s scaling relation (Larson, 1981). Similar laws apply for the cloud’s mass and the mean density. The clouds appear to be turbulent on scales from the size of the cloud down to molecular cloud cores (Mac Low & Klessen, 2004). At the length scales of cores, the turbulence is roughly at the transonic point and in these more quiescent, dense regions stars are born. Estimates for the internal velocity dispersion are deduced from the width of molecular lines and are in the range of a few km s^{-1} (see e.g. Gahm et al., 2006). As the local sound-speed in the cold clouds is only $\approx 0.2 \text{ km s}^{-1}$ this corresponds to turbulence at levels of Mach 5-20. Models of supersonic turbulence are indeed able to reproduce the highly filamentary and self-similar nature of MCs quite well (see e.g. Padoan & Nordlund, 1999). However, it remains still puzzling how the turbulence can be kept at such a high level during the entire lifetime of a MC. This is still a matter of ongoing debate.

For a long time MCs were believed to be long-lived equilibrium structures with lifetimes of $\approx 100 \text{ Myr}$. Since they would be stabilized by magnetic fields, stars would form by ambipolar diffusion during the entire lifetime of the cloud. However, observations of the small stellar age spread in MCs ($< 1 \text{ Myr}$, see e.g. Hillenbrand 1997) challenged this scenario. So the paradigm changed within the past years towards a much more dynamic picture. MCs are now believed to be transient features assembled by large scale flows, which are bound by pressure rather than by self-gravity (Ballesteros-Paredes et al., 1999). These flows originate in supersonic turbulence, most

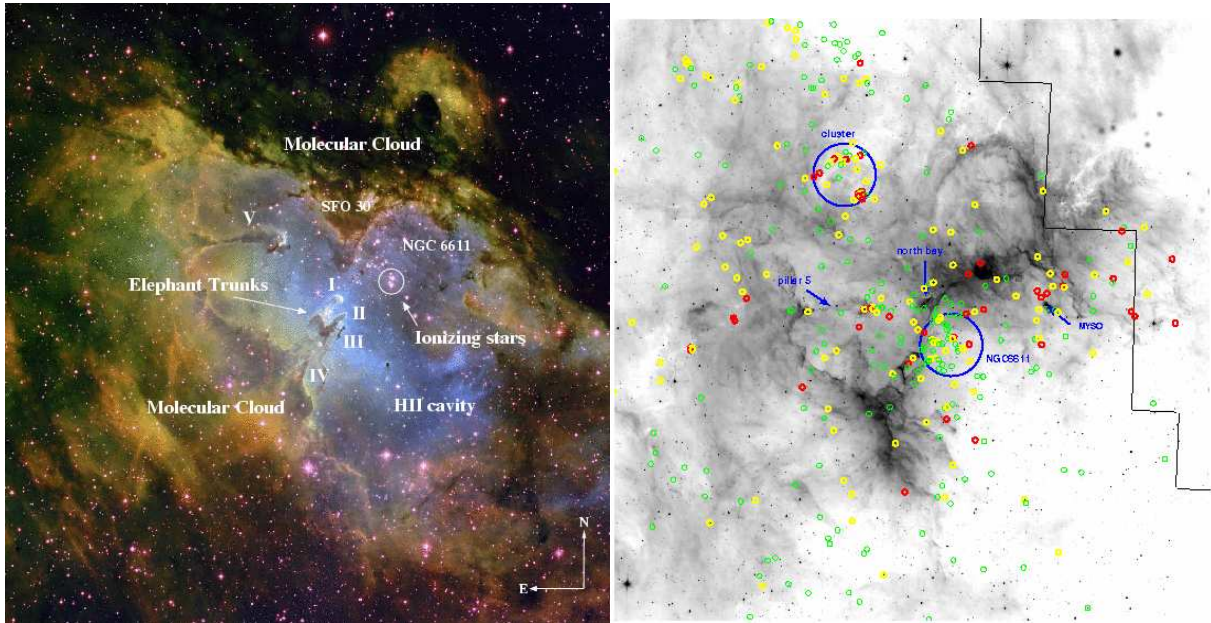


Figure 1.4: Left: The morphology of the entire HII region in M16. Combined picture of $H\alpha$ (green), $[OIII]$ (blue) and $[SII]$ (red). Image credit: T. A. Rector & B. A. Wolpa, NOAO, AURA. Right: Star formation in M16 from Indebetouw et al. (2007). Sources with massive accretion disks are yellow, and those that in addition likely have massive envelopes are red. Candidates where the circumstellar mass can not be strongly constrained are green (Indebetouw et al., 2007).

likely driven by a mixture of galactic rotation and supernovae (Mac Low & Klessen, 2004). The balance of turbulence and gravity then determines the local star formation efficiency. In addition, the observed, strong turbulence would have to be present for a much shorter time. Besides, the small stellar age gradient and the lack of Post-TTauri stars with an age $> 10\text{Myr}$ indicate that MCs are destroyed after 5 – 10Myr. Three possible processes should play a major role here. First, the feedback of the stars formed can tear the parental cloud apart (Matzner, 2002). Second, the cloud can simply disperse after the initial compression. This process is quite slow, as the dispersion should happen roughly at the sound-speed of the cold gas. Third, the cloud may be disrupted by the turbulent flows that formed it previously. Most likely the disruption is caused by a combination of all three processes.

1.2 The Feedback of Massive Stars

As soon as a MC has formed, massive O stars will exert their feedback onto the parental MCs, likely triggering or speeding up the subsequent formation of smaller stars. For a very recent review of the Eagle Nebula see Oliveira (2008). As it is already visible in Fig. 1.3 the situation is highly complex. In the center, there is a hot HII region, consisting mainly of ionized hydrogen. In these regions the observed number densities of the hot gas and the electrons are of the order of

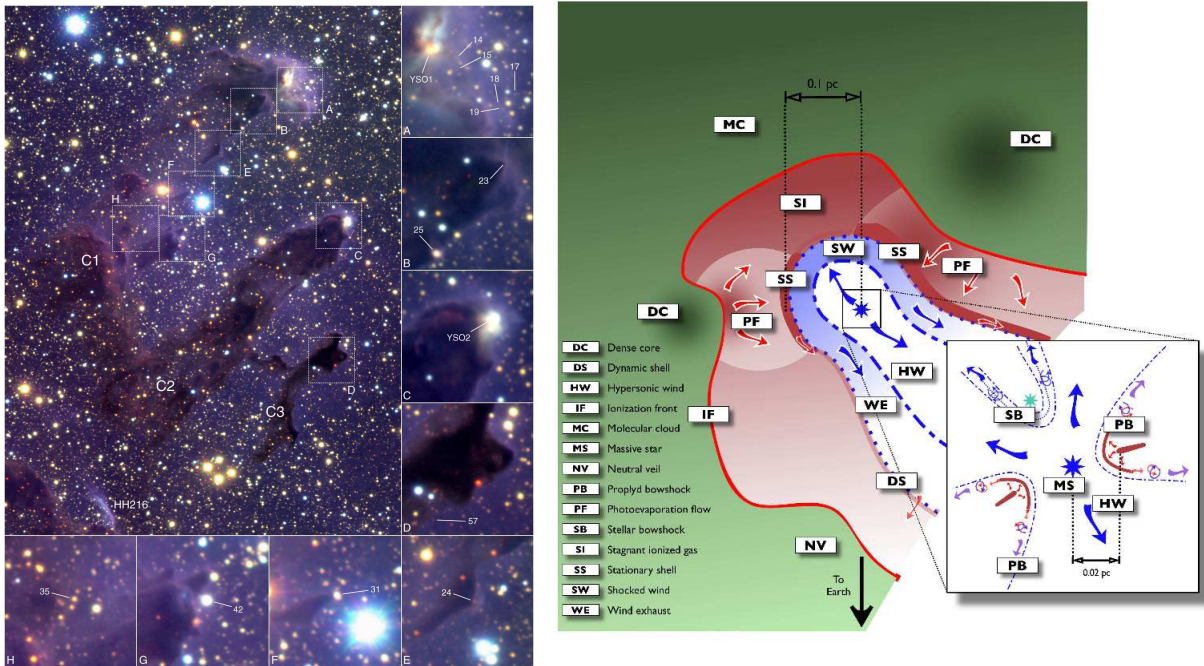


Figure 1.5: Left: True color near-IR image of the pillars in M16 obtained by McCaughrean & Andersen (2002) with ISAAC at the ESO/VLT. JHK images are shown as blue, green and red, respectively. It is clearly visible, that most of the molecular gas is at the tips of the structures. The insets show detailed clumps and young stellar objects. Right: The three-dimensional dynamic structure of the inner Orion nebula as deduced from observations by O’Dell et al. (2009)

$n_e = n_{\text{hot}} \approx 50 \text{ cm}^{-3}$ (see e.g. Lefloch et al., 2002). The adjacent structures are filamentary and up to two orders of magnitude denser than the average in MCs. Fig. 1.4 depicts the morphology of the entire HII region in M16. Besides the three famous pillars I-III, there are several other structures visible. The tips of the pillars contain $10 - 60 M_{\odot}$, which corresponds to approximately 55 – 80% of the total mass of each pillar. This head-to-tail structure can clearly be seen in Fig. 1.5 (left column). Inside each pillar, several denser cores are visible, with star formation detected frequently at the tips (e.g. Sugitani et al., 2002). Recent observations have revealed a high amount of young stellar objects in M16 (see Fig. 1.4, right column). The observations are discussed in more detail in the publications (§4-§6).

There are two main feedback processes. First, the ionizing radiation will heat the surrounding gas, thereby driving shocks in the cold MC. Second, the radiation pressure on the resonance absorption lines of heavy elements will drive stellar winds into the MC. Up to now, it is still unclear which of the two processes will be more effective. The complex situation in the Orion Nebula is shown in Fig. 1.5 (right column). In principle, the ionization should reach fast into the cloud with the speed of light. After the Strömgen radius, given by the volume which can be immediately ionized by the UV-radiation, is reached, this rapid phase ends and the further evolution is dominated by the hydrodynamic evolution with the sound-speed of the hot gas. Now

stellar winds, which can reach velocities of up to 10^3 km s^{-1} , may catch up with the ionization front. However, these velocities are supersonic even with respect to the hot gas at a sound-speed of $\approx 12 \text{ km s}^{-1}$. Therefore shocks can evolve in the hot, ionized region. Then, radiation and ionization and winds would either drive a shock front together or one shock front might overtake the other. Both can be seen in Fig. 1.5 (right column). Here, on the left hand side of the star the evolution is dominated by the ionization and a stagnating wind-shock closer to the star. On the right hand side, the ionization and the winds are streaming away freely. This might either be due to a combined front as described before or simply due to the lack of molecular gas at this side of the star. Up to now, it is still not fully understood if winds can be driven in high density regions. If not, it would be necessary to arrive at lower densities by the ionization and the onset of stellar winds would be delayed. Furthermore, the effectivity of the driving of winds depends crucially on the metallicity in the parental MC. Altogether, the situation is so complex, that it can only be understood by numerical simulations. In this thesis, we focus on the effect of ionizing radiation, neglecting the effect of stellar winds. Basically, we place our simulations in the purely ionized region between the stationary shell and the cold MC in Fig. 1.5 (right column).

Chapter 2

Theoretical Background

In this chapter, the physical foundations for the treatment of HII regions are given. We first deduce the basics of fluid dynamics. Then, the equations of radiative transfer and the treatment for the ionization of a static cloud are derived. After that, we expand this solutions to a dynamical HII region. In the end, the relevant physical timescales involved are discussed.

2.1 Fluid Dynamics

First, we show that a molecular cloud (MC) can be treated by the means of fluid dynamics. We then derive the Euler equations. This section is concluded by a prescription of fully evolved turbulence.

2.1.1 Mean Free Path and Relaxation Timescales

In order to describe MCs it is first necessary to determine under which conditions a gas can be treated as a continuum. This is only valid if the mean free path is much smaller than the size of the cloud looked at. If the scales are comparable, scattering has to be taken into account (as e.g. in the dynamic motion of stars in clusters).

For neutral atoms and molecules the mean free path ℓ is given by

$$\ell = \frac{1}{\sigma n}, \quad (2.1)$$

with σ as the average cross section for particle-particle scattering and n as the mean number density of the cloud (see e.g. Shu, 1991b). Typically $\sigma = 1 \times 10^{-15} \text{ cm}^2$ for proton-proton collisions. For a cloud at a density of $n = 100 \text{ cm}^{-3}$ the mean free path is therefore $\ell = 10^{14} \text{ cm}$, which is several orders of magnitude lower than the size of a MC.

For charged particles the cross-section σ is infinity due to infinite range of the coulomb force. Nevertheless, it is possible to estimate the sphere of influence in which the electrostatic energy is comparable to the kinetic energy of thermal electrons by defining an effective radius:

$$\frac{e^2}{r_{\text{eff}}} \propto kT, \quad (2.2)$$

where e is the elemental charge, k is the Boltzmann constant and T the electron temperature. Thus, the cross section for this estimate is $\sigma_e = \pi r_{\text{eff}}^2$ and the mean free path can be written as

$$\ell \propto \frac{1}{n_e \pi r_{\text{eff}}^2} \propto \frac{kT}{n_e e^4}. \quad (2.3)$$

For the ionized, hot gas in an HII region the electron density is typically $n_e = 50 \text{ cm}^{-3}$ and the temperature $T_{\text{hot}} = 10^4 \text{ K}$. With these values, the mean free path is $\ell \approx 10^{12} \text{ cm}$. The relaxation time for electrons to acquire a Maxwellian distribution is

$$t_{\text{rel}}(e - e) \propto \frac{\ell}{c_{s,e}} \propto \frac{m_e^{1/2} (kT)^{3/2}}{n_e e^4}. \quad (2.4)$$

For a more sophisticated treatment including the self-shielding of charged particles see e.g. Spitzer (1962). Here, the electric potential of an ion attract electrons and repulses ions. From a statistical point of view the potential gets cut off by an exponential factor at large radii. This factor is determined by the Debye length L_D , which is given by

$$L_D = \sqrt{\frac{kT}{4\pi e^2 (n_e + n_p)}} \quad (2.5)$$

for a plasma consisting of purely electrons and protons. The precise expression for Eq. 2.4 is then

$$t_{\text{rel}}(e - e) = \left(\frac{0.290}{\ln \Lambda} \right) \left(\frac{m_e^{1/2} (kT)^{3/2}}{n_e e^4} \right), \quad (2.6)$$

where $\ln \Lambda = 3L_D/r_{\text{eff}}$. From this equation it follows directly that the relaxation time for protons at the same number density is

$$t_{\text{rel}}(p - p) = \left(\frac{m_p}{m_e} \right)^{\frac{1}{2}} t_{\text{rel}}(e - e). \quad (2.7)$$

In addition, Spitzer (1962) shows that the timescale until electrons and protons reach the same temperature is given by

$$t_{\text{rel}}(e - p) = \left(\frac{m_p}{m_e} \right) t_{\text{rel}}(e - e). \quad (2.8)$$

For a fully ionized HII region with $n_e = n_p = 50 \text{ cm}^{-3}$ this timescales are of the order 10^{-6} yr , 10^{-4} yr and 10^{-2} yr , respectively. The mean free path for the collision of two electrons is according to the more precise treatment $l \approx 10^{10} \text{ cm}$.

The estimates of the mean free path for neutral and charged particles show that it is valid to treat the cold gas of MCs as well as the hot gas in HII regions as a continuum by the means of fluid dynamics. Besides, the short relaxation timescales allows to assume that the distribution of particles will locally be Maxwellian and can always be described by a kinetic temperature T .

2.1.2 The Fluid Dynamic Equations

As shown in the previous section, the motions of gas inside MCs and HII regions can be described by the equations of fluid dynamics. In general, there are two approaches to calculate the motions of a fluid. On the one hand, there is the Eulerian description, where the physical quantities are treated as functions of the time t at fixed positions \mathbf{x} . On the other hand, there is the Lagrangian prescription where the dynamics are calculated by following the motions of a fluid element. The transition from a Lagrangian to an Eulerian prescription is formally given by the change from the total differential to the partial differentials:

$$\frac{d}{dt} = \frac{\partial}{\partial t} + \frac{\partial \mathbf{x}}{\partial t} \cdot \frac{\partial}{\partial \mathbf{x}} = \frac{\partial}{\partial t} + \mathbf{u} \cdot \nabla. \quad (2.9)$$

Since it is more common, the equations are derived for the Eulerian prescription and will be transformed into a Lagrangian prescription in §3 as SPH, the numerical method used, is Lagrangian. For the derivation, we follow the approach outlined by Shu (1991b). We first motivate the Boltzmann equation (which is also used in §2.2.1) and then derive the Euler equations from it.

The Hamiltonian H of a gas particle with the mass m and phase-space coordinates (\mathbf{x}, \mathbf{p}) can be split in a smoothly varying part and a part containing irregular variations, e.g. collisions:

$$H = H_{\text{smooth}} + H_{\text{irr}}. \quad (2.10)$$

In addition, we can define the distribution function $f(\mathbf{x}, \mathbf{p}, t)$ in a way that the number of atoms or molecules inside a phase space element is

$$f(\mathbf{x}, \mathbf{p}, t) d\mathbf{x} d\mathbf{p}. \quad (2.11)$$

The smooth part of the Hamiltonian requires that

$$f(\mathbf{x}, \mathbf{p}, t) d\mathbf{x} d\mathbf{p} = f(\mathbf{x} + \mathbf{u} dt, \mathbf{p} + \mathbf{F} dt, t + dt) d\mathbf{x} d\mathbf{p}, \quad (2.12)$$

i.e. that all particles at a time t at a position \mathbf{x} with a momentum \mathbf{p} experiencing an external force \mathbf{F} will be at $\mathbf{x} + \mathbf{u} dt$ with a momentum $\mathbf{p} + \mathbf{F} dt$ at the time $t + dt$. Taking the irregular part of the Hamiltonian into account leads to

$$f(\mathbf{x} + \frac{\mathbf{p}}{m} dt, \mathbf{p} + \mathbf{F} dt, t + dt) d\mathbf{x} d\mathbf{p} - f(\mathbf{x}, \mathbf{p}, t) d\mathbf{x} d\mathbf{p} = \left(\frac{\partial f}{\partial t} \right)_{\text{col}} d\mathbf{x} d\mathbf{p} dt. \quad (2.13)$$

Dividing by $d\mathbf{x} d\mathbf{p} dt$ and then taking the limit gives

$$\frac{\partial f}{\partial t} + \frac{\partial f}{\partial \mathbf{x}} \cdot \frac{\mathbf{p}}{m} + \frac{\partial f}{\partial \mathbf{p}} \cdot \mathbf{F} = \left(\frac{\partial f}{\partial t} \right)_{\text{col}}, \quad (2.14)$$

the so called Boltzmann Equation.

To derive equations for the physical evolution of a fluid we multiply Eq. 2.14 by a function $\varphi(\mathbf{v})$ which is any polynomial of \mathbf{v} and then integrate over all possible \mathbf{v} :

$$\int \left[\varphi \frac{\partial f}{\partial t} + \varphi \mathbf{v} \cdot \frac{\partial f}{\partial \mathbf{x}} + \varphi \mathbf{F} \cdot \frac{\partial f}{\partial \mathbf{p}} \right] d\mathbf{v} = \int \varphi \left(\frac{\partial f}{\partial t} \right)_{\text{col}} d\mathbf{v}. \quad (2.15)$$

If the dimension of the fluid element L is much larger than the mean free path ℓ (see §2.1.1), there are exact five conserved quantities φ : the mass, momentum and energy of a particle

$$\varphi = m, \quad \varphi = m\mathbf{v}, \quad \varphi = m|\mathbf{v}|^2. \quad (2.16)$$

For these, the collisional term can not contribute to the rate of change and thus

$$\int \varphi \left(\frac{\partial f}{\partial t} \right)_{\text{col}} d\mathbf{v} = 0. \quad (2.17)$$

Taking this into account and defining

$$\langle \varphi \rangle = \frac{1}{n} \int \varphi d\mathbf{v}, \quad (2.18)$$

with $n = \int d\mathbf{v}$ as number density of the gas (cf Eq. 2.11) we can derive from Eq. 2.15

$$\frac{\partial}{\partial t} (n\langle \varphi \rangle) + \frac{\partial}{\partial \mathbf{x}} \cdot (n\langle \mathbf{v}\varphi \rangle) + n\mathbf{F} \cdot \left\langle \frac{\partial \varphi}{\partial \mathbf{v}} \right\rangle = 0 \quad (2.19)$$

since the derivatives in t and \mathbf{x} can be exchanged with the integration in \mathbf{v} .¹

For the mass conservation $\varphi = m$ and by defining $\rho = nm$ as the mass density and $\mathbf{u} = \langle \mathbf{v} \rangle$ as the mean velocity of the fluid element Eq. 2.19 yields

$$\frac{\partial \rho}{\partial t} + \frac{\partial}{\partial \mathbf{x}} \cdot (\rho \mathbf{u}) = \frac{\partial \rho}{\partial t} + \nabla \cdot (\rho \mathbf{u}) = 0, \quad (2.20)$$

which is the continuity equation. In other words, the decrease in mass per unit time must be equal to the out-streaming mass. Inserting the other conserved quantities, momentum and energy into Eq. 2.19 leads to a set of four linear independent equations for twelve independent variables, since the higher order terms lead to tensors (e.g. $\nabla(\rho \langle \mathbf{v} \cdot \mathbf{v} \rangle)$ leads to a viscous stress tensor).

To solve this problem a closure relation is needed. In an approximation we can expand the distribution function as

$$f = f_0 + \delta f_1 + \delta^2 f_2 + \dots \quad (2.21)$$

with

$$\delta = \frac{\ell}{L}. \quad (2.22)$$

¹To derive the third term the divergence theorem has to be used and the assumption that f vanishes faster than any power of \mathbf{v} for $\mathbf{v} \rightarrow \infty$ on the thereby created surface.

This is the so called Chapman-Enskog procedure, for a full treatment see Lifshitz & Pitaevskii (1981). As $\delta \ll 1$ we can assume in lowest order $f = f_0$. Substituting φ with the conserved quantities in Eq. 2.19 then gives

$$\frac{\partial \rho}{\partial t} + \nabla \cdot (\rho \mathbf{u}) = 0 \quad (2.23)$$

$$\frac{\partial (\rho \mathbf{u})}{\partial t} + (\rho \mathbf{u} \cdot \nabla) \mathbf{u} + \nabla P + \mathbf{F} = 0 \quad (2.24)$$

$$\frac{\partial \varepsilon}{\partial t} + \mathbf{u} \cdot \nabla \varepsilon + \frac{P}{\rho} \nabla \cdot \mathbf{u} = 0, \quad (2.25)$$

with P as the gas pressure and ε as the specific internal energy. This set of equations is called the Euler equations. In combination with an equation of state, relating ρ , P and ε , which already has been used in deriving Eq. 2.25, these equations form a closed set. Denote that this lowest order approximation takes no viscosity into account, and therefore e.g. no angular momentum can be transported in a disk. This can be avoided by approximating $f = f_0 + \delta f_1$, which will then include a viscous stress tensor and thus lead to the so called Navier-Stokes-Equations. Since in the SPH formalism viscosity is included by an artificial viscosity, the Euler equations are the foundation for this method.

2.1.3 Fully Developed Turbulence

Observations of the ISM show a highly turbulent structure. In general, turbulence consist of non-uniform, irregular motions, often with supersonic velocity and thus leading to shocks.

To treat the turbulent motions in a fluid it is adept to define the dimensionless Reynolds number as

$$\text{Re} = \frac{vl}{\mu}, \quad (2.26)$$

where $v = |\mathbf{v}|$ is the absolute value of the velocity, l is the characteristic length and μ is the kinetic viscosity of a fluid. Turbulence arises as soon as the Reynolds number of a fluid is greater than a critical value Re_{cr} . Experimental tests show that $\text{Re}_{\text{cr}} \approx 10 - 100$. Fully developed turbulence is characterized by irregular variations of the velocity field in time and space. There is no precise analytical treatment, since turbulence in itself is a highly non-linear process. Nevertheless, a qualitative treatment can be deduced (see e.g. Landau & Lifshitz, 1966).

The velocity of a fluid is given by

$$\mathbf{v} = \mathbf{u} + \boldsymbol{\sigma}, \quad (2.27)$$

with \mathbf{u} as mean velocity of the flow and $\boldsymbol{\sigma}$ as the current variations. First, turbulent eddies will arise on length scales comparable to the characteristic size of the flow $l \approx L$ (e.g. the size of the MC). Their velocity fluctuations are comparable to the fluctuations in the mean velocity $\Delta_l \mathbf{u}$. This is called the driving range of the turbulence, which is characterized by

$$l \approx L, \quad \sigma_l \approx \Delta_l \mathbf{u}. \quad (2.28)$$

With time, smaller and smaller eddies arise on scales λ , which can be seen as substructures of the driving eddy. Their fluctuations are smaller than in the driving range, but much bigger than the typical fluctuation of the mean velocity at that length scale

$$\lambda \ll l, \Delta_\lambda \mathbf{u} \ll \sigma_\lambda \ll \Delta_l \mathbf{u}. \quad (2.29)$$

The Reynolds number for any given scale is defined as

$$\text{Re}_\lambda = \frac{\lambda \sigma_\lambda}{\mu}. \quad (2.30)$$

As long as $\text{Re}_\lambda \gg 1$, viscous effects (and thus μ) are of minor importance (see §2.1.1). As soon as λ is comparable to the mean free path ℓ , viscous effects start to dominate and we can define a smallest scale λ_0 , where $\text{Re}_{\lambda_0} \approx 1$. This is the dissipation scale, where the turbulent energy is transformed into heat by viscous effects. Altogether, fully developed turbulence can be described by three regimes:

- the driving regime, where the energy is deposited into the turbulence ($\lambda \approx L$)
- the inertial regime ($\lambda_0 \ll \lambda \ll L$)
- the dissipative regime ($\lambda \approx \lambda_0$).

According to Kolmogorov (1941) in the inertial range the turbulence can be treated as locally homogeneous and isotropic. On this scales energy is neither produced nor lost. Thus, the kinetic energy dissipated² in an eddy n during the time t_n has to be constant and is

$$\varepsilon = \frac{E_n}{t_n} \propto \frac{v_n^2}{t_n} = \frac{v_n^3}{\lambda_n}. \quad (2.31)$$

Solving for the velocity gives the Kolmogorov-Law

$$v_n \approx \varepsilon^{1/3} \lambda_n^{1/3} \quad (2.32)$$

for fully evolved turbulence in ideal, incompressible hydrodynamics. This corresponds directly to the Larson scaling for MCs given in §1.1. In fact this is surprising, since the ISM is normally not considered to be incompressible. However, the true reason for this scaling remains yet to be uncovered. Changing into k-space with $k \propto 1/\lambda$ gives

$$E(k) \propto \frac{v_n^2}{k} \propto \frac{\varepsilon^{2/3} \lambda_n^{-2/3}}{k} = \varepsilon^{2/3} k_n^{-5/3}. \quad (2.33)$$

The one-dimensional $E(k) \propto k^{-5/3} = k^s$ can be transformed into the three-dimensional equivalent $P(\mathbf{k}) \propto k^q$. Under the assumption of isotropy it follows that $q = -2 + s$. Thus, $P(\mathbf{k}) \propto k^{-11/3}$ for the Kolmogorov-scaling of turbulence.

In numerical simulations the dissipation scale λ_0 is usually not given by the mean free path ℓ . This is simply due to the fact, that numerical methods are not able to span all orders of magnitude from the size of MCs down to λ_0 . Therefore, numerical dissipation happens at the resolution limit of the simulations.

²Here dissipation means the transport of kinetic energy from one eddy to another, not the conversion of kinetic energy into heat.

2.2 Radiative Transfer and Ionization

In this section, we derive the equation of radiative transfer from the Boltzmann equation. In addition, the ionization of a static cloud consisting of atomic hydrogen is discussed.

2.2.1 The Radiative Transfer Equation

To derive the equations of radiative transfer we look at a distribution $f(\mathbf{x}, \mathbf{p}, t)$ of photons with energy $h\nu$ and momentum $\mathbf{p} = \frac{h\nu}{c}\mathbf{s}$, where c is the speed of light and \mathbf{s} is the direction of travel. For this distribution the Boltzmann equation (cf Eq. 2.14) must hold:

$$\frac{\partial f}{\partial t} + \frac{\partial f}{\partial \mathbf{x}} \cdot \frac{\mathbf{p}}{m} + \frac{\partial f}{\partial \mathbf{p}} \cdot \mathbf{F} = \left(\frac{\partial f}{\partial t} \right)_{\text{col}}. \quad (2.34)$$

Since the distribution function gives the number of photons with an energy $h\nu$ the radiative energy in a phase-space volume is given by

$$dE_\nu = h\nu f_\nu(\mathbf{x}, \mathbf{p}, t) d\mathbf{x} d\mathbf{p}. \quad (2.35)$$

Photons traveling with the speed c through an area dA during the time dt into a direction \mathbf{s} and a solid angle $d\Omega$ will transverse a volume $d\mathbf{x} = c dt (\mathbf{n} \cdot \mathbf{s}) dA$, where \mathbf{n} is the normal vector of dA . On the other hand, all photons in a small frequency interval $[\nu, \nu + d\nu]$ occupy only a small shell in momentum space: $d\mathbf{p} = p^2 dp d\Omega = \left(\frac{h\nu}{c}\right)^2 \left(\frac{h}{c}\right) d\nu d\Omega$. Thus, Eq. 2.35 can be written as (see e.g. Bodenheimer et al., 2007)

$$dE_\nu = \frac{h^4 \nu^3}{c^2} f_\nu(\mathbf{x}, \mathbf{p}, t) dt \mathbf{n} \cdot \mathbf{s} dA d\nu d\Omega \quad (2.36)$$

and we can define

$$I_\nu(\mathbf{x}, \mathbf{s}, \nu, t) = \frac{h^4 \nu^3}{c^2} f(\mathbf{x}, \mathbf{p}, t) \quad (2.37)$$

as the intensity, the total energy of photons with a frequency $[\nu, \nu + d\nu]$ that travel through an area dA into a solid angle $d\Omega$ per unit time, unit area, unit solid angle and unit frequency interval. Substituting the intensity and neglecting relativistic effects ($\mathbf{F} = 0$) Eq. 2.34 gives

$$\frac{\partial I_\nu}{\partial t} + c(\mathbf{s} \cdot \nabla) I_\nu = \left(\frac{\partial I_\nu}{\partial t} \right)_{\text{col}}. \quad (2.38)$$

As before, all changes of the intensity due to collisions of photons are summed up in $\left(\frac{\partial I_\nu}{\partial t} \right)_{\text{col}}$. The most important collisional processes of a photon with the energy $h\nu$ are listed below (see e.g. Carroll & Ostlie, 2006).

- **Bound-bound transitions** are excitations or de-excitations of the bound electrons of an atom or a molecule. The electron can either return directly to the ground-state emitting a photon of energy $h\nu$ or via several intermediate energy levels emitting several photons or lower energy. The resulting photon(s) are emitted into a random direction.

- **Bound-free absorption** or photoionization is the ionization of an atom by a photon with sufficient energy. We denote the binding energy of the ground state with $h\nu_0$. Thus, a photon with energy $h\nu \geq h\nu_0$ can unbind the electron, thereby ionizing the atom. The surplus energy is transferred into kinetic energy of the photoelectron. For atomic hydrogen $h\nu_0 = 13.6\text{eV}$.
- **Free-free absorption** is the inverse effect of the so called 'bremsstrahlung'. In the vicinity of an ion a free electron can absorb a photon of arbitrary energy. The photon energy is transferred into kinetic energy of the electron, the ion has to be present for energy and momentum conservation.
- **Electron scattering** is the scattering of a photon by a free electron (Thompson scattering) or an electron loosely bound to an atom (Compton scattering and Rayleigh scattering). Since the cross-section for these effects is ten orders of magnitude smaller than the photoionization cross-section of hydrogen, electron scattering does not lead to a considerable absorption of photons.

As the fourth point can be neglected it is sufficient to focus at the first three processes. To treat the absorption we define the mass absorption coefficient κ_ν in a way that dE_ν^{abs} , the energy absorbed per time dt in a frequency interval $[\nu, \nu + d\nu]$ by a volume $dAds$ with the mass density ρ from an one-dimensional ray with intensity I_ν impinging perpendicular to dA into $d\Omega$, is

$$dE_\nu^{\text{abs}} = \kappa_\nu \rho I_\nu d\Omega d\nu dAds dt. \quad (2.39)$$

Analogously the scattering coefficient ζ_ν is defined as

$$dE_\nu^{\text{scatt}} = \zeta_\nu \rho I_\nu d\Omega d\nu dAds dt. \quad (2.40)$$

These two effects reduce the energy (i.e. the amount of photons) in a ray³. Since the ray-energy may also be increased by thermal emission by the volume we define the mass emission coefficient j_ν by

$$dE_\nu^{\text{em}} = j_\nu \rho d\Omega d\nu dAds dt. \quad (2.41)$$

Combining these equations and comparing to Eq. 2.36 the total change of the intensity due to collisions can be deduced similar to Eq. 2.37 as

$$dI_{\nu, \text{coll}} = [\rho j_\nu - (\kappa_\nu + \zeta_\nu) \rho I_\nu] ds. \quad (2.42)$$

Taking the time derivative the total change of the intensity by collisions is thus

$$\left(\frac{\partial I_\nu}{\partial t} \right)_{\text{col}} = c j_\nu - c(\kappa_\nu + \zeta_\nu) \rho I_\nu, \quad (2.43)$$

³Denote that in this form we already neglect the amount of radiation scattered into this ray from other rays. For a more precise treatment see e.g. Shu (1991a)

since $ds/dt = c$ for photons. Substituting this into Eq. 2.38 and looking at a one-dimensional ray in the direction of \mathbf{s} gives

$$\frac{1}{c} \frac{\partial I_\nu}{\partial t} + \nabla I_\nu = \rho j_\nu - (\kappa_\nu + \zeta_\nu) \rho I_\nu, \quad (2.44)$$

the time-dependent equation of radiative transfer. Under the assumptions that κ_ν , ζ_ν , j_ν and the intensity I_ν are constant over time we can derive the time-independent equation of radiative transfer:

$$\nabla I_\nu = \rho j_\nu - (\kappa_\nu + \zeta_\nu) \rho I_\nu. \quad (2.45)$$

2.2.2 Ionization of a Static Cloud

In the following we derive the ionization equilibrium equation for a cloud containing pure hydrogen. In principle a hydrogen atom can be ionized by photons or by collisions with other atoms. We neglect the collisional ionization of hydrogen, since the ionization rate per unit volume $I_{\text{coll}} = 6.23 \times 10^{-16} \text{ cm}^3 \text{ s}^{-1} n_{\text{HI}} n_e$ (see e.g. Altay et al., 2008) gives a minor contribution compared to the UV-flux of a star.

We define the ionization degree $\eta(x) = \frac{n_{\text{HII}}}{n_{\text{H}}} = \frac{n_e}{n_{\text{H}}}$ at a distance x from the star. In the non-equilibrium case the change of the ionization degree is given by the change of the electron density, which depends on the difference of the ionization rate \mathfrak{I} and the recombination rate \mathfrak{R} , i.e. the surplus or missing number of ionizing photons after the recombinations:

$$\frac{d\eta}{dt} = \frac{1}{n_{\text{H}}} \frac{dn_e}{dt} = \frac{1}{n_{\text{H}}} (\mathfrak{I} - \mathfrak{R}). \quad (2.46)$$

The ionization rate is given by Eq. 2.44 and the photoionization cross section of the hydrogen atom, the recombination rate has to be determined by looking at the electron distribution and the cross-section for recombinations of electron with different energy levels of the ionized hydrogen atoms.

The energy-level diagram of HI is depicted in Fig. 2.1, the energy levels are described in the usual quantum mechanic way (n^2L with $n = [0, 1, 2, \dots]$, $L = [S, P, D, F, \dots]$). Allowed transitions are depicted by the solid lines. As the lifetime of excited states are of the order 10^{-8} s to 10^{-4} s (see e.g. Osterbrock, 1989)⁴, which is much shorter than the mean lifetime of an H-atom against photoionization of $\approx 10^8 \text{ s}$ in a typical HII region we can consider all H-atoms to be in the ground state (1^2S). Thus, only photons with an energy $h\nu \geq h\nu_0$ can ionize hydrogen. The ionization cross section for the ground state of hydrogen is

$$\sigma_\nu(\nu) = 6.3 \times 10^{-18} \text{ cm}^2 \left(\frac{\nu_0}{\nu} \right)^4 \frac{e^{4 - (4 \arctan(\varphi)/\varphi)}}{1 - e^{-2\pi/\varphi}} \text{ for } \nu \geq \nu_0, \quad (2.47)$$

where

$$\varphi = \sqrt{\frac{\nu}{\nu_0} - 1}. \quad (2.48)$$

⁴Only the 2^2S level has a mean lifetime of 0.12s, since the transition $2^2S \rightarrow 1^2S$ is less likely.

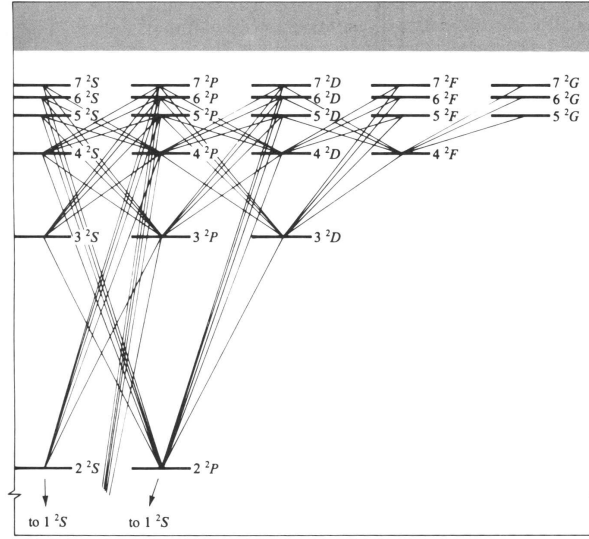


Figure 2.1: Partial energy-level diagram of H I. Permitted radiative transitions are marked with solid lines. (Osterbrock, 1989)

With this cross-section the mean free path of photons can be determined (cf Eq. 2.1)

$$\ell = \frac{1}{n_{\text{H}}\sigma_{\nu}(\nu)} \quad (2.49)$$

which gives close to the Lyman-break $\ell \approx 10^{-3}$ pc for a typical number density $n_{\text{H}} = 50 \text{ cm}^{-3}$ in an HII region.

The surplus energy of the photons is transferred into kinetic energy of the electrons, which will thus obtain a distribution according to the infalling flux. As we have seen in §2.1.1 the electron and the ions (protons) will relax into a Maxwellian distribution on a timescale of 10^{-2} yr. It is therefore valid to approximate the ionized plasma on larger timescales by a mean temperature T . Especially the free electrons can be described by a Maxwellian distribution function dependent on the velocity and mean temperature of the electrons $f(\mathbf{v}, T)$. Thus, the recombination coefficient to a certain level n^2L of the hydrogen atom can be written as

$$\alpha_{n^2L}(H, T) = \int_0^{\infty} \mathbf{v} \sigma_{nL}(H, \mathbf{v}) f(\mathbf{v}, T) d\mathbf{v}, \quad (2.50)$$

where $\sigma_{nL}(H, \mathbf{v})$ is the cross-section for the recombination of an electron with an H-ion. Since every recombination is followed immediately by a cascade down to the ground state, the total recombination coefficient is the sum of the recombination for all levels

$$\alpha_{\text{tot}}(T) = \sum_{n=1}^{\infty} \sum_{L=0}^{n-1} \alpha_{n^2L}(H, T). \quad (2.51)$$

With these results we can attempt to solve the equation of radiative transfer (Eq. 2.44). If we assume the source to be a star during its main-sequence life-time, we can neglect all time

dependencies, as we are looking at a static cloud. The cloud will converge towards an equilibrium solution ($\frac{d\eta_{\text{eq}}}{dt} = 0$) and following Eq. 2.46 the ionization rate has to balance the recombination rate

$$\mathfrak{J} = \mathfrak{R}. \quad (2.52)$$

From now on, we neglect the absorption of photons by scattering. This can be motivated, since only photons with $h\nu \geq h\nu_0$ contribute to the ionization. Therefore, bound-bound transitions can be completely neglected. In addition, the cross-section for free-free absorption drops rapidly for higher ν and thus this process is of minor importance (Shu, 1991a). The emission of photons by recombinations can be included in the emissivity j_ν and thus it is sufficient to look at a simplified version of Eq. 2.45

$$\nabla I_\nu = \rho(j_\nu - \kappa_\nu I_\nu). \quad (2.53)$$

We now separate the intensity for the star and the diffuse component

$$I_\nu = I_\nu^* + I_\nu^{\text{diff}}. \quad (2.54)$$

Since the stellar photons are only emitted inside the star (which is assumed to be negligible small) $j_\nu^* = 0$ and the intensity is given by

$$\nabla I_\nu^* = \rho \kappa_\nu I_\nu^*, \quad (2.55)$$

with the solution

$$I_\nu^*(x) = I_\nu^*(0)e^{-\tau(\nu, x)}. \quad (2.56)$$

Here, we defined

$$\tau(\nu, x) = \int_0^x \rho(x') \kappa_\nu dx' \quad (2.57)$$

as the optical depth along a ray at a distance x from the source. Replacing the intensity by the number of photons with energy $h\nu$ per unit time and unit area $F_\nu^* = \frac{I_\nu^*}{h\nu}$ gives ⁵

$$F_\nu^*(x) = F_{\nu,0}^* e^{-\tau(\nu, x)} \quad (2.58)$$

for the photon flux at a position x , where $F_{\nu,0}^*$ is the total number of photons emitted by the star per unit time and area at a frequency ν .

We now look at the diffuse part of the intensity I_ν^{diff} . At a typical temperature of $T = 10^4$ K the amount of ionizing photons by thermal emission is negligible. All photons with an energy $h\nu \geq h\nu_0$ emitted are therefore due to direct recombinations of electrons to the ground level with a probability $\alpha_1(T)$. Therefore, the number of ionizing photons per volume has to be equal to the number of recombinations to the ground state (cf Eq. 2.46)

$$\int_{\nu_0}^{\infty} \rho j_{\nu,d} d\nu = n_{\text{HII}} n_e \alpha_1(T), \quad (2.59)$$

⁵This is again along a one-dimensional ray. In three dimensions this would have to be the average over all solid angles. In addition, there is a geometrical dilution factor $(4\pi r^2)^{-1}$ in $F_\nu^*(x)$.

where $j_{\nu,d} = \frac{j_{\nu}}{h\nu}$. In an optically thick medium the diffuse photons will be absorbed elsewhere in the medium. Thus, the number of emitted diffuse photons equals the number of ionizations by diffuse photons, i.e. all diffuse photons will be confined to the nebula. If we assume that the same assumption holds locally, we obtain $\nabla I_{\nu,d} = 0$ and with Eq. 2.53 it follows that

$$F_{\nu,d} = \frac{j_{\nu,d}}{\kappa_{\nu}}, \quad (2.60)$$

where $F_{\nu,d} = \frac{I_{\nu,d}}{h\nu}$. This is the so called 'On-The-Spot'-Approximation. It holds exactly, if all emitted diffuse photons are absorbed immediately in the direct surrounding. This is a quite good approximation, since the emitted photons have energies $\nu \approx \nu_0$, therefore large cross-sections σ_{ν} (cf Eq. 2.47) and thus a small mean free path.

With these results we can go back to Eq. 2.46. The number of photoionizations has to be equal to the number of recombinations to all levels

$$\int_{\nu_0}^{\infty} \rho \kappa_{\nu} F_{\nu} d\nu = n_{\text{HII}} n_e \alpha_{\text{tot}}(T), \quad (2.61)$$

where $F_{\nu} = \frac{I_{\nu}}{h\nu}$ again. We split F_{ν} in a part from the star and a diffuse part and use Eq. 2.60

$$\int_{\nu_0}^{\infty} \rho \kappa_{\nu} F_{\nu}^* d\nu + \int_{\nu_0}^{\infty} \rho j_{\nu,d} d\nu = n_{\text{HII}} n_e \alpha_{\text{tot}}(T). \quad (2.62)$$

With Eq. 2.59 it follows that

$$\int_{\nu_0}^{\infty} \rho \kappa_{\nu} F_{\nu}^* d\nu = n_{\text{HII}} n_e [\alpha_{\text{tot}}(T) - \alpha_1(T)] = n_{\text{HII}} n_e \alpha_{\text{B}}(T), \quad (2.63)$$

where

$$\alpha_{\text{B}}(T) = \sum_{n=2}^{\infty} \sum_{L=0}^{n-1} \alpha_{n^2 L}(H, T) \quad (2.64)$$

is the recombination coefficient to all levels but the ground state. Combining Eq. 2.58 with $\kappa_{\nu} = \frac{\sigma_{\nu}}{m_{\text{H}}} = \frac{n_{\text{HII}}}{\rho} \sigma_{\nu}$ and $n_{\text{HII}} = (1 - \eta) n_{\text{H}}$ gives

$$(1 - \eta_{\text{eq}}(x)) \int_{\nu_0}^{\infty} n_{\text{H}} \sigma_{\nu} F_{\nu,0}^* e^{-\tau_{\nu,x}} d\nu = \eta_{\text{eq}}(x)^2 n_{\text{H}}^2 \alpha_{\text{B}}(T), \quad (2.65)$$

for the ionization equilibrium ($\frac{d\eta_{\text{eq}}}{dt} = 0$).

Since the cross-section for the photoionization peaks strongly at $h\nu_0$ and then levels off quickly we assume the flux to be monochromatic. Thus, σ_{ν} , τ_{ν} and F_{ν}^* can be approximated by

$$\bar{\sigma} = \frac{\int_{\nu_0}^{\infty} \sigma_{\nu} F_{\nu,0}^* d\nu}{\int_{\nu_0}^{\infty} F_{\nu,0}^* d\nu}, \quad (2.66)$$

$$\bar{\tau} = \int_0^{x'} \bar{\sigma} (1 - \eta_{\text{eq}}(x')) n_{\text{H}}(x') dx' \quad (2.67)$$

and

$$J_{Ly} = \int_{\nu_0}^{\infty} F_{\nu,0} d\nu, \quad (2.68)$$

the average cross section, average optical depth and the total ionizing flux of the star. For a fixed temperature of the hot gas $\alpha_B = \alpha_B(T)$ it follows that

$$(1 - \eta_{eq}(x)) \bar{\sigma} n_H J_{Ly} e^{-\bar{\tau}} = \eta_{eq}(x)^2 n_H^2 \alpha_B \quad (2.69)$$

is the simplified prescription of the ionization equilibrium for a monochromatic flux. In the case of a homogeneous density distribution this equation can be solved numerically and gives the precise shape of the ionization front. For the case of plane-parallel radiation this is performed in §4.3.1.

If we expand the treatment to the non-equilibrium case it follows from Eq. 2.69 and 2.46 that the change of the ionization degree is given by

$$\frac{d\eta}{dt} = (1 - \eta(x)) \bar{\sigma} J_{Ly} e^{-\bar{\tau}} - \eta(x)^2 n_H \alpha_B. \quad (2.70)$$

This equation is used to calculate the evolution of the ionization degree numerically (see §3.2.2).

Altogether, this equation was derived using the following approximations:

- The cloud consists of pure hydrogen.
- Collisional ionizations are neglected.
- All hydrogen atoms are in the ground state, since the transitions times between different energy levels are very short.
- The flux of the star and the diffuse emissivity are constant over time.
- The scattering of photons is neglected, as the free-free absorption cross-section for ionized photons drops quickly and the electron density is low.
- All ionizing photons emitted after recombinations are absorbed immediately in the direct surrounding ('On-The-Spot'-Approximation).
- The ionizing photons are assumed to be monochromatic as the photoionization cross-section peaks at the Lyman break and then levels off quickly.
- The entire HII region has a constant temperature.

2.3 Evolution of an HII region

Let us now consider the evolution of the ionization front in a dynamic hydrogen cloud, where the density is not constant. In general, the evolution can be divided into two phases:

- A first phase, characterized by the rapid expansion of the ionization front. This phase happens on timescales, which are comparable to the recombination timescale t_{rec} . Therefore, the evolution is so fast that the gas can not react to its increase in pressure and the evolution is similar to the case of a static cloud (see §2.2.2).
- A second phase, which starts as soon as the hot gas reacts to its higher temperature and expands into the cold surrounding cloud. Since the expansion lowers the density of the hot gas, less photons are used up to compensate the recombination and the ionization can penetrate further into the neutral cloud. This phase lasts until the hot and the cold gas are in pressure equilibrium or until the O star finishes its main-sequence lifetime.

2.3.1 The Strömgen-Sphere

In the initial phase of rapid expansion the entire volume, which can be kept from recombining by the star, is ionized. This is the so called Strömgen-Sphere (Strömgen, 1939). Integration of Eq. 2.65 over a volume dV gives

$$J_{\text{Ly}} = V_s n_{\text{H}}^2 \alpha_{\text{B}}, \quad (2.71)$$

since $\int_0^{r_s} (1 - \eta) n_{\text{H}} \bar{\sigma} e^{-\bar{\tau}} dr = e^{-\bar{\tau}(0)} - e^{-\bar{\tau}(r_s)} = 1$. This means that the entire flux of the star has to be used up in a volume V by recombinations. Here, it is assumed that the sphere is fully ionized ($\eta = 1$). Solving for the radius of this sphere gives

$$R_{\text{S}} = \left(\frac{3J_{\text{Ly}}}{4\pi n_{\text{H}}^2 \alpha_{\text{B}}} \right)^{\frac{1}{3}}. \quad (2.72)$$

The position of the front while approaching the equilibrium value $r_{\text{I}}(t)$ is given by

$$4\pi r_{\text{I}}^2 n_{\text{H}} \frac{dr_{\text{I}}}{dt} = J_{\text{Ly}} - \frac{4\pi r_{\text{I}}^3}{3} n_{\text{H}}^2 \alpha_{\text{B}}, \quad (2.73)$$

which can be motivated by e.g. Eq. 2.70. Solving for $r_{\text{I}}(t)$ and then integrating gives

$$r_{\text{I}}(t) = r_{\text{S}} \left(1 - e^{t/t_{\text{rec}}} \right)^{\frac{1}{3}}, \quad (2.74)$$

where $t_{\text{rec}} = \frac{1}{n_{\text{H}} \alpha_{\text{B}}}$ is the recombination timescale. This is discussed in more detail for the plane-parallel case in §4.3.1.

2.3.2 Jump Conditions for Ionization Fronts

We will now derive the jump conditions for ionization fronts under the assumption of a thin shocked layer. This is valid, since the front itself is only a few mean free-paths thick ($\ell \approx 10^{-3}$ pc, see §2.2.2). If we assume the ionization of a homogeneous medium the problem is spherically symmetric and we can therefore use an one-dimensional approach (see e.g. Shu, 1991b). We place ourselves in the frame of the ionization front and denote the quantities in the hot, ionized gas with the subscript 2 and in the cold, neutral gas with the subscript 1. During both evolutionary phases the mass (Eq. 2.23) and the momentum (Eq. 2.24) across the front has to be conserved

$$\rho_1 v_1 = \rho_2 v_2 \quad (2.75)$$

$$P_1 + \rho_1 v_1^2 = P_2 + \rho_2 v_2^2. \quad (2.76)$$

If T_1 and T_2 are assumed to be constant the pressure is

$$P_{1,2} = \rho_{1,2} a_{1,2}^2 = \rho_{1,2} \frac{kT_{1,2}}{\mu_{1,2} m_{\text{P}}}, \quad (2.77)$$

with $a_{1,2}$ as the isothermal sound-speed of the gas. For pure atomic hydrogen the mean molecular weights are $\mu_1 = 1.0$ and $\mu_2 = 0.5$, respectively. Eq. 2.76 can be written as

$$\rho_2 (a_2^2 + v_2^2) = \rho_1 (a_1^2 + v_1^2). \quad (2.78)$$

substituting v_2 from Eq. 2.75 gives the quadratic equation

$$a_2^2 \left(\frac{\rho_2}{\rho_1} \right)^2 - (a_1^2 + v_1^2) \frac{\rho_2}{\rho_1} + v_1^2 = 0 \quad (2.79)$$

with the solutions

$$\frac{\rho_2}{\rho_1} = \frac{1}{2a_2^2} \left[(a_1^2 + v_1^2) \pm \sqrt{f(v_1^2)} \right] = \frac{v_1}{v_2}. \quad (2.80)$$

Physical meaningful solutions arise only if the square-root is not imaginary, hence $f(v_1^2) = (a_1^2 + v_1^2) - 4a_2^2 v_1^2 > 0$. The roots of $f(v_1^2) = 0$ are

$$v_{\text{R}} = a_2 + \sqrt{a_2^2 - a_1^2} \approx 2a_2 \quad (2.81)$$

$$v_{\text{D}} = a_2 - \sqrt{a_2^2 - a_1^2} \approx \frac{a_1^2}{2a_2}. \quad (2.82)$$

The approximations hold as long as $a_2^2 \gg a_1^2$, which is always true in HII regions. Thus, there are two physical meaningful solutions. We call them R-type front for

$$v_1 \geq v_{\text{R}} \quad (2.83)$$

and D-type front for

$$v_1 \leq v_D \quad (2.84)$$

for reasons that will be explained shortly. Denote that

$$v_R v_D = a_1^2 \quad (2.85)$$

and

$$v_R + v_D = 2a_2. \quad (2.86)$$

With these relations Eq. 2.80 can be rewritten as

$$\frac{\rho_2}{\rho_1} = \frac{v_2}{v_1} = \frac{1}{2a_2^2} \left[(v_R v_D + v_1^2) \pm \sqrt{(v_1^2 - v_R^2)(v_1^2 - v_D^2)} \right]. \quad (2.87)$$

We call the front R-critical or D-critical if the square-root vanishes, i.e. if $v_1 = v_R$ or $v_1 = v_D$. For the minus sign, the density contrast for the R-type front in the limit is

$$\frac{\rho_2}{\rho_1} \rightarrow 1 + \frac{a_2^2}{v_1^2} \approx 1 \text{ for } v_1 \gg a_2. \quad (2.88)$$

Thus the front is called 'rarefied', since the density is equal before and behind the front. This is the case we expect at the ignition of the O star. For the D-type front the case with the plus sign gives in the limit $v_1 \rightarrow 0$

$$\frac{\rho_2}{\rho_1} = \frac{a_1^2}{a_2^2}, \quad (2.89)$$

the density in the neutral gas is much higher, we therefore named it 'dense' front before. This density contrast corresponds to static pressure equilibrium $\rho_2 a_2^2 = \rho_1 a_1^2$, the phase we would expect at the very end of the expansion phase.⁶

2.3.3 Expansion of an HII region

As seen in the section before, after the ignition of an O star the front should start as a R-type front and end as a D-type front. Since the square-root in Eq. 2.80 can not become negative, the transition from one front to another is forbidden. The solution is as follows. In the beginning the ionization travels with a speed $v_I > a_2$ until it reaches its Strömngren-radius as discussed in §2.3.1. This radius is reached in a few recombination times (≈ 5 kyr). On timescales that short, the hot gas can not react to its increase in pressure. After a hydrodynamical crossing time, the hot gas starts to expand and a shock front is driven into the cold medium. As we will show, a R-critical front ($v_1 = v_R$) equals a D-critical front ($v_1 = v_D$) plus an isothermal shock and thus the transition is now possible.

⁶Denote that the two front classes can be subdivided into a 'weak' and a 'strong' branch (see e.g. Shu, 1991b). To be precise, the fronts important for the evolution of HII regions discussed here are called 'weak' R-type and 'weak' D-type fronts.

For an isothermal shock, mass (Eq. 2.75) and momentum conservation (Eq. 2.76) must apply. In the isothermal case, the sound-speed $a_0 = a_1 = a$ is the same on both sides of the front and it follows

$$\rho_1(v_1^2 + a^2) = \frac{\rho_0 v_0}{v_1}(v_1^2 + a^2) = \rho_0(v_0^2 + a^2), \quad (2.90)$$

where 0 denotes the undisturbed and 1 denotes the shocked gas. Solving this equation yields

$$v_0 v_1 = a_1^2. \quad (2.91)$$

From the previous chapter we know (Eq. 2.85):

$$v_R v_D = a_1^2. \quad (2.92)$$

Thus a front, streaming with a velocity v_R into the undisturbed, cold gas can be transformed by an isothermal shock into a front with a velocity v_D .

After this transition, the evolution is mainly dominated by hydrodynamics. The ram pressure on both sides of the front has to be equal (see e.g. Dopita & Sutherland, 2003)

$$P_{\text{ion}} = P_{\text{cold}}, \quad (2.93)$$

where

$$P_{\text{cold}} = \rho_0 v_s^2 = \rho_0 \left(\frac{dr}{dt} \right)^2, \quad (2.94)$$

with $v_s = \frac{dr}{dt}$ as the speed of the shock front. The pressure at the ionized side of the shock is given by the thermal pressure of the hot gas

$$P_{\text{ion}} = P_{\text{hot}} = \rho_2 a_2^2. \quad (2.95)$$

If we assume that the ionizations balance the recombinations in the HII region during the entire evolution the Strömgren-Sphere (Eq. 2.71) can be solved for the density

$$\rho_2 = \sqrt{\frac{3m_{\text{P}}^2 J_{\text{Ly}}}{4\pi r^3 \alpha_{\text{B}}}}. \quad (2.96)$$

Thus,

$$r^3 \left(\frac{dr}{dt} \right)^4 = \frac{3m_{\text{P}}^2 J_{\text{Ly}}}{4\pi \rho_0^2 \alpha_{\text{B}}} a_2^4 = R_{\text{S}}^3 a_2^4 \quad (2.97)$$

or

$$r^{\frac{3}{4}} \frac{dr}{dt} = R_{\text{S}}^{\frac{3}{4}} a_2. \quad (2.98)$$

Integration is possible and with the boundary condition $r(t_0) = R_{\text{S}}$ it follows

$$r(t) = R_{\text{S}} \left(1 + \frac{7}{4} \frac{a_2}{R_{\text{S}}} (t - t_0) \right)^{\frac{4}{7}}. \quad (2.99)$$

This is only an approximate solution, according to Shu (1991b) this can also be used as “rough analytic solution” to an accuracy of about 10 percent. For the plane-parallel case this is discussed in §6.2 and a fitting factor is introduced to match the simulations precisely.

2.4 Physical Timescales, Heating and Cooling

To conclude the theoretical foundations we take a quick look at the timescales of the physical processes involved. All quantities are evaluated for typical values of a molecular cloud as used in our simulations. In detail, $n = 300 \text{ cm}^{-3}$, $M = 500 M_{\odot}$, $r = 2 \text{ pc}$, $a_{\text{hot}} = 12.8 \text{ km s}^{-1}$, $a_{\text{cold}} = 0.2 \text{ km s}^{-1}$ and $\alpha_{\text{B}} = 2.59 \times 10^{-13} \text{ cm}^3 \text{ s}^{-1}$.

The gravitational timescale is the free-fall timescale, the characteristic time that it would take a body to collapse under its own gravitational attraction

$$t_{\text{ff}} = \sqrt{\frac{3\pi}{32G\rho}} \approx 3 \text{ Myr}, \quad (2.100)$$

where G is the gravitational constant. The hydrodynamical evolution is given by the sound-crossing time, for the cold gas

$$t_{\text{cold}} = \frac{r}{a_{\text{cold}}} \approx 10 \text{ Myr} \quad (2.101)$$

and for the hot gas

$$t_{\text{hot}} = \frac{r}{a_{\text{hot}}} \approx 150 \text{ kyr}. \quad (2.102)$$

An estimate for the timescales of ionization can be given by the recombination timescale. It takes a Strömgren-Sphere $\approx 5t_{\text{rec}}$ to reach its equilibrium value (cf Eq. 2.74), where

$$t_{\text{rec}} = \frac{1}{n_{\text{H}}\alpha_{\text{B}}} \approx 0.4 \text{ kyr}. \quad (2.103)$$

An estimate for the cooling and heating involved in molecular clouds is much more complex and its numerical implementation would be a thesis on its own (see e.g. Walch, 2008). Therefore, we only briefly review the basic concept. In a molecular cloud, the main source of heating is the electron capture by CII and other ions and the subsequent photoionization. The main source of cooling at temperatures below 100 K is radiation of excited molecules and atoms. These excitations are mainly produced by electrons and H atoms. The main coolant is again CII, since it is the most abundant heavy ion in HI-regions. Balancing the cooling rate $\Lambda_{\text{H,CII}}$ and the heating rate Γ_{ei} gives an estimate for the equilibrium temperature

$$T_{\text{E,cold}} \approx 10 - 20 \text{ K}. \quad (2.104)$$

Following Spitzer (1978), the cooling time can be estimated as

$$t_{\text{C,cold}} \approx \frac{2.4 \times 10^5}{n_{\text{H}} \text{ cm}^3} \text{ yr} \approx 0.8 \text{ kyr}. \quad (2.105)$$

In the hot, ionized gas, the heating is of course provided by the surplus energy of the photo-electrons and is determined by the spectrum of the emitting star. As seen in §2.1.1 the plasma of electrons and protons will relax into a Maxwellian distribution very fast ($t_{\text{rel}} < 10^{-2} \text{ yr}$). The main source of cooling in this regions are transitions of higher ionization levels of O, Ne and

N with excitation energies of $1.9 - 3.3 \text{ eV}$. Excitation of these levels rises sharply with the temperature, as only the electrons in the tail of the Maxwellian distribution achieve these energies and their number rises strongly with T . On the other hand, these levels can radiate away energy effectively via cascading down on several levels. The cooling time can be estimated as (Spitzer, 1978)

$$t_{\text{C,hot}} \approx \frac{2.4 \times 10^4}{n_{\text{H}} \text{ cm}^3} \text{ yr} \approx 0.08 \text{ kyr}, \quad (2.106)$$

which is much smaller than the recombination timescale t_{rec} , the timescale of the heating by photoionization. Thus, these transitions cool the ionized gas to an equilibrium temperature

$$T_{\text{E,hot}} \approx 10^4 \text{ K}, \quad (2.107)$$

below which the cooling gets inefficient, since the energy of the electrons is no longer sufficient to excite the higher levels with energies $> 1 \text{ eV}$ and the lower levels are not able to radiate energy away as efficiently. For a more detailed analysis of the processes involved see e.g. the textbooks by Spitzer (1978) and Osterbrock (1989).

Altogether, the hierarchy of timescales is as follows

$$t_{\text{ff}} \approx t_{\text{cold}} > t_{\text{hot}} > t_{\text{rec}} > t_{\text{C,cold}} > t_{\text{C,hot}}. \quad (2.108)$$

From this, we can draw two important conclusions. First, we can treat the ionization as decoupled from all hydrodynamic and gravitational interactions. As the recombination timescale is much shorter, we can always assume that ionization equilibrium has been achieved. Second, we can treat both, the hot and the cold component, as isothermal ($\gamma = 1$), since heating and cooling always balance into an equilibrium temperature on timescales shorter than all other processes.

Chapter 3

Numerical Implementation

In this chapter the numerical treatment of HII regions applied in this thesis is derived. First, we give a brief overview of SPH, the numerical method used. Then, we go on to prescribe the implementation of ionizing radiation into this method.

3.1 The Method SPH

In contrast to grid based methods smoothed particles hydrodynamics (SPH) does not evaluate the physical quantities on fixed positions, but rather follows the dynamic evolution on moving integration points. These moving integration points can be viewed as particles. The main advantage of SPH is thus the adaptive resolution. In regions of high density, many particles are present and the resolution is high. As a trade-off, low-density regions are less resolved. This poses problems, especially in simulations dominated by instabilities (Agertz et al., 2007). Solving these issues is work in progress. Nevertheless, SPH is ideally suited to study gravity dominated problems which include several orders of magnitude (e.g. the collapse of MCs, star formation,...). Excellent reviews of the SPH technique can be e.g. found in Benz (1990), Monaghan (1992) and Price (2005).

3.1.1 Basic Equations

The fully three-dimensional simulations in this thesis have been performed with the OpenMP-parallel SPH/tree-code VINE (Wetzstein et al., 2008; Nelson et al., 2008). As mentioned before, SPH follows the motion of fluid elements. This requires a Lagrangian prescription (see §2.1.2). The equations describing the motion of a fluid element described by a particle i with a mass m_i are

$$\frac{d\mathbf{x}_i}{dt} = \mathbf{v}_i \quad (3.1)$$

$$\frac{d\mathbf{v}_i}{dt} = -\frac{\nabla P_i}{\rho_i} - \frac{\nabla \Phi_i}{m_i}. \quad (3.2)$$

$$\frac{du_i}{dt} = -\frac{P}{\rho}\nabla u_i \quad (3.3)$$

The first equation is a straightforward definition of the velocity. The second equation can be derived from the momentum equation Eq. 2.24 by using the change from the partial to the total differential $\frac{d}{dt} = \frac{\partial}{\partial t} + \mathbf{v} \cdot \nabla$ and using the mass conservation equation in its Lagrangian form. In addition, we have identified the external force as gravity and replaced it by the gravitational potential Φ . The third equation is the energy equation Eq. 2.25 in Lagrangian form, where the specific internal energy ε is now denoted by u_i . As each particle represents a mass m_i , the mass is conserved automatically as long as no particles are removed from the simulation.

Since each SPH-particle represents a fluid element it is not treated as a point mass, but as a smeared out density distribution. This is achieved via smoothing out the hydrodynamical quantities by a kernel. In VINE, the widely used W4-SPH kernel (Monaghan & Lattanzio, 1985), is employed, which is in three dimension given by

$$W(r_{ij}, h_{ij}) = \frac{\sigma}{h_{ij}^v} \begin{cases} 1 - \frac{3}{2}v^2 + \frac{3}{4}v^3 & \text{if } 0 \leq v < 1, \\ \frac{1}{4}(2-v)^3 & \text{if } 1 \leq v < 2, \\ 0 & \text{otherwise,} \end{cases} \quad (3.4)$$

where $v = \frac{r_{ij}}{h_{ij}}$ is the dimensionless separation of two particles i and j . Here, $r_{ij} = |r_i - r_j|$ is the distance of the particles and $h_{i,j} = (h_i + h_j)/2$ is the characteristic smoothing length scale, with h_i and h_j as the individual smoothing lengths of the particles. From this definition all particles with $v < 2$ contribute as 'neighbours' to the evaluation of the hydrodynamical quantities. These are calculated as a weighted sum over all neighbours. For the density this gives

$$\rho_i = \rho(r_i) = \sum_{j=1}^N m_j W(r_{ij}, h_{ij}). \quad (3.5)$$

Denote that the kernel is symmetric with respect to an interchange of the indices. This is important to ensure the conservation of e.g. momentum. All the hydrodynamical quantities have to be symmetrized as well. The symmetric version of Eq. 3.2 is

$$\frac{d\mathbf{v}_i}{dt} = -\sum_j m_j \left(\frac{p_i}{\rho_i^2} + \frac{p_j}{\rho_j^2} \right) \nabla_i W(r_{ij}, h_{ij}). \quad (3.6)$$

As mentioned in §2.1.2 SPH implements the lowest order approximation of the Boltzmann-Equation, which leads to the Euler equations. This is due to the fact that the next order approximation, the Navier-Stokes-Equation, includes second order spatial derivatives. The calculation of these derivatives can lead to problems due to the disorder of the integration points, i.e. the particles. Instead, viscous effects are treated in SPH by introducing an artificial viscosity. With this viscosity Eq. 3.6 changes to

$$\frac{d\mathbf{v}_i}{dt} = -\sum_j m_j \left(\frac{p_i}{\rho_i^2} + \frac{p_j}{\rho_j^2} + \Pi_{ij} \right) \nabla_i W(r_{ij}, h_{ij}), \quad (3.7)$$

where

$$\Pi_{i,j} = \begin{cases} (-\alpha_{ij}c_{ij}\mu_{ij} + \beta_{ij}\mu_{ij}^2)/\rho_{ij} & \mathbf{v}_{ij} \cdot \mathbf{r}_{ij} \leq 0, \\ 0 & \mathbf{v}_{ij} \cdot \mathbf{r}_{ij} > 0 \end{cases} \quad (3.8)$$

is the standard artificial viscosity (Gingold & Monaghan, 1983). Here, c_{ij} and ρ_{ij} are the symmetrized sound-speed and density. $\mathbf{v}_{ij} = |\mathbf{v}_i - \mathbf{v}_j|$ is the velocity difference and

$$\mu_{ij} = \frac{h_{ij}\mathbf{v}_{ij} \cdot \mathbf{r}_{ij}}{\mathbf{r}_{ij}^2 + \eta^2 h_{ij}^2}, \quad (3.9)$$

is the velocity divergence, with $\eta \approx 10^{-1} - 10^{-2}$ to prevent singularities. The ' α ' term in the artificial viscosity is comparable to a bulk viscosity, whereas the ' β ' term corresponds to a von Neumann-Richtmyer viscosity, which converts kinetic energy to thermal energy and prevents particle intersections. This standard artificial viscosity is used in all simulations in this thesis.¹

The energy equation Eq. 3.3 is implemented in VINE to provide the heating by PdV work. As we showed in §2.4 that HII regions and cold molecular clouds can be treated as isothermal ($du/dt = 0$), this equation is not used in this thesis. Instead, we fix the internal energy for every particle to $u_i = a^2$, where

$$a = \sqrt{\frac{\gamma k_B T}{\mu m_p}} \quad (3.10)$$

is the isothermal sound-speed (see Eq. 2.77).

To complete the set of equations an equation of state is needed, which correlates density, pressure and internal energy. In the isothermal case this is simply given by

$$P_i = \rho_i u_i = \rho_i a^2. \quad (3.11)$$

From this short overview it can already be seen that the choice of the smoothing length, i.e. the volume a particle occupies, is essential in SPH. The accuracy of the integration rises with an increasing number of neighbours, but the computational costs rise as well. A too high number of neighbours reduces the resolution, as only scales larger than h are resolved and smaller scales are smeared out. Furthermore, the number of neighbours per particle should roughly stay constant during the entire calculation to ensure a constant accuracy as well as a constant resolution. Thus, the smoothing length has to be variable in both space and time. The time-dependent smoothing length is given by (Benz et al., 1990)

$$\frac{dh_i}{dt} = -\frac{1}{3} \frac{h_i}{\rho_i} \frac{d\rho_i}{dt} = \frac{1}{3} h_i \nabla \cdot \mathbf{v}_i. \quad (3.12)$$

If this equation leads to a neighbour count outside the allowed range, an exponential correction term is used to push the number of neighbours back into the allowed range. In the standard version of VINE the mean number of neighbours is set to $N = 50$, with an allowed variation of $\Delta N = 20$. This is generally the classic value for the number of neighbours in SPH simulations.

¹VINE also offers a Balsara viscosity, which allows for a better treatment of shear flows, but since the focus of this thesis is not on shear flows it was not used for performance reasons.

However, recent simulations by Attwood et al. (2007) show that a smaller ΔN makes the numerical dissipation a bit smaller. We found the same behavior for the VINE code in the framework of a code comparison (Kitsionas et al., 2008). Nevertheless, we use $\Delta N = 20$ in all simulations presented in this thesis to save computational costs. This is reasonable, since the scales relevant for this work are above the numerical dissipation length.

3.1.2 Time Stepping and Tree Accuracy

The next issue we are going to look at is the correct time integration of the quantities defined in the previous chapter. VINE offers two integrators, a second order Runge-Kutta-Fehlberg integrator and a second order Leapfrog integrator. Since the second one is used throughout this thesis we will focus on it. In a Leapfrog integrator, the update of a physical quantity and its derivative are offset by half a step. Each will be updated in full steps, so that the two updates 'leapfrog' over each other. For the position and velocity the offset form is given as

$$x^{n+1/2} = x^{n-1/2} + v^n \Delta t^n \quad (3.13)$$

$$v^{n+1} = v^n + a^{n+1/2} \Delta t^n, \quad (3.14)$$

where a is the acceleration of a particle. Of course this is done in all three spatial directions. The entire sequence of updates can be written as

1. update all positions to $x^{n+1/2}$, extrapolate all other quantities
2. compute derivatives, e.g. $a^{n+1/2}$
3. update all velocities to v^{n+1}
4. update all positions to x^{n+1} via $x^{n+1} = x^{n+1/2} + \frac{1}{2}(v^n + v^{n+1})\Delta t^n$.

After that, begin from the start. The fourth step is necessary, since for e.g. the calculation of the gravitational force, positions and velocities have to be known at the full update position.

This integration is only stable, if the time-steps used are small enough. As before, this is a trade-off between accuracy and computational time. To allow an efficient treatment, individual particle time-steps are used. Thus, every particle follows its own time-steps, which is especially useful if a calculation covers several orders of magnitude. The time-step can be derived from the change in a particle's

$$\text{acceleration : } \Delta t_{\text{acc}}^{n+1} = \tau_{\text{acc}} \sqrt{\frac{h}{|\mathbf{a}|}}, \quad (3.15)$$

$$\text{velocity : } \Delta t_{\text{vel}}^{n+1} = \tau_{\text{vel}} \frac{h}{|\mathbf{v}|}, \quad (3.16)$$

$$\text{both : } \Delta t_{\text{velacc}}^{n+1} = \tau_{\text{velacc}} \sqrt{\frac{|\mathbf{v}|}{|\mathbf{a}|}}, \quad (3.17)$$

where $\tau \approx 0.5$ is a tuning parameter. In this thesis, the combination of both criteria is used. For SPH, two additional criteria are needed. One is the Courant-Friedrichs-Lewy (CFL) criterion (Monaghan, 1989)

$$\Delta t_{\text{CFL}}^{n+1} = \tau_{\text{CFL}} \frac{h_i}{c_i + 1.2(\alpha_i c_i + \beta_i h_i \max_j(\mu_{ij}))}, \quad (3.18)$$

which ensures that information about the flux is not propagated further than one smoothing length. Good results are usually obtained with $\tau_{\text{CFL}} \approx 0.3$. The other is a criterion for the smoothing length

$$\Delta t_h^{n+1} = \tau_h \frac{h_i}{\dot{h}_i}, \quad (3.19)$$

which ensures that the smoothing length does not change rapidly and thus particles encountering a strong shock do require several time-steps to pass through the shock. The recommended value is $\tau_h \approx 0.15$ (e.g. Wetzstein et al., 2008).

A particle i gets then assigned the minimum value of these as a new time-step:

$$\Delta t_i^{n+1} = \min_k \left(\Delta t_{i,k}^{n+1} \right). \quad (3.20)$$

The calculation of the gravitational force is the most expensive part of any calculation involving gravity. In principle, it is a direct sum of all interactions of the particles on each other. However, in collisionless systems (see §2.1.1) it is sufficiently accurate to calculate this force approximately. The interaction with several more distant particles is assumed to can be treated as one single interaction. Thus, more remote distributions of particles enter as a point source into the calculation. The challenge in this approach is the decision, which particles are remote enough. First, all particles get organized in a tree data structure. In this tree, the tree nodes can than be used as representants of a group of particles. VINE employs the Press or 'nearest neighbour binary tree' (Press, 1986; Benz, 1990). This tree is a very close representation of the grouping of particles in space. By examining the nodes in the tree, either the entire node can be accepted as interacting or the node can be opened and its children (i.e. smaller nodes or already particles) can be examined. A complete traversal of the tree therefore produces a list of interacting nodes, for which the force can be calculated approximately as well as a list of single particles (i.e. neighbours), for which a direct summation is needed. The usage of a tree reduces the computational cost for N particles to the order $\mathcal{O}(N \log N)$ compared to $\mathcal{O}(N^2)$ for the direct summation. However, this is still dependent on the efficiency of the tree traversal. The contribution of the nodes further away is done by a multi-pole expansion. Therefore, the acceptance of a node is based on the convergence radius of the extrapolation. The 'multi-pole acceptance criterion' (MAC) used in this thesis is the one suggested by Springel et al. (2001), as implemented in VINE (Wetzstein et al., 2008). It uses an approximation for the error in the truncation of the multi-pole expansion at hexadecapole (16th) order for the definition of an error criterion. The relative error of the node in the acceleration calculation compared to the total acceleration at the last time-step is

$$r_{ij}^6 > \frac{M_j h_j^4}{\theta |\mathbf{a}_{\text{old}}|}. \quad (3.21)$$

Here, the gravitational constant is set to $G = 1 \text{ cm}^3 \text{ g}^{-1} \text{ s}^{-2}$, M_j is the mass of a node, \mathbf{a}_{old} is the acceleration of a particle the last time it was calculated and θ is a dimensionless accuracy parameter. In addition, the simple 'geometric' MAC has to be satisfied

$$r_{ij}^2 > (h_j^2 + h_i^2)^2. \quad (3.22)$$

In this thesis, the MAC is used with an accuracy parameter of $\theta = 5 \times 10^{-4}$.

For a more detailed prescription of the VINE code see Wetzstein et al. (2008) and Nelson et al. (2008).

3.2 Implementation of Ionizing Radiation

To implement ionizing radiation into the VINE code we choose a plane-parallel approximation. In a sufficiently large distance from the source of UV-radiation, e.g. an O star, the radiation can be assumed to impinge parallel on a surface, thereby neglecting geometrical aspects. This enables us to look at the evolution of a MC at the border of an HII region in unprecedented detail. Keeping the hierarchy of the time-steps in mind (§2.4) we can always assume the ionization to reach its equilibrium state. As the recombination timescale is much shorter than hydrodynamic and gravitational timescales, we will calculate the ionization degree for all particles on the smallest timescale current in the simulation². The calculation of the new ionization degree is performed right before the equation of state, since then all important quantities such as position and density of the particles are already updated and the updated ionization degree can then be used in the equation of state.

3.2.1 Casting of Rays

In order to determine the rays along which we will propagate the radiation, the transparent surface of our simulated volume facing the O star is decomposed in several sub-domains or rays. We choose the radiation to impinge from the negative x-direction, i.e. the left hand side in most figures. An adept criterion for the size of the rays is the diameter a particle occupies

$$d_{\text{part}} = 2 \cdot \left(\frac{3}{4\pi} \frac{m_{\text{part}}}{\rho_{\text{part}}} \right)^{1/3}. \quad (3.23)$$

The width Δy and the height Δz of the rays is then set to the average value $\overline{d_{\text{part}}}$ of the particles close to the source. Each particle gets assigned to a ray as depicted in Fig. 3.1. The particle number is stored together with its ray-number in a two-dimensional integer array of the length N_{part} . Now, they are sorted into ascending bin number. This is done by the parallel quick-sort routine already implemented in VINE (Nelson et al., 2008), which has been modified to sort

²When gravitational collapse occurs this produces some overhead, as the time-steps can get very short. This does not affect the physical treatment, as the collapsing cores are always self-shielded from the ionization. Nevertheless, it is producing unnecessary calculations and could be optimized.

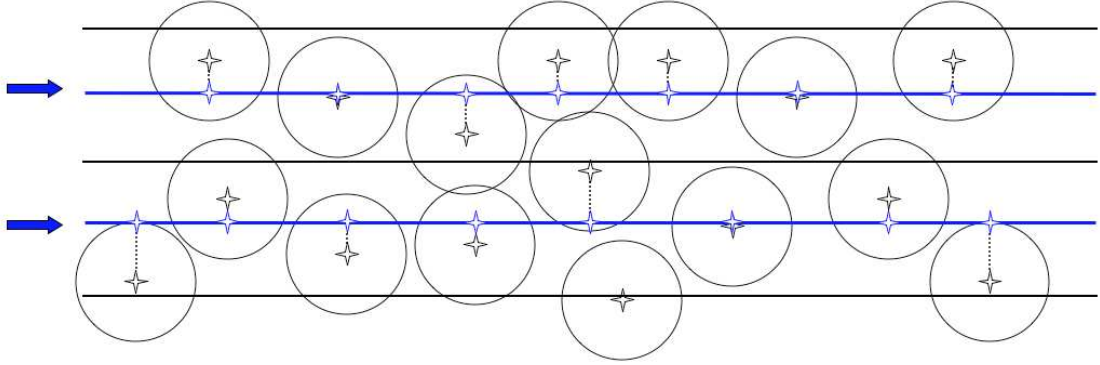


Figure 3.1: Schematic depiction of the sorting of the particles into the rays in two dimensions.

integer values. After that, each CPU gets a chunk of the main array, corresponding to one ray. This poses the last existing bottle-neck in the parallelization of the code. As it is necessary to know the length of the chunks to hand each CPU the correct part of the main array, we have to count the number of particles in every ray. This means a summation into an array of the size number of rays times number of rays, which does not lend itself to an efficient parallelization in OpenMP. As soon as the chunks are handed to the CPUs, the particles inside are sorted in ascending order by their distance to the surface and the radiation is propagated along the rays as described in §3.2.2. This is of course easily parallelized, as long as the number of rays is bigger than the number of CPUs used, which is always the case in our simulations.

After an initial fast evolution the density close to the surface of infall only changes slowly. Thus, Δy and Δz are approaching a fixed value and the number of bins gets constant. To avoid any bias by superimposing a fixed geometry on the simulated volume the particles are shifted by a random factor $\varepsilon_y = [-\frac{1}{2}\Delta y, \frac{1}{2}\Delta y]$ and $\varepsilon_z = [-\frac{1}{2}\Delta z, \frac{1}{2}\Delta z]$ before the sorting into the ray.

During the further evolution, the particles closest to the source reach the much lower density of the hot gas. Therefore, the bin-size gets much smaller than the local d_{part} . To compensate this effect we refine each bin into four sub-bins, as soon as

$$\frac{d_{\text{part}}}{\Delta y} = \frac{d_{\text{part}}}{\Delta z} < \frac{1}{2}. \quad (3.24)$$

Currently, up to eight levels of refinement are implemented. Thus, the effective resolution in each bin can be refined by a factor of up to 256, which leads to a resolution of the ionizing radiation which is higher than the resolution of the SPH-simulation during gravitational collapse (see e.g. §4.4.2, Fig. 4.8).

3.2.2 Calculation of the Ionization Degree

Along the rays, which were defined in the previous chapter, the ionization is calculated corresponding to Kessel-Deynet (1999). As seen in Eq. 2.58 the number of photons at a given position

x per unit time and area is given by

$$F(x) = F_0 e^{-\bar{\tau}(x)}, \quad (3.25)$$

where F_0 is the photon flux at the surface. From now on, the particles are assumed to be lined up in the bin and only the projected distance is evaluated, i.e. the distance of the particles is only calculated in the x -direction. Every particle i occupies a length which is defined by its next neighbours in the ray

$$\Delta x_i = \frac{x_{i+1} - x_{i-1}}{2}. \quad (3.26)$$

According to Eq. 2.57

$$\Delta \tau_i = (1 - \eta_i) n_{\text{H},i} \bar{\sigma} \Delta x_i \quad (3.27)$$

is the optical depth of a particle occupying a length Δx_i along the ray, with $n_{\text{H},i} = \frac{\rho_i}{m_{\text{H}}}$ for pure hydrogen, where ρ_i is given by the SPH-density of the particle. The number of photons per unit time and area entering at the front of the volume the particle is occupying is then given by

$$F_{i,\text{front}} = F_0 e^{\tau_{i-1}}, \quad (3.28)$$

where

$$\tau_{i-1} = \sum_{k=0}^{i-1} \Delta \tau_k \quad (3.29)$$

is the sum of the optical depth along the ray up to the particle i . With the number of photons impinging on the particle the change of the ionization degree can now be calculated via Eq. 2.46

$$\frac{d\eta}{dt} = \frac{1}{n_{\text{H}}} (\mathcal{J} - \mathcal{R}) = \frac{1}{n_{\text{H}}} \nabla F - n_{\text{H}} \eta^2 \alpha_B \quad (3.30)$$

in its discrete form

$$\frac{\Delta \eta_i}{\Delta t} = \frac{F_{i,\text{front}} - F_{i,\text{back}}}{n_{\text{H},i} \Delta x_i} - n_{\text{H},i}^2 \eta_i^2 \alpha_B, \quad (3.31)$$

where

$$F_{i,\text{back}} = F_0 e^{-(\tau_{i-1} + \Delta \tau_i)} \quad (3.32)$$

is the number of photons leaving the particle after the ionization. Thus,

$$\frac{\Delta \eta_i}{\Delta t} = \frac{F_0}{\Delta x_i n_{i,\text{H}}} e^{-\tau_{i-1}} (1 - e^{-\Delta \tau_i}) - n_{\text{H},i} \eta_i^2 \alpha_B \quad (3.33)$$

is the discrete equation giving the change of the ionization degree.

Denote that

$$S_i = \frac{1}{\Delta x_i n_{i,\text{H}}} \quad (3.34)$$

is basically the surface the ionization is impinging on. This should be comparable to d_{part}^2 , the surface of the bin (Eq. 3.23). Defining

$$\beta = \frac{d_{\text{part}}}{\Delta x_i} \quad (3.35)$$

and combining both equations gives

$$\beta = n_i d_i^3 = \frac{6}{\pi} \approx 1.9, \quad (3.36)$$

i.e. the choice of the bins is best when 2 particles occupy a binlength in the x-direction. Estimating the number of particles in the x-direction can be approximated by estimating the kernel with a step-function. Roughly, the volume implied by Eq. 3.23 is half the smoothing length. The number of particles in the smoothing length is 50, therefore in half the length $50/2^3 = 6.25$ particles should be projected in the x-direction per binlength at the start of each bin. Shortly before the refinement, the smoothing length is halved, and thus $50/4^3 = 0.78$ particles should be projected. Thus, on average the number of particles is in the right range. There are of course deviations, especially at the front of the bin. The choice of the bin-size mainly effects the newly ionized part, i.e. the shape of the ionization front, since in the already ionized region only recombinations are important (since $\Delta\tau \approx 0$), which are calculated directly via the SPH-density. Thus, our choice gives a bin-size which becomes best towards the far end of the ray. As the analytical tests in §4.3 show, the choice of the bin-size leads to a very good agreement of the numerical and analytical values.

In order to calculate the time evolution of Eq. 3.33 we take the implicit form

$$\eta_i^n = \eta_i^{n-1} + \Delta t^n (\mathcal{J}_i^n - n_{\text{H},i}^n (\eta_i^n)^2 \alpha_B). \quad (3.37)$$

Here, the index n denotes the current time-step and $n-1$ the last time-step. Besides, I_i^n all quantities are known at the current time-step. According to Eq. 3.33 we can estimate

$$\mathcal{J}_i^n = \mathcal{J}_i^{n-1} \frac{1 - e^{-n_i^n \bar{\sigma} \Delta x_i^n (1 - \eta_i^n)}}{1 - e^{-n_i^n \bar{\sigma} \Delta x_i^n (1 - \eta_i^{n-1})}} \quad (3.38)$$

under the assumption that neither the position nor the density of the particles changed much since the last time-step (i.e. $\Delta x_i^{n-1} \approx \Delta x_i^n$ and $n_i^{n-1} \approx n_i^n$). This is a valid assumption as the ionization is happening on much shorter timescales than any hydrodynamical process (see §2.4). The ionization degree can now be easily obtained by finding a root for

$$f(\eta) = \eta - \eta_i^{n-1} + \Delta t^n (n_{\text{H},i}^n (\eta_i^n)^2 \alpha_B - I_i^n(\eta, \eta_i^{n-1})) = 0, \quad (3.39)$$

where $\eta \equiv \eta_i^n$. This is done with a Newton-Raphson method according to Press (1986). In every iteration, η is modified according to

$$\eta_{k+1} = \eta_k - \frac{f(\eta_k)}{f'(\eta_k)}, \quad (3.40)$$

where k now denotes the iteration. Since the changes in the ionization degree are usually small, this method converges after 3-4 iterations in most cases. The maximum allowed number of 200 iterations in our code is never used. As soon as the ionization degree reaches a value lower than $\eta_i = 10^{-10}$ the calculation is stopped and the ray is left, since the ionizing photons are all used up.

3.2.3 Equation of State and Modification of the Time-step Criterion

With the new ionization degree, the pressure of the particle is derived according to the new temperature. Implementing the ionization degree with a linear extrapolation into Eq. 3.11 gives

$$P_i = \left(\frac{T_{\text{ion}}\eta_i}{\mu_{\text{ion}}} + \frac{T_{\text{non}}(1 - \eta_i)}{\mu_{\text{non}}} \right) \frac{k_B \rho_i}{m_P}. \quad (3.41)$$

This linear approximation proves to be sufficient, as the transition region of the ionization degree is so sharp (see e.g. Fig 4.2), that test simulations with a higher order approximation showed no effect.

Due to this increased pressure, a particle which gets suddenly ionized can receive a huge acceleration. This can lead to problems, especially with the extrapolations involved in the Leapfrog-integrator. To avoid this issue, the newly ionized particles get assigned a new time-step according to

$$\Delta t_{\text{new},i} = \frac{a_{\text{cold}}}{a_{\text{hot}}} \Delta t_{\text{CFL},i}, \quad (3.42)$$

as soon as the ionization degree $\eta > 10^{-3}$. This means that a particle, although its temperature is only $\approx 20\text{K}$ gets the time-step of a particle already at $\approx 10^4\text{K}$ to avoid any unphysical behavior. After that, its time-step is evaluated according to the standard criteria (see §3.1.2). Since the particles gain a bigger time-step very slowly this poses no problem, as the particle will by then achieve its correct time-step, e.g. by the combined velocity and acceleration criterion. The numerical cost of the calculation of the ionization degree is not affected at all by this treatment, since there will be ionized particles with high energies keeping the smallest time-step at all small value anyways throughout the entire simulation. The cost of the hydrodynamic calculation is slightly increased, because the particles attain the small time-step a bit earlier than they would have to by the standard criteria. Nevertheless, this is vital to ensure a correct integration and provides only a tiny increase in the overall calculation time, which is dominated by gravitational acceleration and hydrodynamics (see §4.3.3).

Chapter 4

iVINE - Ionization in the parallel tree/SPH code VINE: First results on the observed age-spread around O-stars

¹M. Gritschneider, T. Naab, A. Burkert, S. Walch, F. Heitsch, M. Wetzstein

We present a three-dimensional, fully parallelized, efficient implementation of ionizing UV radiation for smoothed particle hydrodynamics (SPH) including self-gravity. Our method is based on the SPH/tree code VINE. We therefore call it iVINE (for Ionization + VINE). This approach allows detailed high-resolution studies of the effects of ionizing radiation from e.g. young massive stars on their turbulent parental molecular clouds. In this paper we describe the concept and the numerical implementation of the radiative transfer for a plane-parallel geometry and we discuss several test cases demonstrating the efficiency and accuracy of the new method. As a first application, we study the radiatively driven implosion of marginally stable molecular clouds at various distances of a strong UV source and show that they are driven into gravitational collapse. The resulting cores are very compact and dense exactly as it is observed in clustered environments. Our simulations indicate that the time of triggered collapse depends on the distance of the core from the UV source. Clouds closer to the source collapse several 10^5 years earlier than more distant clouds. This effect can explain the observed age spread in OB associations where stars closer to the source are found to be younger. We discuss possible uncertainties in the observational derivation of shock front velocities due to early stripping of proto-stellar envelopes by ionizing radiation.

ISM: H II regions – ISM: kinematics and dynamics – radiative transfer – ultraviolet: ISM – stars: formation – methods: numerical

4.1 Introduction

As hydrodynamical simulations become more and more advanced one of the key issues is the successful implementation of additional physics like the effects of radiation. Prominent applications are for example the reionization of the early Universe (for a comparison of methods see

¹published as 2009, MNRAS, 393, 21

Iliev et al. 2006 and references therein).

In our present day universe ionizing radiation still plays a vital role. UV-radiation from massive, young stars ionizes their surrounding. The hot, ionized gas then expands into the cold, neutral gas and thus drives shock fronts into the parental molecular clouds. Up to now it is not fully understood if this violent feedback enhances or hinders star formation. Elmegreen & Lada (1977) proposed that the shock front builds up dense regions by sweeping up the cold gas, which then eventually collapse due to gravitational instability and form stars. This is called the 'collect and collapse model' (see also the review by Elmegreen 1998). Another situation arises when preexisting, dense structures (e.g. molecular cloud cores) that are gravitationally marginally stable get compressed by the approaching front and start collapsing. This is commonly called radiation driven implosion (see e.g. Sandford et al., 1982).

Observations provide widespread evidence for these scenarios (see Sugitani et al., 1989; Hester et al., 1996). More recent observations indicate triggered star formation on the edges of HII regions e.g. in the Orion clouds (Stanke et al., 2002), the Carina nebula (Smith et al., 2000), M16 (Fukuda et al., 2002), M17 (Jiang et al., 2002), 30 Dor (Walborn et al., 2002) and the SMC (Gouliermis et al., 2007a). Deharveng et al. (2005) report triggered star formation in samples of more distant HII regions. Besides these quite complex large scale regions there have been numerous observations of bright rimmed cometary globules. These are small isolated clouds with a clear head to tail structure with the dense heads pointing towards an ionizing source (Sugitani et al., 1991). Their morphology enables a direct comparison to simulations. In particular, the properties of individual young stellar objects (YSOs) surrounding OB-associations can be determined precisely. YSOs are observed in the mass range from T Tauri ($0.1 - 3 M_{\odot}$) up to Herbig Ae Be ($2 - 8 M_{\odot}$) stars (see e.g. Lee & Chen 2007, Snider et al. 2007). The velocity of the shock front triggering the star formation is calculated from the age difference of the stars and their relative distance. These estimates are in the range of a few km/s (e.g. Thompson et al. 2004, Getman et al. 2007).

Numerous simulations on the topic of cloud evaporation and sequential star formation have been performed. (Yorke et al., 1982, and references therein) published a series of two-dimensional simulations on the gas dynamics of HII regions, especially on champagne flows, where a stream of hot gas breaks through the border of cold, confining gas. Subsequently, Elmegreen et al. (1995) presented two-dimensional, grid-based simulations showing that the expansion of an HII region into the surrounding cloud can trigger star formation. Kessel-Deynet & Burkert (2003) demonstrated with a three-dimensional SPH code, that a marginally stable molecular cloud core can be triggered into collapse when exposed to strong UV radiation. With a more detailed description of radiation implemented into an SPH code Miao et al. (2006) could reproduce the observed features of the Eagle Nebula, including the photodissociation regions and the temperature profile. Using a three-dimensional grid-based scheme, Mellema et al. (2006) simulated the HII region excavated by a point source of UV-radiation. They find remarkably similar morphologies and physical properties when comparing their models to observations. Furthermore simulations with an SPH-code by Dale et al. (2005) and a grid code by Mac Low et al. (2007) showed that a turbulent interstellar medium surrounding an O-star allows the ionizing radiation to efficiently expel most of the nearby gas. Only the denser regions resist and continue to collapse.

However none of the authors so far described ionizing radiation as an efficient trigger for star

formation. There is only weak evidence by Dale et al. (2007b), that the external irradiation of a collapsing cloud by a point source can indeed increase the star formation efficiency from 3% to 4% when compared to a control run without radiation. For a review of feedback processes we refer the reader to Mac Low (2007). For completeness we would like to refer to recently published implementations for ionizing radiation into an SPH code by Pawlik & Schaye (2008), where the photons of a source are followed along cones, and Altay et al. (2008), where the radiation is followed via a Monte Carlo ray-tracing scheme

All these studies demonstrate that there is a strong connection between the UV-radiative feedback from massive stars and the observed morphologies of the ambient molecular cloud gas. Yet, a quantitative discussion of the interaction between UV-radiation and turbulent molecular clouds is still missing. To advance our understanding, we introduce iVINE, the fully parallel implementation of UV-radiation in the parallel tree-SPH-code VINE (Wetzstein et al. 2008, Nelson et al. 2008). This efficient tool permits high resolution simulations of molecular clouds in the vicinity of strong UV sources such as an O-star or association.

The paper is structured as follows. The physical model and its implementation are described in Section 4.2, followed by a detailed comparison of the scheme with analytical results (Sec. 4.3). We apply the new method to the radiatively driven implosion of a marginally stable molecular cloud core and compare three simulations with different initial UV fluxes to observations (Sec 4.4). In Section 4.5 we summarize and discuss the results.

4.2 Numerical Method

As soon as a young massive star emits UV-radiation it ionizes its surrounding, creating an HII region. Initially the ionization proceeds fast with a speed of this rarefied (or R-type) front of $v_R \gg a_{\text{hot}}$, where a_{hot} is the sound speed of the hot, ionized gas. After a sound crossing timescale the hot gas reacts to its increased temperature and an isothermal shock front is driven into the cold surrounding medium. This dense (or D-type) shock travels at a much smaller speed $v_D \approx a_{\text{hot}}$. For a full textbook analysis of this evolution see e.g. Osterbrock (1989).

4.2.1 Prescription of Ionizing Radiation

To follow the evolution of the HII region of a young massive star in a numerical simulation we use a prescription for the ionizing UV-radiation similar to the one that has been proposed by Kessel-Deynet & Burkert (2000) as presented before (Gritschneider et al., 2007). The flux J at any given position x is given by

$$J(x) = J_{\text{Ly}} e^{-\tau_v(x)}, \quad (4.1)$$

where J_{Ly} is the Lyman continuum flux of the hot star. The optical depth τ_v is given by the integral along the line of sight between the source of radiation and the position x

$$\tau_v = \int_0^x \kappa_v \rho dx, \quad (4.2)$$

where κ_{ν} is the frequency weighted absorption coefficient

$$\kappa_{\nu} = \frac{\sigma_{\nu} n_{\text{H}}}{\rho}, \quad (4.3)$$

with n_{H} being the number density of neutral hydrogen and ρ the mass density of the gas. We assume the gas is pure hydrogen with a mean molecular weight of $\mu = 1$. As the frequency dependent absorption cross section σ_{ν} peaks at the Lyman break it is a valid assumption to take an average cross section $\bar{\sigma}$, thereby approximating the radiation to be monochromatic. Thus, every photon above the Lyman break is assumed to ionize one hydrogen atom.

We define the ionization degree η as

$$\eta = \frac{n_{\text{e}}}{n}, \quad (4.4)$$

where n_{e} is the number density of electrons and n is the combined number density of protons and neutral hydrogen atoms. The time derivative of the ionization degree can be written as

$$\frac{d\eta}{dt} = \frac{1}{n} \frac{dn_{\text{e}}}{dt} = \frac{1}{n} (\mathcal{J} - \mathcal{R}), \quad (4.5)$$

with the ionization rate I given as

$$\mathcal{J} = \nabla J \quad (4.6)$$

and the recombination rate R as

$$\mathcal{R} = n_{\text{e}}^2 \alpha_{\text{B}} = \eta^2 n^2 \alpha_{\text{B}}. \quad (4.7)$$

For the recombination coefficient α_{B} we choose

$$\alpha_{\text{B}} = \sum_{i=2}^{\infty} \alpha_i, \quad (4.8)$$

where α_i is the recombination probability for a level i of the hydrogen atom. The recombination of electrons and protons leads to a diffuse field of Lyman continuum photons, which in turn can again ionize a hydrogen atom. We neglect this effect under the assumption that every reemitted photon is in turn immediately absorbed in the direct surrounding. This assumption, called ‘on the spot approximation’ is valid as long as the hydrogen density is high enough (e.g. Spitzer 1978), which is always true in the vicinity of the ionization front. Some fraction of the UV-photons is absorbed by dust, and re-emitted in the IR-regime, leading to an effective lower flux. We neglect this effect, since the flux incident on the simulation volume is determined largely by its distance from the radiation source, so that geometrical dilution of the radiation field is likely to be more important than absorption by dust.

The average temperature of the gas is coupled linearly to the ionization degree η through

$$T = T_{\text{hot}} \cdot \eta + T_{\text{cold}} \cdot (1 - \eta), \quad (4.9)$$

where T_{cold} is the initial temperature of the cold, unionized gas and T_{hot} is the average temperature of the ionized gas.

4.2.2 Implementation

To treat the hydrodynamical and gravitational evolution of the gas we use the parallel smoothed particle hydrodynamics (SPH) code called VINE which has been developed by Wetzstein et al. (2008) and Nelson et al. (2008). SPH is a Lagrangian method, which renders it extremely suitable to cover several orders of magnitude in density and spatial scale, for example during cloud core collapse and star formation. VINE is a powerful parallel implementation of the SPH method in combination with a tree code for the calculation of gravitational forces. It offers a Runge-Kutta integrator as well as a Leapfrog integrator. Both schemes can be used in combination with individual particle time-steps. For this work the Leapfrog integrator is chosen. Every time the equation of state is computed we calculate the ionization degree for all particles in the entire simulation.

The heating by UV-radiation can be treated as decoupled from the dynamic evolution since the recombination timescale

$$t_{\text{rec}} = \frac{1}{n\alpha_{\text{B}}} \quad (4.10)$$

is much shorter than any hydrodynamical timescale. In our simulations (see Section 4.4) the crossing time even in the hot gas is $t_{\text{hot}} \approx 70 \text{ kyr}$, whereas the recombination timescale is $t_{\text{rec}} \approx 1 \text{ kyr}$ for a number density of $n = 100 \text{ cm}^{-3}$. Thus, it is valid to treat ionization and hydrodynamics as two separate processes. In other words the ionization can be assumed to happen instantaneously. Frequently updating the ionization degree together with a modified time-step criterion (see Section 4.2.3) ensures that the radiation is treated correctly on all scales.

To include the effect of UV-radiation we assume a plane-parallel geometry, i.e. parallel rays. This is valid as long as the distance from the source of radiation is larger than the dimensions of the area of infall. In our simulations the radiation is impinging from the left hand side, that is from the negative x -direction. To couple ionization to hydrodynamics we use a ray-shooting algorithm. As the ionizing flux is propagated along the x -direction, we ensure the conservation of flux by dividing the (y, z) -plane into sub-domains of equal size, whose extent along the x -direction spans the whole simulation domain. Along each of these sub-domains or rays the flux is transported in a conservative manner. To convert the SPH-particle density ρ_{part} correctly into a gas density distribution within these three-dimensional rays the volume and thus the diameter d_{part} that each SPH-particle occupies is calculated via the mass of each particle m_{part} :

$$d_{\text{part}} = 2 \cdot \left(\frac{3}{4\pi} \frac{m_{\text{part}}}{\rho_{\text{part}}} \right)^{1/3}. \quad (4.11)$$

The width Δy and the height Δz of the rays or bins is then set to the average value $\overline{d_{\text{part}}}$ of the particles closest to the source. To determine this value the first two particles in each ray at the previous time-step are taken into account. Since this is the region with the lowest density throughout the entire simulation this guarantees that the bin-size is always larger than the characteristic particle resolution. As soon as the ray approaches a density increase the local d_{part} becomes smaller than Δy and Δz . For

$$\frac{d_{\text{part}}}{\Delta y} = \frac{d_{\text{part}}}{\Delta z} < \frac{1}{2} \quad (4.12)$$

we refine the ray subsequently into four sub-rays to treat the ionization of high density regions correctly. Each of the sub-rays inherits the optical depth of the main ray. Currently the code allows for five levels of refinement, thus increasing the effective bin resolution in each direction by a factor of 32. In principle it would be possible to de-refine the sub-rays by using the average optical depth of the four refined sub-rays for the de-refined bin. We do not include this, since it would lead to an unphysical shading of lower density sub-rays as soon as they are combined with a high density sub-ray due to an overestimation of the optical depth.

To calculate the optical depth, we sort the particles within each bin according to their distance to the source and discretize into subsections of the size

$$\Delta x_i = \frac{x_{i+1} - x_{i-1}}{2}. \quad (4.13)$$

Thus, Δx_i is the projected distance of a particle i to its direct neighbours closer and further away from the source, i.e. the length along the line of sight the particle occupies. We then calculate the optical depth τ along each ray by summing up the individual optical depths τ_i of each particle i . The discrete value of τ_i is given according to Eq. 4.2 as

$$\tau_i = \bar{\sigma} n_{\text{H},i} \Delta x_i. \quad (4.14)$$

The number density n_{H} and the density ρ used to calculate the recombination rate (cf Eq. 4.7) are simply given by the SPH-density ρ_{part} . From these quantities the new ionization degree η is determined according to Eq. 4.2 by a Newton-Raphson iteration scheme. It converges with a precision of more than 0.1% in less than 200 iterations. When the ionization degree reaches a value of $\eta = 1 \times 10^{-10}$ we terminate the further calculation of this bin. This implementation is fully parallelized in OpenMP.

4.2.3 Modification of the Time-step Criterion

A detailed discussion of the different time-step criteria implemented in the underlying VINE code is given in Wetzstein et al. (2008). Note that our implementation of ionizing radiation is designed to be used in connection with individual particle time-steps (see Wetzstein et al., 2008, for details). To exactly follow the evolution of a particle during its ionization process it is vital to use a small enough time-step. To do so we decided to force every particle to a smaller time-step as soon as its ionization degree reaches $\eta > 10^{-3}$, i.e. when the particle is going to be ionized. The new time-step is chosen by a modified Courant-Friedrichs-Lewy (CFL) condition according to

$$\Delta t_{\text{new}} = a_{\text{cold}}/a_{\text{hot}} * \Delta t_{\text{CFL}}, \quad (4.15)$$

where a_{cold} and a_{hot} are the fixed respective sound-speeds of the cold and the ionized gas at T_{cold} and T_{hot} . Δt_{CFL} is the individual time-step the particle would get assigned due to the CFL-condition (see Wetzstein et al., 2008). This ensures that the hydrodynamical quantities are treated correctly even though the particle gets a boost in temperature. Therefore, we anticipate the subsequent acceleration due to the approaching ionization front by choosing already the much smaller time-step even though the particle is just ionized to 0.1%. This criterion also ensures

that the ionization degree is followed accurately during the evolution of the later dense or D-type ionization front, because v_D is always smaller than the sound speed of the hot gas $v_D < a_{\text{hot}}$. Hence, this front will always be resolved by particles which have a small enough time-step to track the hot gas. In the beginning the evolution of the faster R-type front ($v_R \gg a_{\text{hot}}$) can be followed by using a small enough initial time-step since this phase is quite short (≈ 5 kyr).

The choice of a small initial time-step together with the modified CFL-criterion ensure that the ionization degree η of a particle never changes by more than ± 0.1 per time-step in all of our simulations. Thus, the ionization front can be followed in both stages (R- and D-type) precisely.

4.3 Numerical Tests

In order to validate the algorithm we perform several tests. The first series of simulations addresses the evolution of the Strömgen solution and tests whether the time-dependent UV-flux is treated correctly on all scales. In addition, we demonstrate the correct implementation of the refinement (Section 4.3.1). The second series of simulations (Section 4.3.2) is designed to demonstrate the correct interaction of ionizing radiation and hydrodynamics. In the end the successful parallelization of the code is shown (Section 4.3.3).

4.3.1 Ionization without Hydrodynamics

The Strömgen test - Ionization by a constant UV flux

When hydrodynamics is not taken into account, the homogeneous surrounding of an ionizing source will always converge towards an equilibrium between ionization and recombination. The volume of the ionized Strömgen sphere (Strömgen, 1939) around an O-star is given by

$$V_S = \frac{J_{\text{Ly}}}{\alpha_B n^2}, \quad (4.16)$$

assuming a monochromatic source with a constant UV-flux J_{Ly} given in photons per second. α_B and n are again the recombination coefficient and the number density (for a textbook analysis see e.g. Shu 1991b).

In the case of plane-parallel radiation, as discussed here, this volume is characterized by the length x_s , which can be penetrated by the ionizing radiation. x_s is determined by the surface S on which the photon flux per area and time, F_{Ly} , is impinging:

$$x_s = \frac{V_s}{S} = \frac{F_{\text{Ly}}}{\alpha_B n^2}. \quad (4.17)$$

The time evolution of the length $x_I(t)$ of this region is given by the differential equation

$$\frac{dx_I}{dt} n = F_{\text{Ly}} - x_I(t) \alpha_B n^2 \quad (4.18)$$

with the solution

$$x_I(t) = x_s (1 - e^{-t/t_{\text{rec}}}), \quad (4.19)$$

where $t_{\text{rec}} = 1/(n\alpha_B)$ is the recombination or Strömberg timescale. The shape of the front is given by the ionization equilibrium equation

$$n(1 - \eta) \int_{v_{\text{Ly}}}^{\infty} F_V \sigma_V dV = n^2 \eta^2 \alpha_B, \quad (4.20)$$

which can be rewritten for the plane-parallel, monochromatic case in terms of the ionization degree (cf Eq. 4.4) as

$$\frac{d\eta}{dx} = \eta^2 \frac{1 - \eta}{1 + \eta} n \bar{\sigma} x_s. \quad (4.21)$$

This equation can be solved numerically and gives the ionization degree η at any given position x for the chosen number density n and mean cross-section $\bar{\sigma}$.

To test the code, we ran three simulations:

- Case A: 125k particles placed on a Cartesian grid
- Case B: 100k particles placed randomly
- Case C: 250k particles placed randomly

For cases B and C the particles are placed randomly in the simulation box and then are allowed to relax with periodic boundaries and the inclusion of hydrodynamics for one crossing timescale to dampen the numeric random noise. Thereafter we switch off the hydrodynamics and compute the ionization. For all simulations we used a mean density $n = 10 \text{cm}^{-3}$. The simulated volume is $(2 \text{pc})^3$, the length the ionization can penetrate is set to $x_s = 1 \text{pc}$. The recombination coefficient and the absorption cross-section are set to typical values of $\alpha_B = 2.7 \times 10^{-13} \text{cm}^3 \text{s}^{-1}$ and $\bar{\sigma} = 3.52 \times 10^{-18} \text{cm}^2$. For the above parameters, $F_{\text{Ly}} = 8.33 \times 10^7 \text{photons cm}^{-2} \text{s}^{-1}$ and $t_{\text{rec}} = 11.8 \text{kyr}$. The simulations run up to $t = 5t_{\text{rec}}$ to allow for a quasi-equilibrium state to evolve.

In Fig. 4.1 the time evolution of the penetration length $x_I(t)$ is shown. The position of the front is calculated by projection of the three-dimensional simulation along the y- and z-axis onto the x-axis. Note that the analytical solution (cf Eq. 4.19) is based on the idealized assumption that the medium is fully ionized ($\eta = 1.0$). However, the precise solution of Eq. 4.5 in equilibrium ($d\eta/dt = 0$) is

$$x_s \eta^2 = \frac{V_s}{S} = \frac{F_{\text{Ly}}}{\alpha_B n^2}. \quad (4.22)$$

In our simulations $x_s \eta^2 = 1 \text{pc}$ is realized with $x_s = 1.05 \text{pc}$ and $\eta = 0.976$. We call this the exact solution whereas the solution assuming $\eta = 1.0$ will be referred to as classic solution. Our simulations converge very well towards the exact solution. Case A, where the particles are initially placed on a grid, slightly overestimates the final value of x_s , while the low resolution simulation (case B) underestimates it. Nevertheless, already with only 100k this implementation shows a very good agreement with the analytical curve. In the high resolution simulation (case C) the numerical result lies right on top of the predicted line.

Fig. 4.2 shows the ionized fraction η and the neutral fraction $\chi = 1 - \eta$ after $t = 5t_s$ at the end of the simulation. The numerical solution of Eq. 4.21 is evaluated for the exact solution

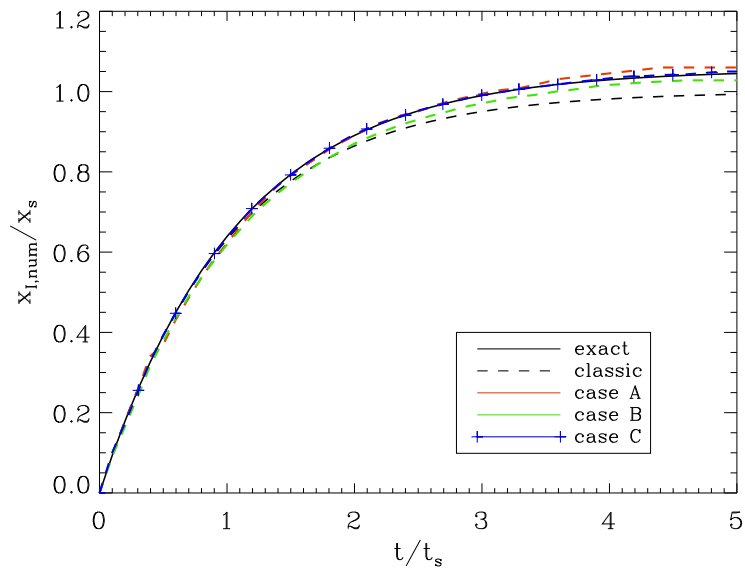


Figure 4.1: Time evolution of the ionization degree η for the three test cases with different particle numbers and distributions red (125k particles), green (100k particles) and blue (250k particles) lines. The black solid line denotes the exact solution, the black dashed line the classic (Strömgren) solution.

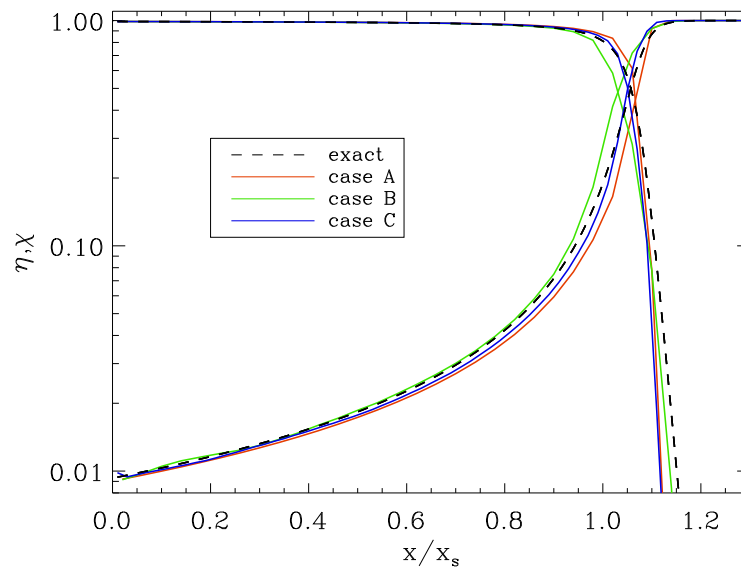


Figure 4.2: Ionization degree η (≈ 1 at $x/x_s = 0$) and neutral gas fraction $\chi = 1 - \eta$ versus position for the cases A (red), B (green) and C (blue). The dashed line represents the exact solution.

with a penetration length of $x_s = 1.05$ pc. As expected from Fig. 4.1, case A overestimates the front position, whereas case B underestimates it. Again the high resolution run C shows the best concordance and we can conclude that these results fit well within the range of the code comparisons done by Iliev et al. (2006). A more direct comparison to this work is not possible due to the plane-parallel nature of the test performed here.²

Ionization by a time-varying source

A more challenging test is the treatment of a time-varying source of ionization. Although this situation is not very realistic for an O-star it nevertheless provides a very good method to test the treatment of a rapidly changing flux by the code.

To produce an ionization front that is traveling at a constant speed through a medium of constant density it is sufficient to increase the flux per area F_{Ly} linearly with time,

$$F_{Ly}(t) = nv_f + n^2\alpha_B v_f t, \quad (4.23)$$

where v_f denotes the speed of the ionizing front. The first term on the right hand side provides the ionization of the front, while the second term compensates for the loss of flux due to recombinations on the way towards the front. We assume a constant density of $n = 10\text{cm}^{-3}$ and the velocity of the front is set at $v_f = 1.3 \times 10^5 \text{cm s}^{-1}$. The other parameters are chosen as before.

Again the three initial conditions A, B and C from section 4.3.1 are explored. The results are shown in Fig. 4.3. As before the simulations match the theoretical solutions closely. In the beginning run A agrees very well with the solution. This is due to the very low numerical noise in the Cartesian grid. However, towards the end the low resolution leads to a deviation from the analytic value. In case B one can clearly see the effect of the noisy density distribution, since for the recombination R any error in the density leads to a quadratic error in the absorption of the photons (cf Eq. 4.7). Therefore, the position starts to oscillate around the exact position. This effect gets stronger the further the front penetrates, as more material has to be kept from recombining. Case C shows a very good agreement with the exact solution, the resolution is high enough to keep the noise in the density distribution low and thus the position of the front is followed precisely.

Testing the refinement - Ionization by a constant source in a two-density medium

All tests up to now were independent of the implementation of refinement, since in a constant density medium each particle occupies roughly the same diameter d_{part} (see Section 4.2.2). To verify the correct implementation of the refinement we set up a simulation with a two-density medium. A lower density gas phase with $n_1 = 10\text{cm}^{-3}$ is set up in the left half of the box and a higher density medium with $n_2 = 100\text{cm}^{-3}$ is placed at the right half of the box. The density contrast is achieved via a different number of SPH-particles in the different regions, the particle

²Note that in Fig. 4.2 the neutral fraction χ converges towards a value of 10^{-2} at $x = 0$ pc in both the simulations and the exact solution whereas in Iliev et al. (2006) χ is reaching much lower values. This is due to the fact that in our simulations the irradiated surface stays constant whereas when simulating a point source this surface and thus χ can get infinitesimally small.

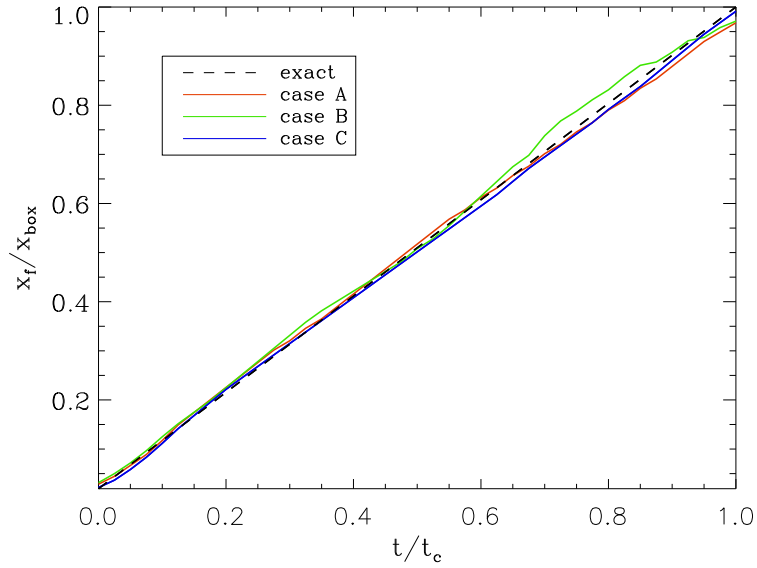


Figure 4.3: Numerical simulation of an ionization front that moves with constant speed through a medium of constant density. Plotted is the position of the front in units of the box length versus the time in units of the crossing time for the three cases A (red), B (green) and C (blue).

masses are equal in the entire simulation. The required flux to ionize the simulation domain up to a position x_s can be calculated by linear superposition according to Eq. 4.22

$$F_{Ly} = \alpha_B x_1 n_1^2 + \alpha_B (x_s - x_1) n_2^2, \quad (4.24)$$

where $x_1 = 0.5$ pc is the extent of the low-density region. The simulation is set up with 550k randomly placed particles. The particle noise is reduced for both regions separately as described in Section 4.3.1. The penetration depth is set to $x_s = 1$ pc. As soon as the equilibrium state is reached the numerically calculated penetration lengths are

$$x_{\text{eq,unrefined}} = 0.985 x_s \quad ; \quad x_{\text{eq,refined}} = 0.997 x_s \quad (4.25)$$

for the unrefined and the refined case. Very good agreement even with the unrefined code can be expected, as we always use the SPH-density in the calculation which is independent of the chosen bins for the calculation of the ionization and the recombination.

Nevertheless, the refinement has an important geometric effect, which becomes clear when assuming a density contrast with a discontinuity which is not aligned vertical to the impinging radiation. We perform a test with a diagonal density contrast between two regions with a number density of $n_{\text{low}} = 10\text{cm}^{-3}$ and $n_{\text{high}} = 200\text{cm}^{-3}$ respectively. Again the particles are placed randomly and the noise is reduced (see Section 4.3.1). A cubic domain of $(0.5 \text{ pc})^3$ including 25k particles is shown in Fig. 4.4. In the unrefined case (left hand side) the effect of the original bin-size of ≈ 0.05 pc can be clearly seen as step-like features. With refinement the density contrast of

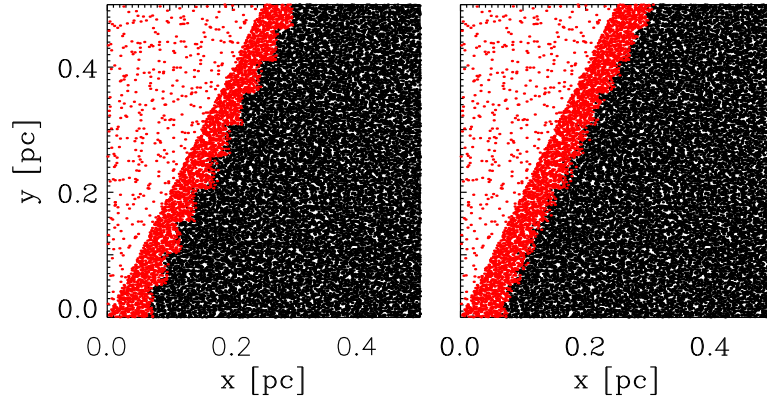


Figure 4.4: Effect of the refinement on a diagonal density step. Plotted are the SPH-particles in a $(0.5 \text{ pc})^3$ volume projected along the z-axis. Red: ionized particles ($\eta > 0.1$), black: unionized particles. Left: without the inclusion of refinement. Right: with the inclusion of one level of refinement.

20 leads to one level of refinement (since $d_{\text{part}}/\Delta y \approx 1/2.7$, cf Eq. 4.12) and the geometrical bias is already negligible (Fig. 4.4, right hand side). In the simulations in Section 4.4 all five levels of refinement lead to spatial resolution of the radiation in our simulations as high as 10^{-3} pc , therefore the radiation does not produce any unphysical geometrical effects.

4.3.2 Ionization with Hydrodynamics

Steady propagation of an ionizing front

This test was originally proposed by Lefloch & Lazareff (1994). An area of constant density is ionized by a photon flux which increases linearly with time. This leads to a hydrodynamical shock wave traveling at a constant speed. The number densities n_i, n_c, n_0 in the ionized, the compressed and the undisturbed medium can then be calculated from the corresponding sound speeds a_i, a_c, a_0 . Let u_i be the speed of the ionization front and u_s be the speed of the shock front. The jump condition for a D-type ionization front can be written as

$$\frac{n_i}{n_c} = \frac{a_c^2}{a_i^2} = \frac{a_0^2}{a_i^2}, \quad (4.26)$$

since the compressed and the neutral medium have the same temperature and thus the same sound-speed. At the isothermal shock the jump conditions are

$$u_s(u_s - u_i) = a_0^2, \quad (4.27)$$

$$\frac{n_c}{n_0} = \frac{u_s^2}{a_0^2}, \quad (4.28)$$

where u_1 is the gas velocity just inside the shock. With the approximation of a thin shock it can be assumed that the ionization front and the shock front have the same speed $u_i = u_s$. For a detailed derivation of the jump conditions see e.g. Shu (1991b). Introducing the time derivative of the ionizing flux $C = dF/dt$ the speed of the front can be calculated similar to Eq. 4.17:

$$u_i = \frac{C\alpha_B}{n_1^2} (= u_s). \quad (4.29)$$

The jump conditions can then be rewritten to give the following relations:

$$n_c = n_0 \frac{u_s^2}{a_0^2} = n_0 \left(\frac{C}{\alpha_B n_1^2 a_0} \right)^2 \quad (4.30)$$

$$n_i = n_c \frac{a_0^2}{a_1^2} = \left(\frac{n_0 C^2}{\alpha_B a_1^2} \right)^{\frac{1}{5}} \quad (4.31)$$

$$u_1 = u_s - \frac{a_0^2}{u_s}. \quad (4.32)$$

To compare directly to previous results, we used the initial conditions by Lefloch & Lazareff (1994). The density is $n_0 = 100\text{cm}^{-3}$, the temperature is $T_{\text{cold}} = 100\text{K}$. The flux increases linearly with time at a constant rate of $dF/dt = 5.07 \times 10^{-8}\text{cm}^{-2}\text{s}^{-2}$, starting from zero. As before the recombination parameter is set to $\alpha_B = 2.7 \times 10^{-13}\text{cm}^3\text{s}^{-1}$ and the ionized temperature is $T_{\text{hot}} = 10^4\text{K}$. Refinement is included.

The simulations are performed using the individual particle time-steps of VINE. For the determination of the time-step we use the criteria given in Wetzstein et al. (2008). Here we will only review briefly the parameters used. We use a combined time-step criterion based on the change in acceleration and velocity of the particle with an accuracy parameter of $\tau_{\text{acc}} = 1.0$. In addition, a CFL criterion is used with a tolerance parameter of $\tau_{\text{CFL}} = 0.3$ and the modifications discussed in Section 4.2.3. We also use an additional time-step criterion based on the maximum allowed change of the smoothing length (see Wetzstein et al., 2008, for details) with an accuracy parameter of $\tau_h = 0.15$. VINE employs a variable and time-dependent smoothing length, the number of neighbours of each particle is on average $n_{\text{neigh}} = 50$, but variations of ± 20 are allowed. The artificial viscosity of the SPH method is included in the standard way (Gingold & Monaghan, 1983) with the parameters $\alpha = 1$ and $\beta = 2$ as implemented in VINE.

We performed simulations with 1 and 2 million particles in a cubic simulation domain. The particles are distributed randomly and then left to relax according to Section 4.3.1. The higher resolution compared to the test in Section 4.3.1 is necessary to follow the hydrodynamical shock precisely. As in the tests before, assuming a fully ionized gas with $\eta = 1.0$ and thereby using a value of $T_{\text{hot,a}} = 10^4\text{K}$ for the calculation of the sound-speed of the hot gas, does not correspond to the simulations (see equation 4.22). Instead a much better agreement can be achieved when the real temperature of the gas in the simulations, $T_{\text{hot,r}} = 9200\text{K}$, is used (since $\eta = 0.92$ on average in the ionized region). For this more realistic temperature the simulations are in very good agreement and converge towards the analytic solution with increasing resolution (see Fig. 4.5). This can also be seen in Table 4.1.

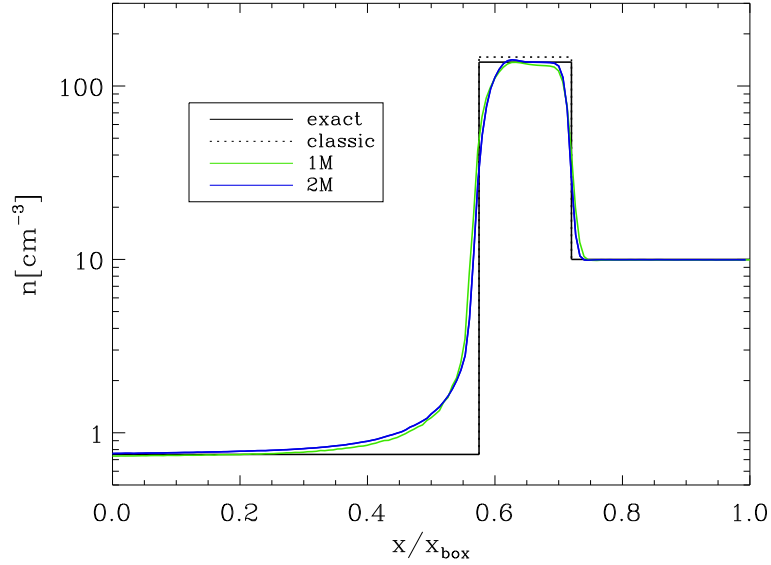


Figure 4.5: Number density versus position for the steady propagation of an ionizing front. The dashed line shows the classic solution, obtained by using a value of $T_{\text{hot,a}} = 10^4 \text{K}$ for the hot gas. The solid line corresponds to the analytic solution for a more realistic value of $T_{\text{hot,r}} = 9200 \text{K}$ for the hot gas. Blue and green lines show the simulations at different resolutions.

	Classic	Exact	Grid	SPHI	iVINE
$n_c (\text{cm}^{-3})$	147	137	169	155	138 ± 6
$n_i (\text{cm}^{-3})$	0.734	0.747	0.748	0.75	0.743 ± 0.01
$u_i (\text{km s}^{-1})$	3.48	3.37	3.36	3.43	3.34 ± 0.18
$u_1 (\text{km s}^{-1})$	3.24	3.12	-	-	3.13 ± 0.04

Table 4.1: Comparison of analytical and numerical results for the test including hydrodynamics and ionization. The iVINE data is obtained from the 2 million particle run, the errors given are 1σ . The grid data is taken from Lefloch & Lazareff (1994), the SPHI data from Kessel-Deynet & Burkert (2000). The analytical values differ from the previous work due to a higher accuracy in our calculations.

4.3.3 Performance

To test the performance of the parallel iVINE code with increasing number of processors we choose the simulation described in Section 4.4 at a later stage and compute one time-step on different numbers of CPUs. The parallel scaling of the various parts of the underlying VINE code is discussed in detail in Nelson et al. (2008). For our test, we use a SGI Altix 3700 Bx2 supercomputer. In total, the ionization uses only a few percent of the total computational time. The precise values range from 2.32% on 2 CPUs to 2.70% on 16 CPUs and 2.86% on 32 CPUs.

When refinement is used, these values change to 8.52% on 2 CPUs and 8.73% on 32 CPUs. Although the ionization takes up relatively more time in this case, the difference in the calculation time between the number of CPUs gets smaller. This is to be expected, as the refinement is calculated inside the bins and this part of the implementation is parallelized very efficiently (each bin is independent of the other bins).

This test shows that the additional cost of our implementation of ionizing radiation in SPH is always much smaller than the cost for other implemented physics, like gravity and hydrodynamics. In particular, our new ray-tracing-scheme shows a substantial speedup compared to the algorithm by Kessel-Deynet & Burkert (2000), where the path-finding alone took up about 50% of the total computational time (Kessel-Deynet, 1999). Another drawback of their approach is that for every particle the optical depth is calculated along a path towards the source until a particle closer to the source with an already calculated optical depth is found. This is a highly serial approach and thus the scheme of Kessel-Deynet & Burkert (2000) does not lend itself easily to an efficient parallelization.

4.4 Radiation Driven Implosion

As a first application of iVINE we model the radiation driven implosion of an otherwise stable molecular cloud core. This approach is very similar to Kessel-Deynet & Burkert (2003) but at ten times higher mass resolution. A marginally stable Bonnor-Ebert sphere (BES) (Bonnor, 1956) with a radial pressure profile defined by

$$\frac{1}{r^2} \frac{d}{dr} \left(\frac{r^2}{\rho} \frac{dp}{dr} \right) = -4\pi G \rho \quad (4.33)$$

is exposed to UV-radiation from a nearby source. The temperature of the sphere is $T = 10\text{K}$, the peak density is $n_{\text{max}} = 10^3 \text{cm}^{-3}$, and the gas is initially at rest (i.e. no turbulence). The total mass contained in the sphere is $96M_{\odot}$ and the radius is 1.6pc . We embed the sphere into cold gas (10K) with a constant density corresponding to the cutoff-density at the edge of the sphere. These simulations were performed with 2.2×10^6 particles resulting in a particle mass of $7.2 \times 10^{-5} M_{\odot}$. Self gravity is included. The cooling timescale ($t_{\text{cool}} < 0.3\text{kyr}$) is much shorter than any other timescale involved in our simulations (e.g. the crossing timescale of the hot gas is $t_{\text{hot}} \approx 70\text{kyr}$). Thus, we treat the non-ionized gas with an isothermal equation of state ($\gamma = 1$). The ionized gas is assigned a temperature according to Eq. 4.9 with $T_{\text{hot}} = 10^4\text{K}$ and $T_{\text{cold}} = 10\text{K}$ and then treated isothermally as well.

The artificial viscosity and the criteria for the individual time-steps are the same as in Section 4.3.2 ($\alpha = 1$, $\beta = 2$, $\tau_{\text{acc}} = 1.$, $\tau_{\text{CFL}} = 0.3$ and $\tau_{\text{h}} = 0.15$). In addition, we use a multipole acceptance criterion (MAC) for the tree based calculation of gravitational forces according to Springel et al. (2001) as implemented by Wetzstein et al. (2008) with a tree accuracy parameter of $\theta = 5 \times 10^{-4}$. The implementation of the SPH smoothing kernel and the gravitational softening length in VINE are equal at all times. The number of neighbours is set to $n_{\text{neigh}} = 50 \pm 20$. The hydrodynamical boundaries are periodic in the y- and z- direction, and open in the x- direction. This resembles the situation around a massive O-star where the material is allowed to move freely in the radial direction while at the sides similar material is existing. Gravitational forces are calculated by just taking into account the self-gravity of the gas and no external or boundary effects. This is reasonable as the total simulation time ($< 600\text{kyr}$) is much shorter than the free-fall time ($t_{\text{ff}} \approx 1.5\text{Myr}$). In the simulations the radiation is impinging from the left hand side. We perform three different simulations, differentiated by the penetration length in the surrounding medium relative to the box size $C = x_{\text{s}}/x_{\text{box}}$:

- Simulation HF (high flux):

$$F_0 = 9.0 \times 10^9 \text{photons cm}^{-2}\text{s}^{-1} \Rightarrow C \approx 1.0$$

- Simulation IF (intermediate flux):

$$F_0 = 4.5 \times 10^9 \text{photons cm}^{-2}\text{s}^{-1} \Rightarrow C \approx 0.5$$

- Simulation LF (low flux):

$$F_0 = 9.0 \times 10^8 \text{photons cm}^{-2}\text{s}^{-1} \Rightarrow C \approx 0.1$$

This corresponds to the molecular cloud being placed inside (HF), at the border (IF) and outside (LF) of the Strömgen sphere. The evolution of the BES for all three cases is shown in Fig. 4.6.

4.4.1 Dynamical Evolution

The general evolution of a simulation of this kind is as follows: As soon as the simulation starts, a R-type ionization front is driven into the medium. As it can be expected from Section 4.3.1, the front reaches the Strömgen radius x_{s} of the diffuse gas within a few recombination timescales ($5t_{\text{rec}} \approx 5\text{kyr}$). After a sound crossing timescale ($t_{\text{hot}} \approx 70\text{kyr}$) the hot gas reacts to its change in pressure and starts to drive a shock front into the cold gas - a D-type front evolves. This front will affect the morphology of the BES. In the following we describe the individual cases in more detail.

Simulation HF (high flux)

Due to the high flux (see Fig. 4.6 first column), the R-type front is able to propagate very far into the simulation domain. A bow-like shock structure around the edge of the BES evolves ($t \approx 100\text{kyr}$). The shock front running into the denser parts of the cloud is slowed down, so that the

front starts to "wrap around" the cloud. Soon the two flanks are approaching each other while the center of the shock is held back by the dense innermost region (Fig. 4.6 third row, first column, $t \approx 100$ kyr). As the two sides finally collide an elongated filament forms which is gravitationally unstable. In Fig. 4.7 we show this filament at the final stage of our simulations. In comparison runs without self-gravity the two shock fronts cross each other and the cloud disperses. With the inclusion of self-gravity the filament becomes gravitational unstable and is triggered into collapse. In fact the core fragments into several objects, as will be discussed in a subsequent paper. The resolution limit according to Bate & Burkert (1997) is $n_{\max} = 2 \times 10^{10} \text{cm}^{-3}$ in these simulations. As soon as this limit is reached the local Jeans mass is smaller than the mass of 100 particles and artificial fragmentation can occur. Thus, we stop the simulations at this point.

Simulation IF (intermediate flux)

With an intermediate flux the R-type front penetrates much less into the gaseous medium (see Fig. 4.6 second column). Thus, the front does not wrap around the sphere as much as in Simulation HF. As soon as the hot gas reacts to its increased temperature a flattened shock with a much smaller curvature than in Simulation HF forms. In addition, the motion in the hot gas forces the flanks on both sides of the main shock inwards, which can be seen in the velocities of the hot gas in Fig. 4.6 (third row, second column, $t \approx 100$ kyr). These motions are due to the periodic boundaries on the upper and lower edge. Otherwise the gas could stream away freely. However these boundaries are justified by the fact that the molecular cloud is completely surrounding the O-star. In the further evolution the flanks approach each other similar to Simulation HF and the central region becomes unstable and fragments (see Fig. 4.7).

Simulation LF (low flux)

The very low flux in this case only leads to a R-front which barely reaches the sphere (see Fig. 4.6 third column). Therefore, the D-front starts as a nearly plane-parallel shock wave in front of the BES. This shock sweeps away much more material than in the high and intermediate flux cases, where the material is concentrated in the center. Nevertheless, as the shock propagates further the very center of the sphere gets compressed and becomes gravitationally unstable. In contrast to Simulations HF and IF there is no sign of fragmentation in the unstable region.

4.4.2 Structure, Collapse Timescales and Final Mass Assembled

A close look at the final structure of the collapsing filaments of the three simulations (Fig. 4.7) reveals that in all three simulations the core forms at the tip of an elongated filament, which might be eroded in the future. This matches exactly the observed head to tail structure described in Section 1. The core regions have an extent of just $0.02 - 0.05$ pc, which corresponds very closely to e.g. the findings of Motte & André (2001) in the the Perseus star cluster. They observe 8 Class 0 protostars with compact envelopes ($R_{\text{out}} < 10^4 \text{AU} \approx 0.05$ pc). In addition they are denser by a factor of 3-12 than it would be expected from the standard collapse model, which would suggest densities of $n \approx 10^6 \text{cm}^{-3}$ (see e.g. Walch et al. 2008, in preparation). Motte & André

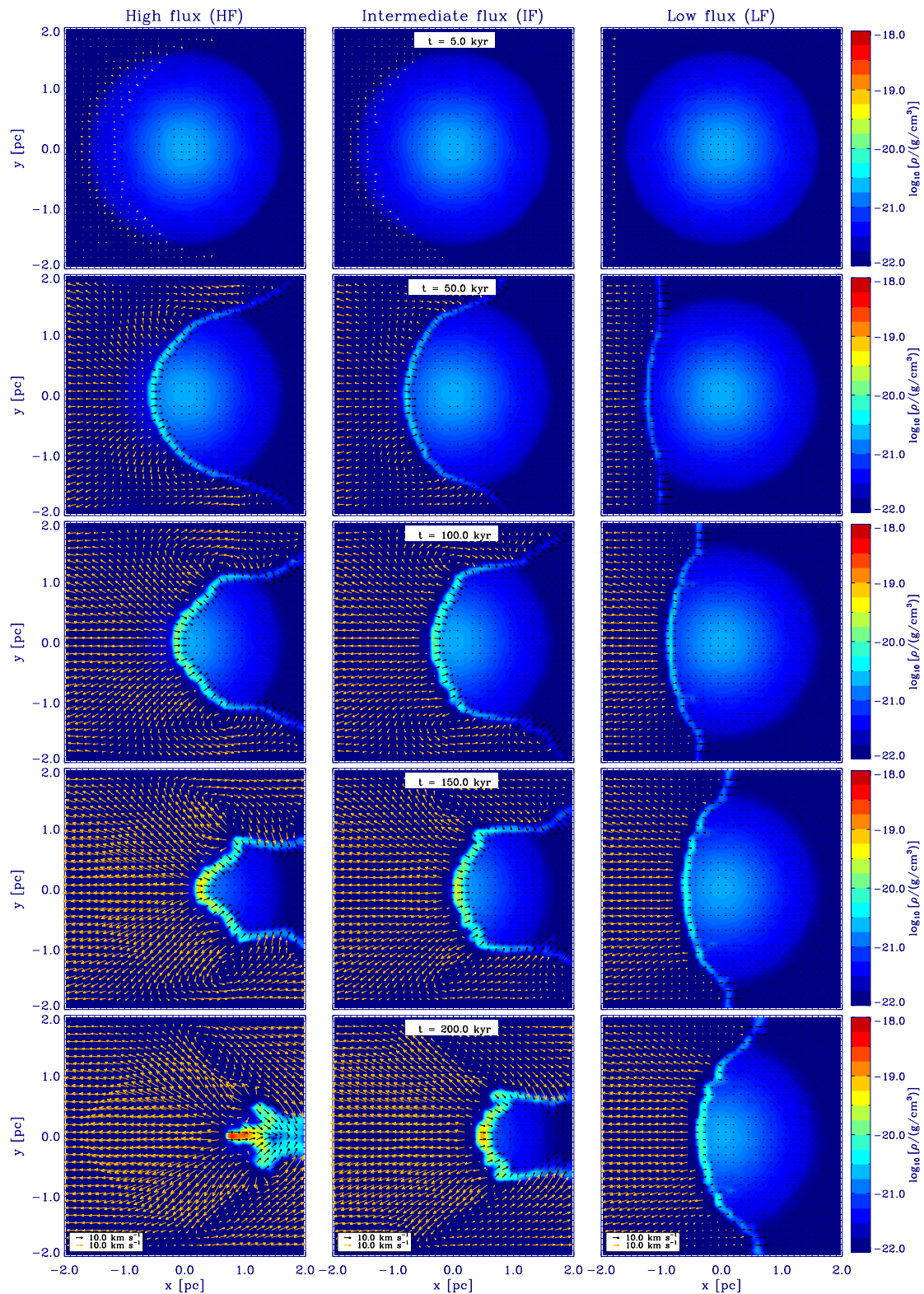


Figure 4.6: Time evolution of the driven collapse of a Bonnor-Ebert sphere ionized by a source with high flux (first column), intermediate flux (second column) and low flux (third column). The simulation volume is a cube with sides 4 pc long, the UV-radiation is impinging from the left hand side. Color coded is the density of the central cold gas slab. Yellow arrows denote the velocities of the hot gas, black arrows the motion of the cold gas. Density and velocities are averaged across a slice of 0.125 pc in the z-direction. Each row shows the three simulations at a different time.

(2001) suggest that this higher densities are due to external disturbances initiating the collapse, which agrees very well with our simulations. Following the observations we define a core as all material with a density higher than $n_{\text{crit}} = 10^7 \text{cm}^{-3}$ in a region of $R_{\text{crit}} = 0.02 \text{pc}$ (which is roughly a Jeans length at a density of n_{crit}) around the peak density.

We plot the evolution of the maximum density in Fig. 4.8. In all three simulations after the first phase of compression by the hot gas a meta-stable phase at densities between 10^6cm^{-3} and 10^7cm^{-3} can be seen. This fits very nicely to the structure of observed cores described above. The duration of this phase depends on the initial flux (HF: 90 kyr, IF: 155 kyr, LF: 290 kyr). In addition, we find evidence that the filaments collapse earlier in cases with a higher flux. The collapse happens at $t = 200 \text{kyr}$, $t = 280 \text{kyr}$ and $t = 600 \text{kyr}$ in Simulation HF, IF and LF, respectively. Observations of triggered star formation tend to show the same trend (see Lee et al. 2005, Ikeda et al. 2008) - the younger the star, the further it is away from the ionizing source. This can not be explained by just attributing it to the speed of the R-type front. As seen in Section 4.3.1 the crossing time for the R-type front is of the order of a few kyr, whereas any observed age-spread is of the order of several hundred kyr. To explain this huge spread the position of the density enhancement relative to the Strömgren radius has to be considered. As we show decreasing the flux and thereby increasing the distance to the source can delay collapse and star formation by 0.08 – 0.4 Myr.

In IC 1396N Getman et al. (2007) report a T Tauri (Class II and Class III stars) population with ages $\approx 0.5 - 1 \text{Myr}$. In addition, 0.3 – 0.5 pc further away from the ionizing source HD 206267 (an O6.5f-type star), there is an embedded population of Class 0/I protostars with ages $\approx 0.1 \text{Myr}$. This can be compared to our simulations where e.g Simulation IF represents gas clumps closer to the source which start to form stars 0.3 Myr earlier than Simulation LF. So at the time the embedded stars start to form in Simulation LF the stars of Simulation IF would be no longer embedded and represent the Class II/III stars population. In fact in our simulations the spread of a few hundred kyr is smaller than in the observations. This difference could be attributed to the classification of the protostars as discussed below.

Besides the age-spread one can look at the velocities of the front and core. From Fig. 4.6 it can be seen that the shock front travels with a speed of 3 – 7 km/s, depending on the initial flux. Most observational estimates provide a front speed $< 1 \text{km/s}$ (Thompson et al., 2004), leading to a difference of almost an order of magnitude between observations and simulations which has been noted before (see e.g. Getman et al. 2007). The age estimates of the YSOs are mainly based on their classification by the spectral energy distribution (SED). A Class 0/I object is deeply embedded, therefore the short micrometer wavelengths are much weaker due to absorptions in the envelope when compared to Class II/III objects. This allows for a clear distinction between both types e.g. in the IRAC [3.6] – [4.5] versus [5.8] – [8] color diagram as shown by Hartmann et al. (2005). We suggest that in the case of triggered star formation, the ionizing radiation could strip the envelope of a YSO, thereby unveiling the central object in short micrometer wavelengths. Thus, the observed Class II/III SED could be caused by a much younger Class 0/I protostar with a removed envelope. This would reduce the estimated age spread, thereby increasing the estimated speed of the shock front and finally leading observations and simulations to agree. This assumption will be subject to further examination.

A dependence on distance is also seen for the velocities of the cold filaments (see the ve-

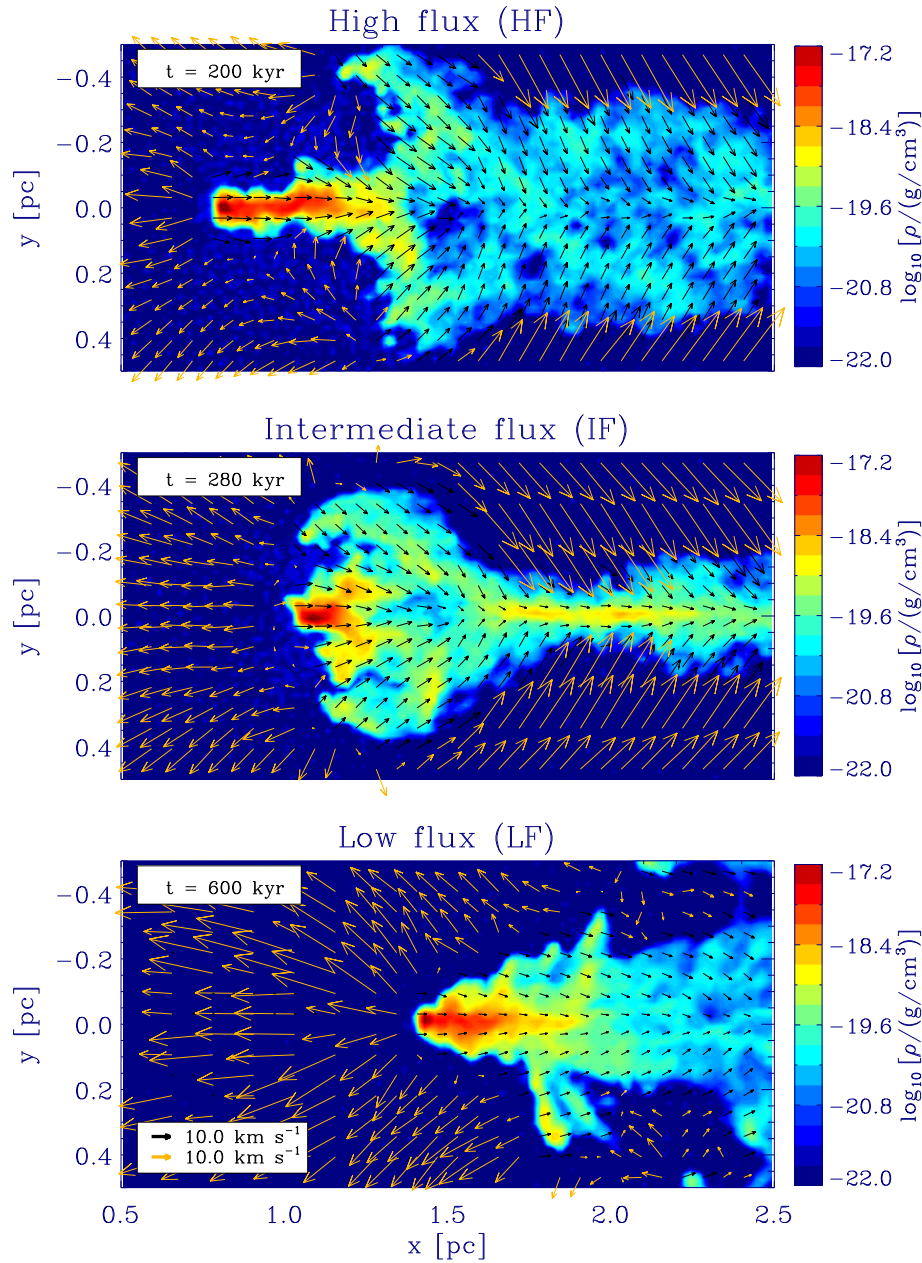


Figure 4.7: Final stage of the three simulations. Color coded is the density in the central slab. Yellow arrows denote the velocities of the hot gas, black arrows the motion of the cold gas. Density and velocities are averaged across a slice of 0.0625 pc in the z -direction. The time of the collapse as well as the displacement of the fragment clearly depend on the initial flux. Furthermore the velocity of the cold gas (black arrows) is decreasing with decreasing flux. The core always forms at the very tip of the filament.

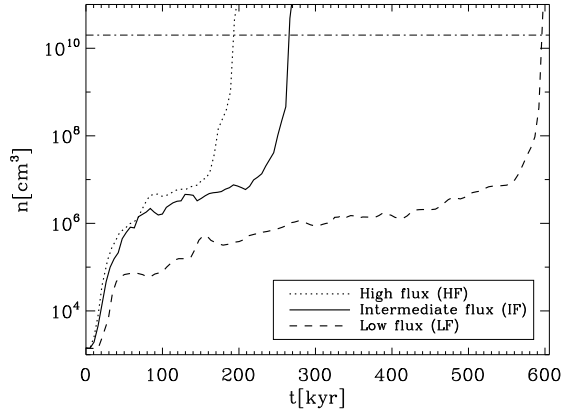


Figure 4.8: The maximum number density versus time for the three different simulations. In the higher flux cases HF and IF the collapse happens much earlier than in the low flux case LF. The dash-dotted line represents the resolution limit as given by Bate & Burkert (1997).

locities of the cold gas (black arrows) in Fig. 4.7). The precise velocities of the cores in the Simulations HF, IF and LF are 8.4km/s, 7.6km/s and 5.1km/s, respectively. Again, the closer the core is to the OB-association the higher is its velocity. Although these small differences are not observable yet it is worth noticing that the cores themselves have bulk velocities which are slightly higher (by about 0.5 – 1km/s) than the rest of the filament. However, this effect may get weaker as the core gets slowed down while sweeping up the rest of the filament.

The final mass assembled does not show a dependence on the initial distance. In Simulation HF the core consists of $6.0M_{\odot}$ in Simulation IF of $7.4M_{\odot}$ and in Simulation LF of $2.8M_{\odot}$. The filaments as a whole have masses of $61.5M_{\odot}$, $75.3M_{\odot}$ or $67.4M_{\odot}$, respectively. It is obvious that the most effective scenario is Simulation IF. Here, the ionization encompasses most of the sphere and thus the shock front is not nearly as plane-parallel as in Simulation LF and does not sweep away as much material. On the other hand, less material gets evaporated by the ionization since the flux is lower than in Simulation HF. Overall the final masses of the collapsing cores fit the observations well. Assuming a star formation efficiency of 30% (see e.g. Lada et al. 2008), we find masses from $0.84M_{\odot}$ to $2.2M_{\odot}$ which agrees with the observed range from classical T Tauri up to Herbig Ae/Be stars (see e.g. Lee & Chen 2007, Snider et al. 2007).

4.5 Summary and Discussion

We present iVINE, a new implementation of UV-radiation into the tree-SPH code VINE. It uses a plane-parallel geometry which renders the code most suitable to perform high resolution studies of the small scale effects of e.g. ionization and turbulence in the surrounding of young massive stars. It is efficiently parallelized and very fast, as only 2%-8% of the total computational time are used for the calculation of ionization. The comparison with analytic solutions shows that

iVINE treats time-dependent ionization as well as the resulting heating effects precisely and convergently.

We base our numerical implementation of ionizing radiation on several assumptions. First, we use a simplified prescription for the radiative transfer by e.g. assuming a monochromatic flux. Second, we neglect UV absorption by dust, which would lower the total UV flux. Third, we do not include a full treatment of recombination zones. In our simulations the ionized gas which gets shaded is assumed to recombine immediately. In addition, the gas in the shaded regions does not get heated by irradiation from the hot gas surrounding it. These effects require a precise time-dependent treatment of heating and cooling processes by ionization and recombination as well as a treatment for the scattering of photons. An implementation of these effects is planned in a future version of the code.

As an application we investigate radiation driven implosion of a marginally stable Bonnor-Ebert sphere. We show that these spheres are indeed driven into gravitational collapse. The resulting cores are in the observed mass range. They are more compact and a factor of ≈ 10 more dense than it would be expected in a more quiescent environment. This fact fits very well with the observations of star formation in a clustered environment. By comparing simulations with three different UV-fluxes we show that there is a clear dependence of the final mass and the age of the collapsed core on the position of the preexisting density enhancement relative to the Strömgen radius. Our findings that the onset of star formation is delayed by 0.08 – 0.4 Myr, depending on the position, are in good agreement with observations of the age spread in bright rimmed clouds. The velocity of the triggering shock is an order of magnitude higher than the observational estimates. This discrepancy has been noted before. We suggest that this can be attributed to the ionizing radiation stripping the envelope from a Class 0/I star. Thereby it might be classified as an Class II/III star, leading to an higher age-spread between the observed objects. Correcting for this effect would increase the estimated velocity of the shock front and thus lead simulations and observations towards agreement.

Acknowledgments

We would like to thank the referee, James Dale, for his valuable comments on the manuscript.

This research was supported by the Deutsche Forschungsgesellschaft (DFG), SFB 375 and by the DFG cluster of excellence "Origin and Structure of the Universe".

All simulations were performed on a SGI Altix 3700 Bx2 supercomputer that was partly funded by the DFG cluster of excellence "Origin and Structure of the Universe".

Chapter 5

Driving Turbulence and Triggering Star Formation by Ionizing Radiation

¹M. Gritschneider, T. Naab, A. Burkert, S. Walch, F. Heitsch

We present high resolution simulations on the impact of ionizing radiation of massive O-stars on the surrounding turbulent interstellar medium (ISM). The simulations are performed with the newly developed software iVINE which combines ionization with smoothed particle hydrodynamics (SPH) and gravitational forces. We show that radiation from hot stars penetrates the ISM, efficiently heats cold low density gas and amplifies over-densities seeded by the initial turbulence. The formation of observed pillar-like structures in star forming regions (e.g. in M16) can be explained by this scenario. At the tip of the pillars gravitational collapse can be induced, eventually leading to the formation of low mass stars. Detailed analysis of the evolution of the turbulence spectra shows that UV-radiation of O-stars indeed provides an excellent mechanism to sustain and even drive turbulence in the parental molecular cloud.

stars: formation — ISM: structure — turbulence — ultraviolet: ISM — methods: numerical

5.1 Introduction

Some of the most spectacular structures in the molecular ISM are observed in the vicinity of hot O/B-stars or associations, e.g. the Horsehead nebula (B33), the three pillars of creation in M16 and the Elephant trunk (BRC37) in IC1396. For the pillars in M16 Sugitani et al. (2002) find a head to tail structure with the denser head pointing toward the OB stars of NGC661. In addition, young stellar objects (YSOs) are present at the tips of the pillars. In the Horsehead nebula Ward-Thompson et al. (2006) report two core-like structures that might undergo subsequent gravitational collapse. Very recent observations by Ikeda et al. (2008) report several YSOs close to the tip of BRC37. As a common feature these pillar-shaped nebulae point toward a source of ionizing radiation and show signs of present or future star formation at their tips.

Up to now the precise physical processes leading to the formation of these structures are not fully understood. The morphologies suggest that feedback effects of UV-radiation and winds of massive stars play an important role in the formation of the pillars. In addition, the radiation

¹published as 2009, ApJ, 694, L26

might have a strong impact on the overall evolution of the parental cloud. Furthermore, molecular clouds are observed to be highly turbulent structures. There is evidence that this turbulence can support the clouds against gravitational collapse and thereby control star formation. As hydrodynamic and MHD turbulence decays rather quickly, the only way to explain this high level of turbulence would be to drive the turbulence - either on large scales by i.e. supernova explosions or on small scales from within the cloud by stellar outflows, winds or ionization (see e.g. Elmegreen & Scalo 2004 and Mac Low & Klessen 2004, for reviews). The possibility of ionization driven turbulence has been indicated by e.g. semi-analytic models of Krumholz et al. (2006). In this Letter we test the hypothesis using high resolution numerical simulations with the newly developed code iVINE (Gritschneider et al., 2009a, hereafter G09).

On the theoretical side progress has been made since Elmegreen et al. (1995) first presented two-dimensional, grid-based simulations showing that the expansion of an HII region into the surrounding ISM can trigger star formation by sweeping up the cold material. This is called 'collect and collapse'. Another proposed scenario is the 'radiation driven implosion', where preexisting density structures are driven into collapse (see e.g. Bertoldi 1989, Kessel-Deynet & Burkert 2003 and G09).

For the numerical treatment of radiation in simulations several codes have been developed (see Iliev et al. 2006 and references therein). Recent applications for the treatment of ionizing radiation in grid based codes include e.g. Mellema et al. (2006) and Krumholz et al. (2007). In SPH-codes implementations have been presented by Dale et al. (2005), Pawlik & Schaye (2008) and Altay et al. (2008). Simulations by Dale et al. (2007b) show that ionizing radiation can slightly enhance the formation of cores in a globally unbound molecular cloud of $10^4 M_{\odot}$. With their choice of initial conditions the positive feedback, the additional or faster formation of cores, outweighs the negative feedback, the disruption of cores. All these applications calculate the effect of a point source on the surrounding medium, thereby focussing much more on the global effect of the ionization. However, neither the detailed morphology of the gas nor the impact of the ionizing radiation on the turbulence has been investigated so far.

5.2 Initial Conditions

We set up a box of gas with sides 4 pc long at a temperature of $T_{cold} = 10\text{K}$ and a mean number density of $\bar{n} = 300\text{cm}^{-3}$, which resembles a slightly denser part of a molecular cloud. The gas mass in the box is $474 M_{\odot}$ which corresponds to 25 Jeans masses. To mimic initial turbulence we employ a supersonic turbulent velocity field (Mach 10) with a steep power-law $E(k) \propto k^{-2}$, where only the largest modes $k = 1..4$ are populated initially. This setup is allowed to freely decay under the influence of isothermal hydrodynamics simulated with the tree/SPH-code VINE (Wetzstein et al. 2008, Nelson et al. 2008). The individual particle time-steps in VINE are determined by using an accuracy parameter of $\tau_{acc} = 1.0$ and a Courant-Friedrichs-Lewy (CFL) tolerance parameter of $\tau_{CFL} = 0.3$. We also use an additional time-step criterion based on the maximum allowed change of the smoothing length with an accuracy parameter of $\tau_h = 0.15$.

After $\approx 1\text{Myr}$ a Kolmogorov-like power-law with $E(k) \propto k^{-\frac{5}{3}}$ is well established on all resolvable scales. The velocities now correspond to Mach 5. This initial setup with the turbulent

velocities is shown in Fig. 5.1 (top panel), the corresponding power-spectrum in Fig. 5.2 (top panel).

With these turbulent initial conditions we perform two simulations, one with and one without the inclusion of ionization. To account for the UV-radiation of a young massive star we use iVINE (G09), a new parallel implementation of ionizing radiation in the tree-SPH code VINE. Here we assume plane-parallel infall of UV-radiation onto one transparent side of the simulated area, which enables us to perform simulations at yet unmatched high resolution. From the surface the radiation is propagated by a ray-shooting algorithm. The size of the rays is determined by the smoothing-length of the SPH-particles, i.e. the width a particle occupies. Along these rays the radiation is calculated. This provides us with an ionization degree η for each SPH-particle, which is then used to assign a new temperature to each particle by linear interpolation.

$$T = T_{\text{hot}} \cdot \eta + T_{\text{cold}} \cdot (1 - \eta), \quad (5.1)$$

where $T_{\text{cold}} = 10\text{K}$ is the initial temperature of the cold, unionized gas and $T_{\text{hot}} = 10^4\text{K}$ is the average temperature of the ionized gas (see e.g. Shu, 1991b). The gas is assumed to be atomic hydrogen. Both gas components are close to thermal equilibrium since the heating and cooling timescales are much shorter than the dynamical timescales. We treat the gas with an isothermal equation of state ($\gamma = 1$) as for the density range in our simulations heating and cooling should balance each other to approximate isothermality (see e.g. Scalo et al., 1998). However, in reality the situation is more complicated. Recent simulations by Glover & Mac Low (2007) indicate an equation of state of the thermal equilibrium gas which is softer than isothermal ($\gamma = 0.7 - 0.8$). For a detailed prescription of the iVINE-code along with several analytical test cases see G09. In the simulations presented here the radiation was calculated on more than $(60)^2$ rays, with the additional inclusion of five levels of refinement, leading to a spatial resolution of $2 \times 10^{-3}\text{pc}$ in the radiation. The photon flux per unit time and area is set to $F_{Ly} = 5 \times 10^9 \text{photons cm}^{-2}\text{s}^{-1}$, allowing the radiation to penetrate the first 10% of the cloud immediately. This corresponds to setting up our simulation to be right at the border of the Strömgren-sphere (Strömgren, 1939), which can be immediately ionized by an O-star or association.

The radiation is impinging from the negative x-direction. Hydrodynamics is calculated with periodic boundaries in the y- and z-direction. The boundary is assumed to be reflecting in the negative x-direction to represent conservation of flux toward the star, whereas in the positive x-direction the gas is allowed to stream away freely. Gravitational forces are calculated without boundaries. This is valid as the free-fall time of the whole simulated area is $t_{\text{ff}} \approx 3\text{Myr}$, which is much larger than the simulation time. To ensure a correct integration of all quantities we use the individual time-stepping-scheme of VINE with the same parameters as for the freely decaying turbulence (see above). For the tree-based calculation of gravitational forces we use a multi-pole acceptance criterion (MAC, Springel et al. 2001) with a tree accuracy parameter of $\theta = 5 \times 10^{-4}$. The correct treatment of the ionization and the resulting acceleration of the particles is obtained by a modified CFL-condition as discussed in G09. The simulations are performed with 2×10^6 gas particles on a SGI Altix 3700 Bx2 supercomputer. The entire calculation took approximately 100 wall clock hours on 16 CPUs.

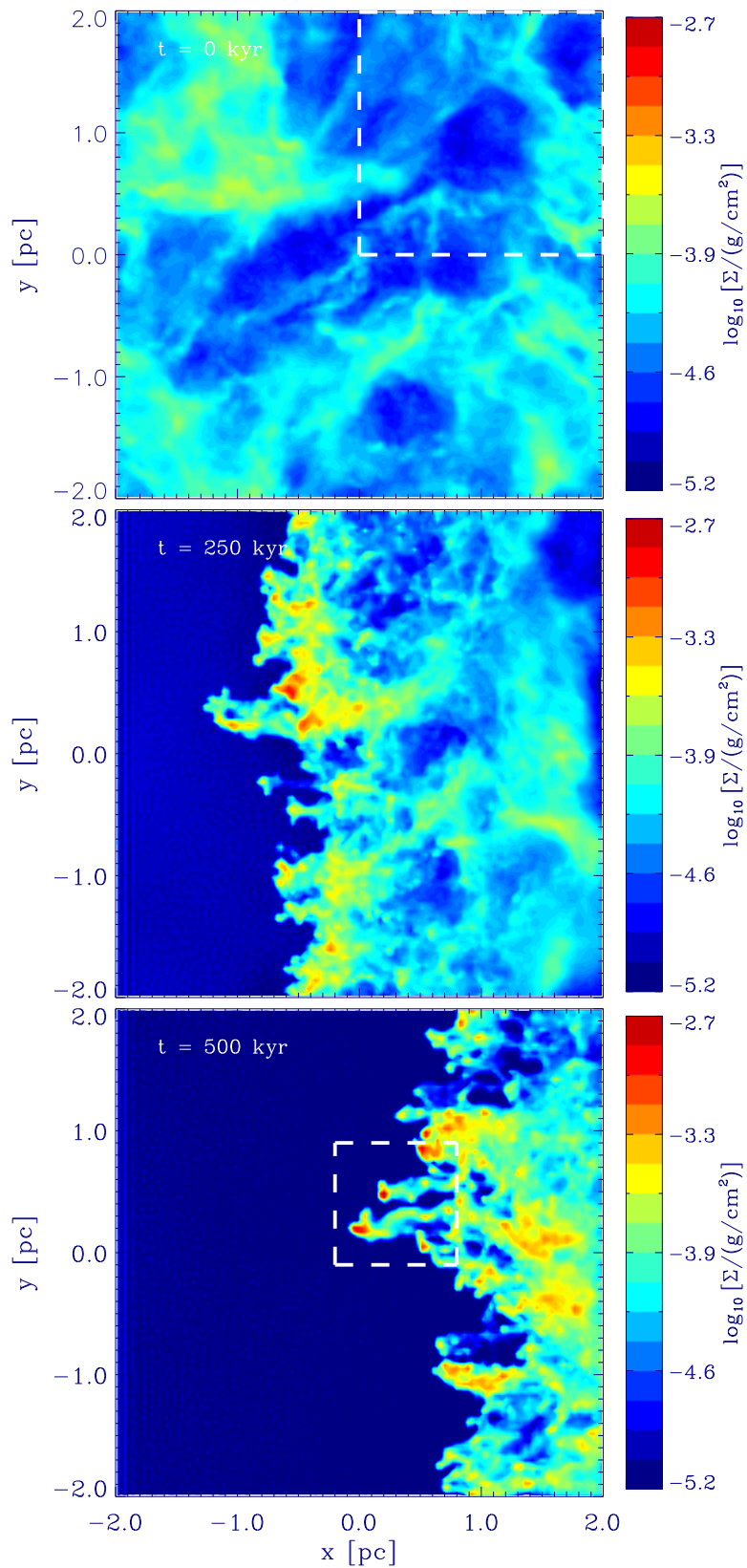


Figure 5.1: Evolution of the turbulent ISM under the influence of UV-radiation impinging from the left hand side. Color coded is the surface density projected along the z-direction. The time of the snapshot is increasing from top to bottom.

5.3 Results

5.3.1 Morphology and Formation of Cores

At the beginning of the simulation the R-type front immediately reaches into the first 10% of the box, with the radiation penetrating further into the low density parts of the cold gas. After a hydrodynamical crossing timescale of the hot gas ($t_{\text{hot}} \approx 30\text{kyr}$)² the ionized gas reacts to its increase in temperature and starts to exert pressure on the cold gas. The cold gas is compressed and pushed away from the source, leading to a systematic velocity in the x-direction. At the same time the radiation has penetrated and ionized the ISM along channels of low density gas. Now these low density regions expand and start compressing the denser, unionized regions especially tangential to the direction of radiation. Thus the preexisting density structures, which are seeded by the turbulent initial conditions get enhanced as shown in Fig. 5.1.

The combination of overall and tangential compression leads to elongated structures that keep sweeping up cold gas. After $\approx 250\text{kyr}$ (Fig. 5.1, middle panel) the dominant structures are already excavated by the combination of radiation and the pressure of the hot gas. From now on the evolution is mainly dominated by the hydrodynamic interactions between the hot and cold phase of the gas.

After $\approx 500\text{kyr}$ (Fig. 5.1, bottom panel) the morphology is remarkably reminiscent of the observed structures. The pillars in our simulations are indeed very complex structures with a cork-screw type, torqued morphology and show rotational motion around their main axis, as it is observed (Gahm et al., 2006). Up to now it has been suggested that these complex morphologies arise due to magnetic fields, which are not included in our simulations. It is very likely that the pillars in M16 are a snapshot of the formation scenario proposed here. At this stage the densest region (indicated by the center of the white box in Fig. 5.1, bottom panel) undergoes gravitational collapse, the simulation is slowed down considerably and we terminate it. Future simulations with the inclusion of e.g. sink particles to avoid the detailed calculation of the further gravitational collapse leading to low mass stars will allow us to trace the subsequent evolution of the whole region. We call the most prominent feature in the white box in Fig. 5.1 (bottom panel) 'pillar I' and the second largest 'pillar II', the collapsing compact core is at the tip of pillar II. Their respective masses are $M_{\text{pillarI}} = 12.3M_{\odot}$, $M_{\text{pillarII}} = 8.1M_{\odot}$ and $M_{\text{core}} = 0.7M_{\odot}$. The compact core is defined as all material with a number density above $n_{\text{crit}} = 10^7\text{cm}^{-3}$ in a region of $R_{\text{crit}} = 0.02\text{pc}$ around the peak density (see G09). Observations show that star formation is taking place close to the tips of the evolving structures (Snider et al., 2007). The same is true for our simulations. In the process of sweeping up the dense material lags behind, gaining less momentum and thus leading to very high density enhancements near the radiation front. In contrast, the simulation without UV-radiation does not show any signs of gravitational collapse.

Overall the scenario is very similar to the 'collect and collapse' model, as the denser regions would not collapse on their own on the timescale simulated and the sweeping up of material plays a vital role. We call it 'collect and collapse with turbulent seeds'.

²This timescale is calculated by taking the sound speed of the hot ionized gas $c_{\text{s,hot}} = 13.1\text{pc/Myr}$ and the average penetration length of the ionization of 0.4pc into account.

5.3.2 Turbulent Evolution

For the discussion of the evolution of the density weighted spectra from the run with ionization we perform a control run with the same initial conditions and accuracy parameters as the main simulation but without the inclusion of UV-radiation. In the comparison run no sign of star formation can be detected. This is reasonable, since the cloud is not set up to become gravitationally unstable as the total time of the simulation is much less than t_{ff} . The comparison is shown at $t = 0\text{kyr}$, $t = 250\text{kyr}$ and $t = 500\text{kyr}$ (Fig. 5.2). We analyze the turbulent spectrum in four cubic domains in the backward domain of the simulation, spanning 2pc in each direction (one is indicated in Fig.5.1, top panel, the other three are shifted in the negative y- and z-direction, respectively). Thus, it is guaranteed that there is always enough cold gas in the volume to achieve sensible results. To avoid a bias by either the ionized gas or the forming high density regions we take into account only gas with a number density $10^2\text{cm}^{-3} < n < 10^4\text{cm}^{-3}$. The particles are binned on a $(128)^3$ cubic grid by using a kernel-weighted binning routine (as e.g. in Kitsionas et al., 2008). Based on this grid we calculate the density weighted spectra by substituting \mathbf{v} with $(\rho/\bar{\rho})^{1/2}(\mathbf{v} - \mathbf{v}_{\text{RMS}})$ before the Fourier transformation. \mathbf{v}_{RMS} is the average velocity in each of the three components. The specific turbulent kinetic energy in the Fourier space is then given as

$$\epsilon_{\text{kin,turb}} = \frac{1}{2}(\mathbf{v}' \cdot \bar{\mathbf{v}}'), \quad (5.2)$$

where \mathbf{v}' and $\bar{\mathbf{v}}'$ are the Fourier transform of the substituted velocity and its complex conjugate, respectively. By mapping the $\epsilon_{\text{kin,turb}}$ cube to wave numbers \mathbf{k} , the specific energy in the compressional, curl-free modes can be calculated as

$$\epsilon_{\text{com}} = \epsilon_{\text{turb,kin}} \frac{(\mathbf{v}' \cdot \mathbf{k})(\bar{\mathbf{v}}' \cdot \mathbf{k})}{(\mathbf{k} \cdot \mathbf{k})(\mathbf{v}' \cdot \bar{\mathbf{v}}')}. \quad (5.3)$$

The specific energy in the solenoidal or incompressible, divergence-free modes is then given by $\epsilon_{\text{sol}} = \epsilon_{\text{kin,turb}} - \epsilon_{\text{com}}$. We construct the spectra by collecting the energy in the different wavenumber intervals (see Kitsionas et al., 2008, for details). The total spectra as well as the solenoidal and compressional parts are shown in Fig. 5.2.

The initial spectrum at $t = 0\text{kyr}$ (Fig.5.2, top panel) resembles quite well a power-law, even though the large-scale (low k) modes are lower, as the initial conditions are not produced by driven but by freely decaying turbulence. The slope is similar to a Kolmogorov-law. Approximately 25% of the total turbulent energy is contained in the compressional modes.

At $t = 250\text{kyr}$ (Fig.5.2, middle panel) there is already a distinct difference between the two spectra. The control run keeps the power-law shape and dissipates energy. In the ionization case the power is strongly increased on all scales. The increase is pronounced for $k > 10$, corresponding to scales $< 0.2\text{pc}$. An interesting feature is the rise in the compressional modes, where now 39% of the total turbulent energy is contained, whereas in the comparison run this ratio stays at 25%. This clearly shows that the energy of the radiation is transferred into compression of the cold gas via the hot gas. The increase is in the turbulent energy itself and not correlated to the overall bulk motion in the x-direction, since the mean velocity is subtracted separately in each direction before the Fourier transform.

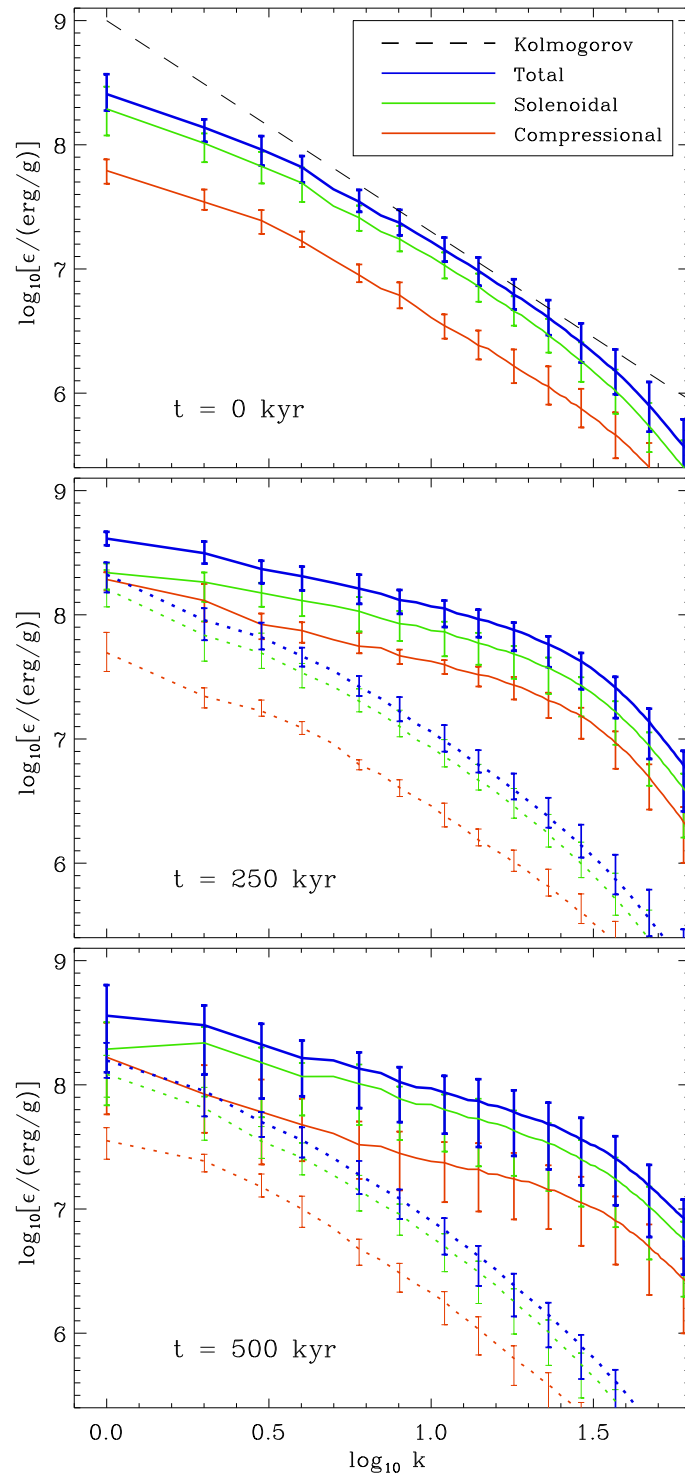


Figure 5.2: Evolution of the density weighted power spectra, plotted is the logarithm of the wavenumber versus the logarithm of the specific kinetic energy. Solid lines denote the run with ionization, dotted lines the control run without ionization. Plotted is the mean value of the spectra in the four different backward cubes, the error bars show the minimum and maximum values. Blue: total specific kinetic energy, green: solenoidal modes, red: compressional modes, dashed: Kolmogorov power-law.

After $t = 500$ kyr (Fig.5.2, bottom panel) these differences are even more pronounced. The kinetic energy in the cold gas is now a factor of four higher than in the run without ionization. Approximately 33% of the total turbulent energy is now contained in the compressional modes. This suggests that after an initial phase of high compression the system starts to relax.

Including the mass in the respective region and density range the total turbulent energy can be calculated. The initial turbulent energy is $E_{\text{turb}} = 2.1 \times 10^{45}$ erg, the final turbulent energy (at $t = 500$ kyr) is $E_{\text{ion}} = 4.3 \times 10^{45}$ erg and $E_{\text{nonion}} = 1.1 \times 10^{45}$ erg in the ionized and unionized case, respectively. Thus, the input of turbulent energy per unit volume and unit time averaged over the simulation time when comparing the run with ionization to the case of freely decaying turbulence is $\dot{e}_{\text{turb}} = 2.1 \times 10^{-25} \text{erg s}^{-1} \text{cm}^{-3}$. By using the simplified assumption that the UV-radiation is absorbed isotropically in the entire simulation volume the amount of energy contained in the ionizing radiation for the chosen flux F_{Ly} is $\dot{e}_{\text{Ly}} = 3.5 \times 10^{-20} \text{erg s}^{-1} \text{cm}^{-3}$. Compared to the estimates of Matzner (2002) and Mac Low & Klessen (2004) our radiative energy is several orders of magnitude higher, since we look at the direct surrounding of an O-star instead of averaging over an entire galaxy. Nevertheless, the conversion efficiency of ionization into turbulent motion of the cold gas is in our case $\sigma = \dot{e}_{\text{turb}}/\dot{e}_{\text{Ly}} \approx 2 \times 10^{-5}$, which is an order of magnitude higher than their estimate of $\sigma \approx 2 \times 10^{-6}$ for the Milky Way. Our highly resolved simulations show that ionizing radiation from an O-star or association provides a much more efficient mechanism to drive and sustain turbulence in the parental molecular cloud than was previously estimated. However, this is still the energy input into the local environment in contrast to the average input rate on galactic scales derived by Mac Low & Klessen (2004). On the larger scales it does not appear to contribute as significantly as e.g. supernova explosions.

5.4 Discussion

We have shown in this letter that the observed pillar-like structures around O-stars as well as the gravitational collapse at the tip of the pillars can result from the impact of the ionizing radiation of massive O-stars on a turbulent molecular cloud. In addition, the turbulent energy in the cold gas is increased by a factor of four, especially in the compressional modes. Both effects are due to the same mechanism: the ionization can heat the gas along channels of low density, thereby compressing gas at higher density into filaments. Close to the source of ionization this leads to the excavation of pillar-like structures with triggered gravitational collapse at their tips. Further away from the source front, the structures have not yet fully developed, nevertheless the effect of compression is clearly visible in the turbulent energy spectra.

Even though we find striking similarities between our simulations and observations, one has to bear in mind that this is a simplified approach which does not involve full radiative transfer. Ionized gas which gets shaded is assumed to cool immediately without affecting the adjacent structures. In addition, the shaded gas does not get ionized and heated by the recombination radiation of the ionized gas surrounding it. This might influence the precise shape of the structure behind the tip. Moreover, the thin surface layers around each pillar where cold and hot gas are mixing cannot be resolved, although they might be crucial for the precise understanding of the temperature and the chemical composition of these structures. Nevertheless, our simulations

indicate that these detailed effects are of minor importance to explain the global picture, i.e. the overall structure and mass assembly of the pillars observed. Stellar winds might have an additional impact. Although O-stars have very powerful winds which can reach velocities of up to 1000km/s, our models suggest that ionizing radiation alone can reproduce most observed features.

The straightforward combination of hydrodynamics and ionizing radiation together with a standard turbulent model and typical parameters for molecular clouds leads to morphologies consistent with observed objects like pillars and collapsing cores. The similarities suggest that ionizing radiation plays a major role not only in shaping the parental cloud, but also in triggering secondary star formation. Furthermore, the overall turbulent kinetic energy in the cold gas is increased significantly.

Acknowledgments

We thank the referee for the valuable comments which helped to improve the manuscript. This research was funded by the DFG cluster of excellence 'Origin and Structure of the Universe'. All simulations were performed on a SGI Altix 3700 Bx2 supercomputer that was partly funded by the DFG cluster of excellence 'Origin and Structure of the Universe'.

Chapter 6

Detailed Numerical Simulations on the Formation of Pillars around HII regions

¹M. Gritschneider, A. Burkert, T. Naab, S. Walch

We perform a set of high resolution simulations on the impact of UV-radiation on the turbulent interstellar medium (ISM). This parameter study includes different levels and driving scales of the turbulence, different ionizing flux as well as different temperatures and densities of the cold gas. We find a clear correlation between the initial state of the turbulent cold cloud and the final morphology and physical properties of the structures adjacent to the HII region. From the simulations we are able to derive a criterion for the formation of pillar-like structures and thus the formation of cores and stars. Gravitational collapse occurs regularly on the tips of the structures. We also derive column densities and velocity profiles of our simulations and find these to be in very good agreement with the observations of trunks and cores. The line-of-sight velocity profiles of the simulations resemble the observed rotational patterns in some projections, although the true velocity fields are turbulent.

stars: formation, ISM: structure, turbulence, ultraviolet: ISM, methods: numerical, HII regions

6.1 Introduction

As soon as a massive O type star ignites, it starts to shape its parental molecular cloud (MC) by its UV-radiation and stellar winds. Very often peculiar structures are found in the vicinity of these ionizing sources, e.g. the 'pillars of creation' in the Eagle Nebula (M16). The observations of this region by Hester et al. (1996) are arguably the most famous picture ever taken with the Hubble Space Telescope. There is also wide-spread evidence for star formation at the tips of the pillars (e.g. Sugitani et al., 2002; Thompson et al., 2002; McCaughrean & Andersen, 2002). For a very recent review of M16 see Oliveira (2008).

Since the launch of the Spitzer Space Telescope a wealth of highly resolved observations of the peculiar pillar or trunk-like structures observed around the hot, ionized HII-regions of massive stars and the star formation in this trunks has become available, e.g. in the Orion clouds

¹to be submitted

(Stanke et al., 2002; Lee & Chen, 2007; Bowler et al., 2009), the Carina nebula (Smith et al., 2000), the Elephant Trunk Nebula (Reach et al., 2004), the Trifid Nebula (Lefloch et al., 2002), M16 (Andersen et al., 2004), M17 (Jiang et al., 2002), 30 Dor (Walborn et al., 2002) and the SMC (Gouliermis et al., 2007b). In addition, several recent observations of bright rimmed clouds (Urquhart et al., 2009; Chauhan et al., 2009) have been carried out. An interesting aspect is the surprisingly spherical shape of many observed nebulae, especially in RCW 120, 'the perfect bubble' (Deharveng et al., 2009). Other other regions, like e.g. RCW 79 (Zavagno et al., 2006), RCW 82 (Pomarès et al., 2009) and RCW 108 (Comerón & Schneider, 2007) share this morphology.

On the theoretical side, star and structure formation in the vicinity of HII-regions is mainly studied with respect to two different aspects. On the one hand there is the 'radiation driven implosion' (RDI) model (see e.g. Klein et al., 1980; Bertoldi, 1989). Here, a pre-existent, but gravitationally stable density enhancement is driven into collapse by the increase in pressure of the surrounding gas. On the other hand there is the 'collect and collapse' (C&C) model proposed by Elmegreen & Lada (1977). A shock front, resulting from the expansion of the hot, ionized gas is driven into the cold surrounding gas and sweeps up material in a dense shell, until it becomes gravitationally unstable. This mainly applies to scales larger than the ones studied here. The model proposed in Gritschneider et al. (2009b, hereafter G09b) bridges the gap between the two. The impact of ionizing radiation on a preexisting turbulent medium is studied. This does not correspond directly to the RDI, since a turbulent medium does not consist of isolated initial structures, which are then driven into collapse. On the other hand, the collapse does not occur by gravitational instabilities inside the shell as in the C&C model. In our model, clumpy substructures are already present. These get compressed to filamentary structures, which now contain enough material collapse on their own. Their gravitational collapse happens after the passage of the main front. Since it is the combination of both processes leading to gravitational collapse we call it 'radiative round-up'.

A main motivation of developing software able to treat ionizing radiation have been investigations of the reionization of the early universe (see e.g. Iliiev et al., 2006; Pawlik & Schaye, 2008; Altay et al., 2008, and references therein). However, several methods treating ionization in the context of contemporal star formation have been developed (e.g. Elmegreen et al., 1995; Kessel-Deynet & Burkert, 2000; Dale et al., 2005; Mellema et al., 2006; Krumholz et al., 2007; Bisbas et al., 2009; Peters et al., 2009), for grid-based as well as for smoothed particle hydrodynamics (SPH) codes.

The results of the first simulations are already encouraging. Kessel-Deynet & Burkert (2003) presented three-dimensional RDI simulations with an SPH code and were able to show that an otherwise gravitationally marginally stable sphere can be driven into collapse by ionizing radiation. Mellema et al. (2006) reproduced the observed morphologies of HII regions by ionizing a turbulent medium with a grid code without the inclusion of gravity. Dale et al. (2007a) compared the gravitational collapse of a MC with and without ionization in an SPH code. They found slightly enhanced star formation in the simulation with ionization. The inclusion of ionization in a grid code in combination with a magnetic field was discussed by Krumholz et al. (2007). A homogenous magnetic field leads to a non-spheric HII-region, as the gas is held back by the magnetic field lines and an oval shaped bubble evolves. In Gritschneider et al. (2009a, hereafter

G09a) we showed that marginally stable density enhancements get triggered into forming stars in cases with high as well as with low ionizing flux. Miao et al. (2009) further analyzed this RDI-scenario with a SPH-code including a radiative transfer scheme. They show that there is an evolutionary sequence, depending on the initial size of the MC, as suggested by Lefloch & Lazareff (1994). In G09b we investigated a subsection of a MC with high resolution and found that the ionization of the turbulent cold medium leads to pillar-like morphologies as well as to triggered star formation. Furthermore, the turbulence in the cold gas is strongly influenced by the ionization. This study will present a more detailed investigation of the evolution of turbulent clouds affected by stellar ionization using iVINE (G09a), an implementation of ionization into SPH.

The structure of this paper is as follows. In §6.2 we briefly review the concept of ionizing radiation, followed by a short summary of the iVINE-code. After that we present the set of initial conditions for the parameter study. In §6.3 the outcome of the different simulations is discussed in detail. A close comparison to the observations is done in §6.4 and we draw the conclusions in §6.5.

6.2 Basic Approach and Initial Conditions

6.2.1 Ionizing Radiation

As soon as an O star is born it ionizes its surroundings by UV-radiation. This leads to an ionized, hot HII-region ($T_{\text{ion}} \approx 10^4$ K). In the beginning the 'R-type' ionization front travels with a speed v_R which is greater than the sound speed of the hot gas a_{ion} . This phase ends as soon as the ionization is balanced by recombinations in the HII-region. The ionized volume V_S , the so called Strömgren sphere (Strömgren, 1939), is then given by

$$V_S = \frac{J_{\text{Ly}}}{\alpha_B (\rho_0/m_p)^2}. \quad (6.1)$$

Here, J_{Ly} is the flux of ionizing photons of the source, which is assumed to be constant and monochromatic, α_B is the recombination coefficient, ρ_0 is the density of the preexisting, homogeneous gas and m_p is the proton mass. At a larger distance from the star the radiation can be assumed to impinge plane-parallel onto a surface and thus Eq. 6.1 simplifies to

$$x_S = \frac{F_{\text{Ly}}}{\alpha_B (\rho_0/m_p)^2}, \quad (6.2)$$

where x_S is the thickness of the ionized region and F_{Ly} is the in-falling ionizing flux per unit time and unit area.

After a hydrodynamical timescale the hot gas reacts to its increased temperature and pressure. The pressure of an ideal one-atomic gas is given by

$$P = \rho \frac{k_B T}{\mu m_p} = \rho c_s^2, \quad (6.3)$$

where ρ is the density, k_B the Boltzmann constant, μ the mean molecular weight and c_s^2 the isothermal sound-speed. Now the evolution is characterized by an isothermal shock followed by a weaker, 'D-type' ionization front. The front velocity is now $v_D < a_{\text{ion}}$. For a full analysis see e.g. Shu (1991b). As the hot gas expands its density is reduced. At the same time the cold, surrounding gas is compressed. Under the assumption that the homogeneous ionized region consumes all UV-photons of the source it follows from Eq. 6.2 that the density of the hot gas for a constant flux and a constant temperature T_{hot} at any given time is

$$\rho_{\text{hot}}(t) = \sqrt{\frac{m_p^2 F_{\text{Ly}}}{\alpha_{\text{B}} x(t)}}. \quad (6.4)$$

To calculate the front position $x(t)$ we follow the approach by Dopita & Sutherland (2003). Under the assumption of a thin shock with the speed v_s the ram pressure in the hot, ionized gas has to be equal to the ram pressure in the cold gas

$$P_{\text{ion}} = P_{\text{cold}}, \quad (6.5)$$

where

$$P_{\text{cold}} = \rho_0 v_s^2 = \rho_0 \left(\frac{dx}{dt} \right)^2 \quad (6.6)$$

The pressure at the ionized side of the shock is mainly given by the thermal pressure of the hot gas

$$P_{\text{ion}} = f P_{\text{hot}} = f \rho_{\text{hot}} c_{s,\text{hot}}^2, \quad (6.7)$$

where we have already introduced a constant fitting factor f to account for the approximations made, especially the one leading to Eq. 6.4. Combining both equations and using Eq. 6.4 and 6.2 yields

$$x^{\frac{1}{4}} \frac{dx}{dt} = f c_{s,\text{hot}} x_s^{\frac{1}{4}}. \quad (6.8)$$

With the initial condition $x(t_0) = x_s$ we can integrate and obtain

$$x(t) = x_s \left(1 + \sqrt{f} \frac{5}{4} \frac{c_{s,\text{hot}}}{x_s} (t - t_0) \right)^{\frac{4}{5}}. \quad (6.9)$$

Using Eq. 6.4 it follows that

$$\rho_{\text{hot}}(t) = \rho_0 \left(1 + \sqrt{f} \frac{5}{4} \frac{c_{s,\text{hot}}}{x_s} (t - t_0) \right)^{-\frac{4}{10}} \quad (6.10)$$

for a plane-parallel infall of a constant flux onto a homogeneous medium.

6.2.2 Numerical Method and First Tests

In order to investigate the effect of different initial conditions and levels of UV-radiation on the formation of pillars we conduct a parameter study. All simulations were performed with the newly developed code iVINE (G09a), an implementation of ionizing radiation in the tree-SPH code VINE (Wetzstein et al., 2008; Nelson et al., 2008). Here, the ionizing radiation is assumed to impinge plane-parallel onto the simulated volume from the negative x-direction. From the surface of infall the radiation is propagated along the x-direction by a ray-shooting algorithm. Along these rays the ionization degree η_i is calculated for each particle i . According to the ionization degree, the pressure P_i of the particle is calculated by a linear extrapolation of the temperature T_{hot} of the hot, ionized and the temperature T_{cold} of the cold, un-ionized gas. Here, we assume both gas components to be isothermal, since for the density range in our simulations heating and cooling should balance each other to approximate isothermality (see e.g. Scalo et al., 1998). Following Eq. 6.3 the new pressure in our simulation is given as

$$P_i = \left(\frac{T_{\text{ion}}\eta_i}{\mu_{\text{ion}}} + \frac{T_{\text{non}}(1-\eta_i)}{\mu_{\text{non}}} \right) \frac{k_B\rho_i}{m_P}, \quad (6.11)$$

where ρ_i is the SPH-density of the particle i and $\mu_{\text{ion}} = 0.5$ and $\mu_{\text{non}} = 1.0$ are the mean molecular weights of the ionized and the un-ionized gas in the case of pure hydrogen, respectively.

As a first test we verify Eq. 6.9 and fit a value for f by ionizing a slab of atomic hydrogen with a constant homogeneous density of $\rho_{\text{cold}} = 300 m_P \text{cm}^{-3}$ and a temperature of $T_{\text{cold}} = 10 \text{K}$. We perform three different runs, corresponding to a low flux (LF, $F_{\text{Ly}} = 1.66 \times 10^9 \gamma \text{cm}^{-2} \text{s}^{-1}$), an intermediate flux (IF, $F_{\text{Ly}} = 5 \times 10^9 \gamma \text{cm}^{-2} \text{s}^{-1}$) and a high flux (HF, $F_{\text{Ly}} = 1.5 \times 10^{10} \gamma \text{cm}^{-2} \text{s}^{-1}$). This corresponds to the ionization penetrating immediately into the first 0.55%, 1.67% and 5% of the region, respectively (see Eq. 6.2). At the same time this is equal to placing the simulation volume further away or closer to the source, e.g. the O-star. The simulations are conducted with the same accuracy and setup as in the parameter study given below (see §6.2.3). Fig. 6.1 shows the resulting evolution of the front. As one can clearly see the approximations leading to Eq. 6.2 ($f = 1$, the dotted lines in Fig. 6.1) do not produce satisfactory results. Instead, assuming

$$P_{\text{ion}} = \frac{5}{4} P_{\text{hot}} \quad (6.12)$$

(i.e. $f = \frac{5}{4}$, the dashed lines in Fig.6.1) perfectly matches the simulations during the entire simulated time of $t_{\text{sim}} = 500 \text{kyr}$. Thus, we keep this assumption for this work.

6.2.3 Initial Conditions

To produce different turbulent initial conditions we use the same approach as in G09b. We set up a supersonic velocity field (Mach 10) with a steep power-law $E(k) \propto k^{-2}$. Before switching on the ionizing source each setup decays freely under the influence of isothermal hydrodynamics and periodic boundary conditions until the desired initial Mach number is reached (after $t \approx 0.8 - 1.0 \text{Myr}$, depending on the specific simulation). The individual particle time-steps in VINE

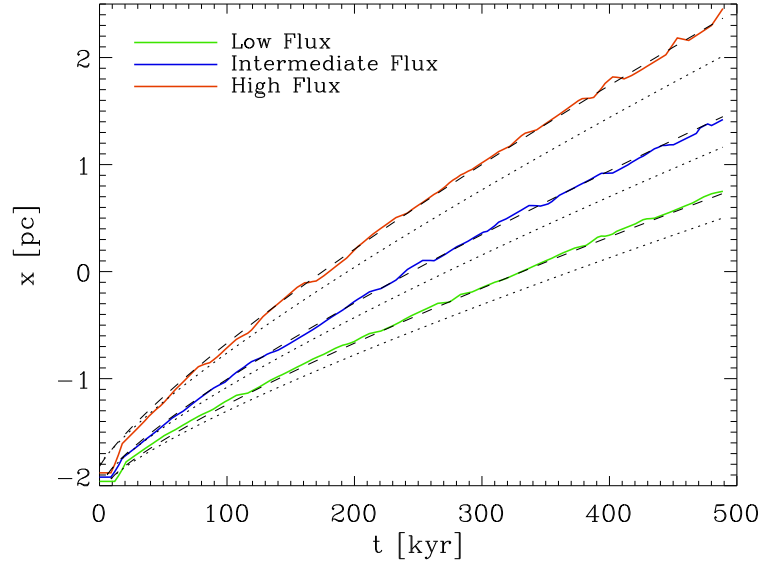


Figure 6.1: Front position versus time for the three test simulations with a different flux impinging on a homogeneous medium. Green, blue and red line: simulations with a low, intermediate and high flux, respectively. Black lines: solution according to Eq. 6.9, dotted $f = 1$, dashed $f = \frac{5}{4}$.

are determined as in G09b by using an accuracy parameter of $\tau_{\text{acc}} = 1.0$ and a Courant-Friedrichs-Lewy (CFL) tolerance parameter of $\tau_{\text{CFL}} = 0.3$. An additional time-step criterion based on the maximum allowed change of the smoothing length with an accuracy parameter of $\tau_h = 0.15$ is also employed.

The initial properties of the different simulations are listed in Table 6.1. A short description of the main differences to the 'fiducial' simulation presented in G09b are given here:

- **M5IF4pk1** Standard case: Mach5, an intermediate flux, the box length is 4 pc and before the free decay only the largest turbulent modes $k = 1.4$ are populated. The temperature of the cold gas is $T_{\text{non}} = 10\text{K}$, the mean density is $\bar{\rho} = 300 m_{\text{P}} \text{cm}^{-3}$ and the simulation is performed with 2×10^6 gas particles.
- **M5LF4pk1** Low Resolution: the number of particle is eight times lower than in the standard case, thus the spatial resolution is two times lower.
- **M5IF-open** Open Boundary: the same as M5IF4pk1, but the gas is allowed to stream away freely in the negative x-direction.
- **M5IFwarm** Warm Medium: the temperature of the un-ionized gas is $T_{\text{non}} = 100\text{K}$, the turbulence is still at Mach 5, now with respect to the higher sound-speed at 100K.

Simulation	$M[M_{\odot}]$	$\bar{\rho}[m_{\text{P}}\text{cm}^{-3}]$	$l_{\text{box}}[\text{pc}]$	$F_{\text{Ly}}[\gamma\text{cm}^{-2}\text{s}^{-1}]$	Mach	k	$T_{\text{ion}}[\text{K}]$
M5IF4pk1	474	300	4	5×10^9	5	1-4	10
M5IF-1r	474	300	4	5×10^9	5	1-4	10
M5IF-open	474	300	4	5×10^9	5	1-4	10
M5IFwarm	474	300	4	5×10^9	5	1-4	100
M5LF4pk1	474	300	4	1.7×10^9	5	1-4	10
M5HF4pk1	474	300	4	1.5×10^{10}	5	1-4	10
M5LF-n100	158	100	4	1.7×10^9	5	1-4	10
M5IF4pk4	474	300	4	5×10^9	5	4-8	10
M2IF4pk1	474	300	4	5×10^9	2	1-4	10
M7IF4pk1	474	300	4	5×10^9	7	1-4	10
M5IF2pk1	119	300	2 ²	5×10^9	5	1-4	10
M5IF8pk1	3795	300	8	5×10^9	5	1-4	10

Table 6.1: Listing of the different initial conditions. Given are initial mass, average density and size of the simulation. In addition, the impinging flux, turbulent Mach number, the largest driving mode of the turbulence and the temperature are listed. M5IF4pk1 is the standard case as presented in G09b.

- **M5LF4pk1** Low Flux: the impinging flux is lower by one third compared to the standard case.
- **M5HF4pk1** High Flux: the initial flux is a factor of three higher compared to the standard case.
- **M5LF-n100** Low Density: the initial average density is a factor of three lower, the impinging flux is lowered by a factor of three.
- **M5IF4pk4** Low k: only the smaller turbulent modes $k = 4..8$ are populated before the free decay.
- **M2IF4pk1** Low Turbulence: the setup decays until Mach 2 before the ionization is switched on.
- **M7IF4pk1** High Turbulence: the setup decays until Mach 7 before the ionization is switched on.
- **M5IF2pk1** 2pc: the y- and z-boxlength is 2pc, the x-boxlength is 4pc. In order to obtain a constant factor between the mass resolution of all simulations the particle number is increased to 4×10^6 .
- **M5IF8pk1** 8pc: the box length is 8pc in each direction, the particle number is 2×10^6 .

To ensure a correct integration of all quantities we use the individual time-stepping-scheme of VINE with the same parameters as for the freely decaying turbulence (see above). In most

simulations hydrodynamics is calculated with periodic boundaries in the y- and z-direction. The boundary is reflecting in the negative x-direction to represent conservation of flux towards the star, whereas in the positive x-direction the gas is allowed to stream away freely. To test this assumption we perform one simulation with open boundaries in both x-directions. Gravitational forces are calculated without boundaries. This is valid as the free-fall time of the whole simulated area is $t_{\text{ff}} \approx 3 \text{ Myr}$, which is much larger than the simulation time of $t_{\text{final}} = 0.5 \text{ Myr}$. For the tree-based calculation of gravitational forces we use a multi-pole acceptance criterion (MAC, Springel et al. 2001) with a tree accuracy parameter of $\theta = 5 \times 10^{-4}$. The correct treatment of the ionization and the resulting acceleration of the particles is obtained by the modified CFL-condition discussed in G09a. The recombination of the hot gas is included with $\alpha_{\text{B}} = 2.59 \times 10^{-13} \text{ cm}^3 \text{ s}^{-1}$ and the cross-section for the ionizing photons is set to $\sigma = 3.52 \times 10^{-18} \text{ cm}^2$. The simulations are performed on a SGI Altix 3700 Bx2 supercomputer, the calculation of each setup took approximately 100 wall clock hours on 16 CPUs.

6.3 Results of the Parameter Study

6.3.1 General Properties

In all of the simulations forming structures the same effect as described in G09b takes place. The ionization penetrates further in the low density region of the turbulent setup. As the ionized gas reacts to its increase in pressure it starts to compress the adjacent, un-ionized, higher density regions. Typically at $t_{\text{final}} = 500 \text{ kyr}$ a clear morphology has evolved. Fig. 6.2 shows the surface density projected along the z-axis at this stage.

To enable a more quantitative discussion we investigate the most prominent structure in each simulation in more detail. To define the tip we take the particle closest to the source of radiation³ above a threshold density of $\rho_{\text{resh}} = 10^4 m_{\text{P}} \text{ cm}^{-3}$. We then take its surrounding, the region spanning 1 pc in the x-direction and 0.3 pc in the negative and positive y- and z- direction. The cold, un-ionized gas in this region is defined as the 'pillar'. This definition allows us to extract the important quantities by the same algorithm for all simulations to enable a direct comparison. The values for the defined pillar at $t_{\text{final}} = 500 \text{ kyr}$ are given in Table 6.2. We estimate the diameter of a pillar via

$$d_{\text{pillar}} = 2 \sqrt{\frac{M}{\rho x \pi}} \quad (6.13)$$

with $x = 1 \text{ pc}$ as the length of the pillar. In addition, the mean density⁴ of the hot gas is listed. It is notable that all simulations with the same impinging flux share a similar density of the pillar as well as of the hot gas. In the case of a homogenous medium this could be expected from Eq.

³In M5LF-n100, M7IF4pk1 and M5IF2pk1 the second tip was taken to produce comparable results.

⁴Denote that we always give the real density ρ of the hot gas, not the number density n to avoid the factor of $\mu = 0.5$ when comparing the low density, un-ionized gas to the ionized gas.

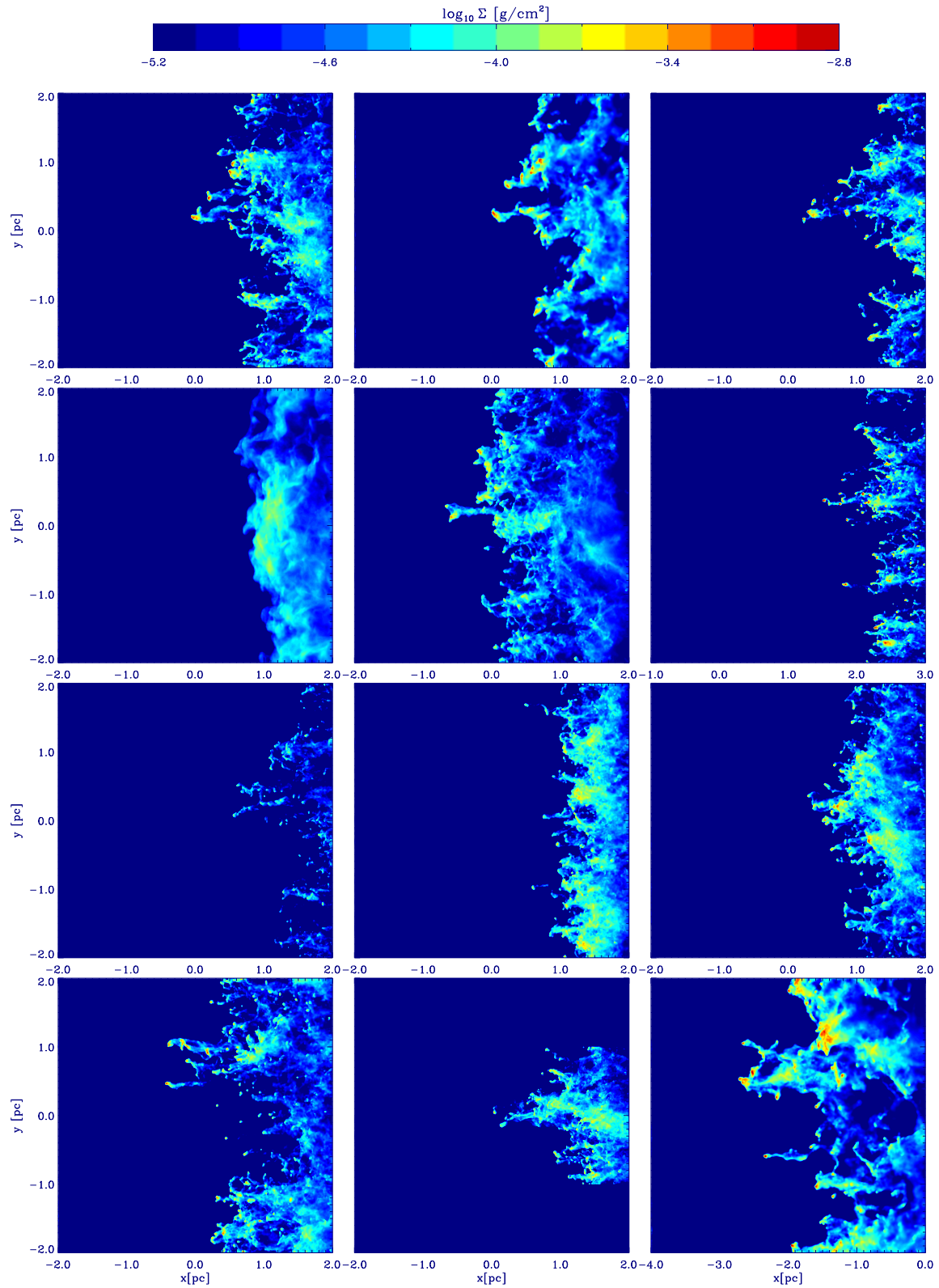


Figure 6.2: Surface density of all simulations of the comparison study, ordered from left to right and top to bottom as in Table 6.2, at the final stage $t_{\text{final}} = 500 \text{ kyr}$. Denote that in panel 6 and 12 the x-axis is shifted.

Simulation	$M[M_{\odot}]$	$\bar{\rho}_p[10^4 m_p \text{cm}^{-3}]$	$\bar{\Sigma}[10^{-3} \text{gcm}^{-2}]$	$\log_{10}[N(\text{H}_2)/\text{cm}^{-2}]$	$\sigma[\text{km s}^{-1}]$
M5IF4pk1	12.6	4.56	1.52	20.5	1.1 ± 0.7
M5IF-lr	14.26	5.66	1.69	20.5	0.88 ± 0.53
M5IF-open	11.0	5.06	1.44	20.5	1.2 ± 0.7
M5IFwarm	10.2	0.37	0.23	19.7	2.0 ± 0.8
M5LF4pk1	12.4	3.75	1.38	20.5	0.90 ± 0.5
M5HF4pk1	10.9	7.23	2.72	20.8	2.3 ± 1.3
M5LF-n100	5.79	2.80	0.99	20.3	1.99 ± 0.9
M5IF4pk4	2.78	3.44	1.16	20.4	1.2 ± 0.7
M2IF4pk1	12.6	3.62	1.32	20.4	1.3 ± 0.6
M7IF4pk1	14.0	5.36	1.71	20.6	1.1 ± 0.5
M5IF2pk1	3.39	2.76	1.00	20.3	1.6 ± 0.8
M5IF8pk1	51.1	4.76	1.94	20.6	1.0 ± 0.5
Simulation	$\bar{v}_x[\text{km s}^{-1}]$	$d[\text{pc}]$	$\bar{\rho}_{\text{ion}}[m_p \text{cm}^{-3}]$	ΔP	
M5IF4pk1	4.8 ± 0.9	0.12	43.4	1.90	
M5IF-lr	4.8 ± 0.5	0.11	42.5	1.50	
M5IF-open	5.4 ± 1.1	0.10	28.6	1.13	
M5IFwarm	3.3 ± 1.7	-	43.6	2.36	
M5LF4pk1	3.3 ± 0.7	0.13	26.5	1.41	
M5HF4pk1	8.2 ± 2.2	0.09	73.5	2.02	
M5LF-n100	6.1 ± 1.9	0.10	19.0	1.36	
M5IF4pk4	6.2 ± 0.9	0.06	42.2	2.45	
M2IF4pk1	3.9 ± 0.9	0.13	39.8	2.20	
M7IF4pk1	4.0 ± 0.9	0.11	39.2	1.46	
M5IF2pk1	3.4 ± 1.5	0.08	38.2	2.77	
M5IF8pk1	2.9 ± 0.7	0.24	42.5	1.78	

Table 6.2: Results of the parameter study. Listed are the mass, mean density, absolute turbulent velocity, velocity dispersion and the x-velocity away from the source of the most prominent structure. Then the mean diameter (see Eq. 6.13) of the pillar and the mean density of the hot gas are given. Finally, the pressure difference ΔP (see Eq. 6.14) is listed.

6.10. We define the pressure difference at $t_{\text{final}} = 500 \text{ kyr}$ as:

$$\Delta P_{\text{final}} = \frac{P_{\text{ion,final}}}{P_{\text{pillar,final}}} = \frac{2T_{\text{ion}} \rho_{\text{ion,final}}}{T_{\text{nion}} \rho_{\text{pillar,final}}} \quad (6.14)$$

Because ΔP_{final} is very close to unity in all simulations we derive as a first result that the pillars are in thermal equilibrium with the hot surrounding gas.⁵

6.3.2 Resolution and Boundary Conditions

The first two simulations do not address different physical properties but rather numerical details. M5IF-lr was performed with exactly the same setup as M5IF4pk1, but with eight times less particles. This leads to a lower spatial resolution by a factor of two. Nevertheless, the morphology is comparable to the higher resolution case (Fig 6.2, panel 2). The only noticeable difference is that the second largest structure in this case has already merged with the third structure. Furthermore, the tiny smaller structures are less frequent. The physical properties (see Table 6.2) are similar as well. The structures in the low resolution case tend to be a bit more massive, which can be expected with lower resolution. Altogether, the global structure and properties are comparable and thus we conclude that M5IF4pk1 is reasonably converged.

In the other test case we investigate the boundary condition in the negative x-direction. In M5IF-open this boundary is not reflecting. Instead the gas is allowed to stream away freely. This leads of course to a lower density in the ionized region. As a consequence the simulation (Fig. 6.2, panel 3) looks like the simulation with a higher flux (panel 6, see §6.3.4), since the radiation is able to penetrate further. Nevertheless, the formation of pillars still takes place and is not strongly affected. Even density and mass assembly of the prominent structure are alike. Therefore, the choice of the boundary condition is not influencing the overall scenario in a significant way. As it is more realistic to assume that there is already hot gas in the region between the source and the turbulent region we keep the reflecting boundary condition in all other simulation. These reflection can be seen as flux conservation at the left border of the simulation: as much gas streams from the area towards the source into the region as is streaming outwards.

6.3.3 Temperature and Pressure

The most striking difference can be seen between M5IF4pk1 (Fig. 6.2, panel 1) and M5IFwarm (panel 4). Both initial conditions are self-similar, both were set up with the same initial random seed for the turbulence and they are relaxed until their velocities resemble Mach 5 at their respective temperature. Consequently, at the time the ionization is switched on, their density distribution is the same. Since the impinging flux is identical, the radiation ionizes the same regions in both cases. Nevertheless, in M5IFwarm no evolution of any filamentary structure is visible. This leads to the conclusion that the pressure balance between the hot, ionized and the cold, un-ionized gas plays a crucial role in the formation of structures.

⁵In fact, the value is always slightly above one, but this can be e.g. attributed to the complete negligence of the turbulent motion in the cold gas in Eq. 6.14.

Taking Eq. 6.3 and the straightforward assumption that only regions with a lower pressure than the pressure of the hot gas can be compressed gives

$$P_{\text{nion,initial}} \leq P_{\text{ion,initial}} \quad (6.15)$$

and thus

$$\rho_{\text{nion}} \leq \rho_{\text{ion}} \frac{2T_{\text{ion}}}{T_{\text{nion}}}. \quad (6.16)$$

If we assume $\rho_{\text{ion}} = 100 m_{\text{P}} \text{cm}^{-3}$ in the beginning, as the ionization mainly penetrates the lower density regions, this equation yields $\rho_{\text{nion,10K}} \leq 3.6 \times 10^5 m_{\text{P}} \text{cm}^{-3}$ and $\rho_{\text{nion,100K}} \leq 3.6 \times 10^4 m_{\text{P}} \text{cm}^{-3}$. The maximum density $\rho_{\text{max}} = 8.8 \times 10^4 m_{\text{P}} \text{cm}^{-3}$ in both simulations lies in between the thresholds. Thus, in M5IF4pk1 the pressure of the ionized gas is high enough to compress even the densest structures, whereas in M5IFwarm several regions are able to resist the compression. Therefore, the ionized 'valleys' are not expanding significantly in the tangential direction, the density is not lowered as much and the ionization is not able to reach much further. At the same time the un-ionized 'hills' are less compressed, but since they are closer to the front they are accelerated more strongly in the x-direction and the initial differences in the front position are leveled out.

In general, the formation of pillars depends critically on whether the density contrast between the dense regions (ρ_{high}), which will not get ionized, and the less dense regions (ρ_{low}), which will get ionized, is higher than the temperature difference between ionized and un-ionized gas. By defining the density contrast in the initial conditions as $\Delta\rho_{\text{init}} = \rho_{\text{high}}/\rho_{\text{low}}$ and taking into account Eq. 6.15 the critical criterion for the formation of pillars can be written as:

$$\Delta\rho_{\text{init}} \leq \frac{2T_{\text{ion}}}{T_{\text{nion}}}. \quad (6.17)$$

As stars will only form in compressed regions, e.g. pillars, this gives an estimate if a region will undergo triggered star formation.

Unfortunately there is no straightforward way to define the density contrast in a turbulent medium, especially since the impinging flux plays a major role in defining 'high' and 'low' density. However, Eq. 6.17 already shows, that increasing the mean density $\bar{\rho}$ while keeping the temperature constant will not help to hinder the formation of pillars. The only way to change the density contrast is to increase the level of turbulence (see §6.3.5).

6.3.4 Initial Flux and Density

In the next test we vary the impinging photon flux. As in the simulations performed in §6.2.2, the flux is able to ionize immediately 0.55%, 1.67% and 5% of a medium at a constant density of $\rho = 300 m_{\text{P}} \text{cm}^{-3}$ in M5LF4pk1, M5IF4pk1 and M5HF4pk1, respectively. The evolution of the density in the hot component is shown in Fig. 6.3. Although the medium is highly turbulent Eq. 6.10 still gives a very good estimate of this density, especially after an initial phase. Only the case with the high flux differs from the analytical solution. This can be understood as Eq. 6.4 depends on both the penetration depth and the density of the ionized gas. A higher flux can

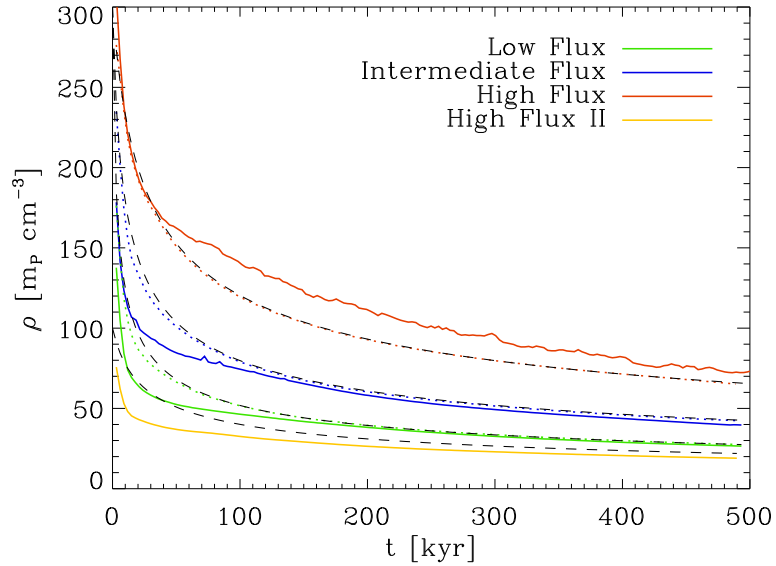


Figure 6.3: The change of the mean density in the hot gas during the simulated time. Solid lines: green M5LF4pk1, blue M5IF4pk1, red M5HF4pk1 and yellow M5LF-n100. Dotted lines: the comparison simulations of §6.2.2 at the respective flux. Dashed black lines: the analytical solution according to Eq. 6.4 with $f = \frac{5}{4}$

ionize denser regions and thus the evolution of M5HF4pk1 would be better described by ionizing a medium at a higher density with a smaller penetration length. On average the turbulent case is still comparable to the case with a constant flux and it is still valid to describe the evolution of the density inside a HII region by Eq. 6.10.

On a more morphological side, the pillars in the simulations with a higher flux (i.e. in a simulation closer to the source) are smaller (Fig. 6.2 panel 6, panel 1 and panel 5 in decreasing flux order). In addition, they gain more momentum away from the source. At the same time the density of the hot gas is higher, leading to denser, more compressed structures with a smaller diameter. Due to the higher photo-evaporation their masses are lower (see Table 6.2).

Changing the initial flux is expected to be similar to changing the mean density. According to Eq. 6.2 $\rho \propto x^2$. In M5LF-n100 we reduced the impinging flux by a factor of three. At the same time we reduced the flux by a factor of three to avoid an extremely high level of ionization degree. In total, this corresponds to the same penetration length as in M5HF4pk1. Thus, we expect a similar morphology to evolve, but the densities should be lower. In Fig. 6.2 (panel 7) this can be clearly seen. The morphology is similar to M5HF4pk1, although the front is less displaced. Again, the density (Fig. 6.3) in the hot gas evolves similarly to the expectation for a homogeneous medium. The mass assembled in the prominent structure (Table 6.2) is lower and the density of the structure fits the findings of pressure equilibrium.

Combining these findings with the results of §6.3.1 allows us to make an interesting prediction. As the density of the hot gas behaves similar to the case of a homogeneous medium and as

the structures are near the pressure equilibrium, we can predict the density of the structures from the initial mean density of the medium, the flux of the source, and the time since the ignition of the source or the position of the ionization front.

6.3.5 Turbulent Mach Number

Another purpose of this study is to disentangle the effects of the initial turbulent density distribution on the formation of the pillars. Therefore, the level of turbulence is changed. We take the decaying turbulent setup at an earlier time, corresponding to Mach 7 in M7IF4pk1 and at a later time, corresponding to Mach 2 in M2IF4pk1. When non-driven turbulence decays, most power is lost on the large scale modes. This can be seen in Fig. 6.2 - in M7IF4pk1 (panel 10) the surface density is clearly dominated by the large modes, which form the prominent fingers. In contrast, in M2IF4pk1 (panel 9) this mode has decayed much further, thus showing no significant preferred location of the structures forming and producing fingers much smaller in the x-direction. However, as seen from the numbers in Table 6.2 the different initial density contrast and average velocity are not significant enough to alter the assembled mass or density of the structures significantly, since the evolution is mainly dominated by the pressure differences between hot and cold gas, which are much higher than the different initial conditions in the simulations varying the Mach number.

6.3.6 Turbulent Scale

To study the effect of the turbulent input scale the initial turbulence, which is usually set up with power on only the largest scales $k = 1..4$, is set up with power on the smaller scales $k = 4..8$ in M5IF4pk4. The resulting surface density in the first 2pc facing the star is shown in Fig. 6.4. Already in the initial conditions (left column) a clear difference can be seen. Whereas the power on the larger k modes leads to large, distinct structures (top panel), power on the smaller modes show already a much more diversified density distribution (lower panel). After $t_{\text{final}} = 500\text{kyr}$ (right column) the ionization leads to an enhancement of the preexisting structure. The densest filaments survive, while the other material is swept away by the ionization. In M5IF4pk1 (top panel) this leads to an excavation of the few, but bigger structures and thus to the creation of few, but distinct pillars. On the other hand, in M5IF4pk4 (bottom panel) more structures, but of smaller scales survive, which leads to several, but tiny structures.

Together with §6.3.5 this shows, that only a strong enough turbulent driving on a large enough driving $k = 1$ mode leads to a overall enhancement to produce the significant structures seen in observations. As has been shown in §6.3.2 this is not an effect of the resolution. The turbulence is well enough resolved to allow for small enough modes to produce fuzzy structure in M5IF4pk1, but the evolution under the influence of UV-radiation is dominated by the larger modes.

Another possibility to change the input scale of the turbulence is to simply increase or decrease the size of the simulation domain. In M5IF8pk1 the domain is doubled. Since the particle number is kept constant, this leads to a factor of two lower spatial resolution. So the resolution in the part of the domain shown in Fig 6.2 (panel 12) is comparable to the low resolution case M5IF-lr (panel 2). M5IF2pk1 has a two times smaller size than the standard case (M5IF4pk1),

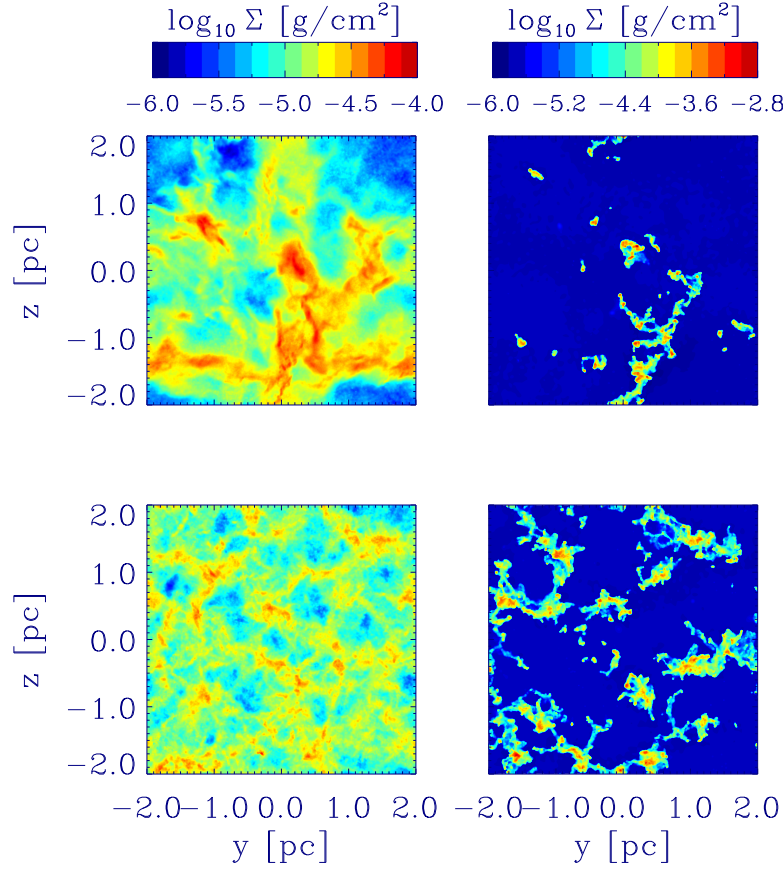


Figure 6.4: Projected surface density along the x-axis. The projected slice is always 2 pc thick. Left: $t = 0$ kyr and the slice starts at the surface facing the O-star, right: 500 kyr and the slice is adjusted to encompass the substructures. Top row: only modes $k = 1 - 4$ are populated initially, bottom row: only modes $k = 4 - 8$ are populated initially.

which corresponds to doubling the spatial resolution. The domain has a smaller extend in the x-direction as well, which we compensate by taking two times the evolved turbulence in the x-direction. This is valid, since the initial conditions were evolved with periodic boundary conditions. The particle number is thus 4×10^6 , twice as high as in most other cases.

As the density distribution and therefore the density contrast is self-similar in all three cases we expect that the same regions of the initial conditions will form the dominant structures. Only the size of the encompassed region and therefore the size and mass of the pillars should change. In Fig. 6.2 all three simulations (panel 1, panel 11, panel 12) show a clear sign of the largest $k = 1$ mode. The size of the structures formed is linearly dependent on the initial box-length or size of the largest k-mode. In fact M5IF2pk1 is somewhat the situation in between M5IF4pk1 and M5IF4pk4, as the largest mode is 2 pc, which corresponds to a $k = 2$ mode in a 4 pc domain. The values of Table 6.2 confirm the importance of the largest mode. In the assembled structures the estimated diameters are roughly a factor of two different and the masses vary by a factor of four.

Simulation	$t_{\text{form}}[\text{kyr}]$	$M[M_{\odot}]$	$v_x[\text{km s}^{-1}]$	$x[\text{pc}]$	$y[\text{pc}]$	$z[\text{pc}]$	Name
M5IF8pk1	305.3	0.86	4.37 ± 1.4	-2.83	-1.84	1.26	Nanni
M5IF8pk1	353.3	0.90	4.16 ± 0.7	-2.60	-1.86	1.34	Vreni
M5IF8pk1	403.7	0.78	4.53 ± 1.1	-2.58	0.29	0.41	Lilli
M5IF8pk1	469.3	0.83	4.99 ± 0.7	-2.06	-1.88	1.48	Steffi
M5HF4pk1	429.5	0.57	11.27 ± 1.0	1.86	-1.05	0.64	Jasmin
M5IF4pk1	493.3	0.72	3.92 ± 0.8	0.19	0.48	-0.79	Anna

Table 6.3: Listing of the proto-stellar cores forming in the different simulations. Given are mass, formation time, average speed away from the source and the formation position as well as the names we gave them.

This is as expected since the regions initially encompassed by the radiation should differ by a factor of two in the y- and the z-direction.

Taking this results on the turbulent scale into account, we conclude that the mass and size of the pillars depends directly on the input scale of the turbulence, e.g the size of the driving process or the size of the preexisting molecular cloud. On average, the most prominent structures in our simulations with an intermediate flux are $d_{\text{pil}} \approx \frac{1}{40}x_{\text{turb}}$, where x_{turb} is the largest turbulent input mode⁶.

6.3.7 Star Formation

In several simulations triggered dense regions form cores and are driven into gravitational collapse. Since star formation is not the main goal of this study we do not replace them by sink particles. Instead we remove the particles forming a core from the simulation to avoid a considerable slowdown of the calculation. Following G09a we define a core as all gas with a density above $\rho_{\text{crit}} = 10^7 m_{\text{p}} \text{cm}^{-3}$ in the region around the density peak and remove the particles representing this core. This core formation is not a numerical effect, since the resolution limit as given by Bate & Burkert (1997) is $\rho_{\text{num}} = 3 \times 10^8 m_{\text{p}} \text{cm}^{-3}$ in the lowest resolution case. We give the simulation, mass⁷, formation time, average speed away from the source and positions in Table 6.3. If we assume the cores to be decoupled from the rest of the cold gas then their position at the end of the simulation can be estimated by this values. All of them are still close to the prominent structures, some of them are traveling further inside the structures, some are lagging behind and would by now be slightly outside of the pillar, closer to the source.

As it can be expected in M5IF8pk1, where the compressed structures are most massive, star formation is most frequent and happens early. There is an age spread visible as well - the earlier a core forms the closer to the source it will be. The other simulations where cores form during the first 500kyr after the ignition of the O star are M5HF4pk1 and M5IF4pk1. The higher flux

⁶In fact the value for M5LF-n100 from Table 6.2 does not match precisely, but from Fig. 6.2 the factor of ≈ 4 between M5IF4pk1 and M5LF-n100 can be seen.

⁷The masses do not differ significantly, as we do not follow the further accretion process and at the moment of formation the cores are still similar.

in M5HF4pk1 leads to a higher compression and thus an earlier formation of a core. This core is less massive and moves faster compared to the core in M5IF4pk1.

Altogether, triggered star formation is very likely in this scenario. The cores form at the center of the structures, but since their velocities differ from the velocity of their parental structure they can be decoupled and either wander further into the trunk or lag behind. At the time they become observable there might be no clear correlation to their birthplace any more.

6.4 Comparison to Observations

6.4.1 General Properties

The first quantity we want to compare to observations is the density of the hot gas. Lefloch et al. (2002) estimate the electron density of the HII-region in the Trifid Nebula from OIII as $n_e = 50 \text{ cm}^{-3}$. In a fully ionized region this corresponds directly to the density given in Table 6.2, since $n_e = n_H = \rho/m_p$. Thus, the observed value is very similar to all simulations with an intermediate flux at $t = 500 \text{ kyr}$.

For the column density of the dense core they estimate $N(\text{CS}) \approx 1.8 \times 10^{13} \text{ cm}^{-2}$, which corresponds to $\log_{10}[N(\text{H}_2)/\text{cm}^{-2}] \approx 22.5$ with their given conversion factor. As our simulations are performed with atomic hydrogen we need to convert the surface density in the cold gas into a column density. With a hydrogen abundance of $X = 0.7$ and the assumption that at this densities all hydrogen is molecular the conversion factor is $\chi = N(\text{H}_2)/\Sigma = 0.35$. The resulting values are given in Table 6.2 and are $\log_{10}[N(\text{H}_2)/\text{cm}^{-2}] \approx 20.5$ in all cases where structures form. As this is the averaged surface density of the entire structure it is two orders of magnitude lower than the observed values. In the tips of the pillars (see e.g. Fig. 6.5) the peak surface density is $\log_{10}[\Sigma_{\text{max}}/(\text{g cm}^{-2})] = -1.2$ which leads to a column density $\log_{10}[N(\text{H}_2)/\text{cm}^{-2}] = 22.12$, which is in good agreement with the observation. Thompson et al. (2002) estimate $\log_{10}[N(\text{H}_2)/\text{cm}^{-2}] \approx 21.3$ for the most prominent of the pillars in M16. In RCW 120 (e.g. Deharveng et al., 2009) condensation 4 seems to be a good candidate for triggered star formation. The peak surface density is $\log_{10}[N(\text{H}_2)/\text{cm}^{-2}] = 22.15 - 22.49$. In addition, Urquhart et al. (2009) look at a sample of 60 bright rimmed clouds and find the column densities in cases of triggered star formation (that is in the cases with photodissociation regions (PDRs)) to be $\log_{10}[N(\text{H}_2)/\text{cm}^{-2}] = 20.9 - 22.8$.

As all these observations match our simulations, we conclude that the evolution of the density of the hot gas is in good approximation given by the estimate in the case of a homogeneous medium (Eq. 6.10). Furthermore, since the densities of the compressed structures are reproduced as well, we can assume that the structures are indeed in pressure equilibrium with the hot, surrounding gas. This gives a the fantastic opportunity to determine the density in the hot gas and in the compressed structures directly from the initial mean density, the flux from the source and the time since the ignition of the source or the position of the ionization front.

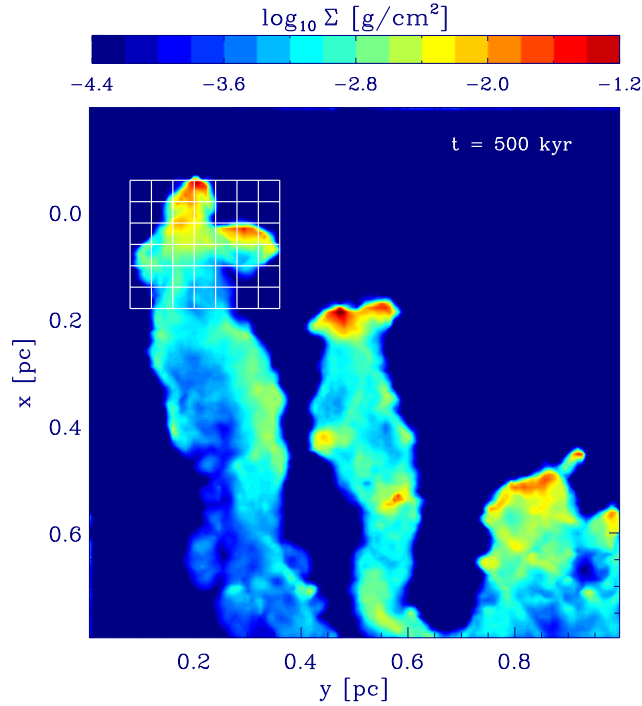


Figure 6.5: Surface density of the most prominent structures in M51F4pk1. The simulation is rotated to enable a more direct comparison to the observation. The white squares denote the regions where the line-of-sight velocities and the velocity fields are taken.

6.4.2 Velocity Field of a Singular Pillar

Another very interesting property to compare between simulations and observations are the details of the velocity distribution. Since turbulence in general is a highly complex process it is not possible to precisely predict the outcome of simulations. Therefore, we do not set up a simulation to match some specific observation but instead start with realistic ICs and then look for an observed counterpart of the outcome of our simulation. For the main pillar in M51F4pk1 the Dancing Queen (DQ) trunk in NGC 7822 as observed by Gahm et al. (2006) looks promising, in shape as well as in the mass range. The authors give the diameter as $d_{\text{obs}} \approx 0.12 - 0.15 \text{ pc}$, the total estimated mass from ^{12}CO is $M_{\text{obs}} \approx 9.2 M_{\odot}$. This fits nicely with the simulated pillar ($d_{\text{sim}} \approx 0.12 \text{ pc}$, $M_{\text{sim}} \approx 12.6 M_{\odot}$, see Table 6.2). If we subdivide the pillar into a head (indicated by the white grid in Fig. 6.5) and a body the mass splits up into $M_{\text{head,s}} \approx 7.2 M_{\odot}$ and $M_{\text{body,s}} \approx 5.3 M_{\odot}$ (compared to $M_{\text{head,o}} \approx 5.7 M_{\odot}$ and $M_{\text{body,o}} \approx 3.5 M_{\odot}$ in the DQ trunk).

To enable a more detailed comparison we defined a grid across the head in the y-x plane (see Fig. 6.5), which is set up to resemble the beams along which the line-of-sight (LOS) velocity is taken. We divide the LOS-velocity, ranging from $v_z = -4 \text{ km s}^{-1}$ to $v_z = 4 \text{ km s}^{-1}$ into 80 equally sized bins. In each of the velocity bins the mass is integrated. Fig. 6.7 shows the profiles obtained in that way. As these profiles do not take any radiative transfer, temperature dependencies or chemistry into account they are not as symmetric as the observed HCO^+ profiles (Fig. 6.8). Nevertheless, the similarities are striking. First of all, the line-width is comparable and thus the

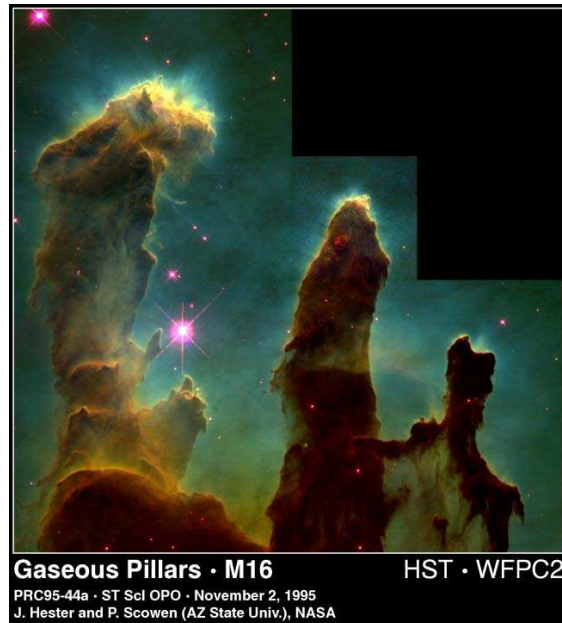


Figure 6.6: To enable a better comparison with the observations, the HST picture of M16 is shown again. The scale is approximately the same as in Fig. 6.5, as the length of pillar I in M16 is ≈ 1 pc. Image credit: J. Hester & P. Scowen, NASA.

velocities are similar, our simulations are just missing the offset of $v_0 \approx -16.4 \text{ km s}^{-1}$, the speed at which the observed DQ is moving with respect to us. In addition, the profile is reminiscent of a rotational pattern, as the peak is shifting from left to right, as well as a gradient along the x-direction, since the peak is shifting from top to bottom. This so called 'corkscrew' pattern has often been attributed to magnetic fields. However, our simulations without magnetic fields are providing an intriguingly similar pattern. It might well be that the misalignment of the magnetic fields with the pillars found by (Sugitani et al., 2007) in M16 indicates the lesser importance of magnetic fields in the formation of pillars as well. When looking at the projection rotated by 90° , the z-x plane, the situation is changed (Fig. 6.9). The profiles along the v_y -LOS-velocity still show the observed line-width but no significant shifting of the peaks can be discovered. To investigate if the rotation of the pillar is a mere projection effect we take a deeper look at the true velocity fields in the y-z plane. Fig. 6.10 shows the v_y - v_z velocity-field averaged in the slices along the x-direction indicated in Fig. 6.5. Here, it can be very clearly seen that there is no distinct rotational pattern. Instead, the motion consists of a complex combination of several flows. The main current is streaming along the surface, thus producing a rotation like signature in some projections. The true origin of these streams producing the pseudo-rotation are most probably remnants of the turbulent initial flows which get deflected at the surface by the pressure of the surrounding hot gas.

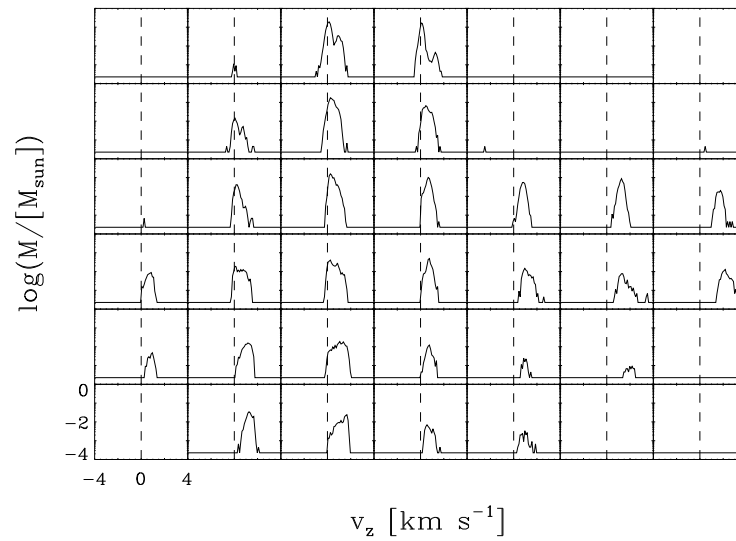


Figure 6.7: Line-of-sight velocities in the different segments shown in Fig. 6.5. Plotted is the mass inside each z -velocity bin against the z -velocity v_z .

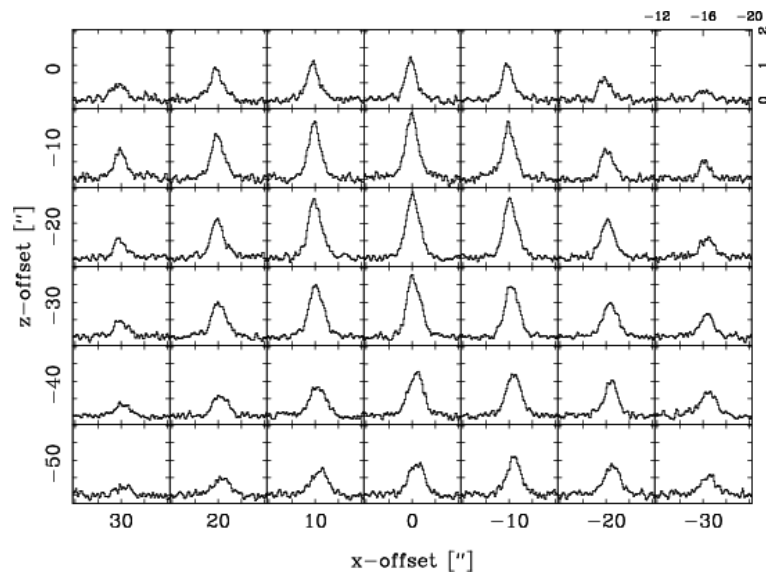


Figure 6.8: Map of HCO^+ profiles over the head of the Dancing Queen Trunk in NGC 7822 as observed by Gahm et al. (2006, their Fig. 7).

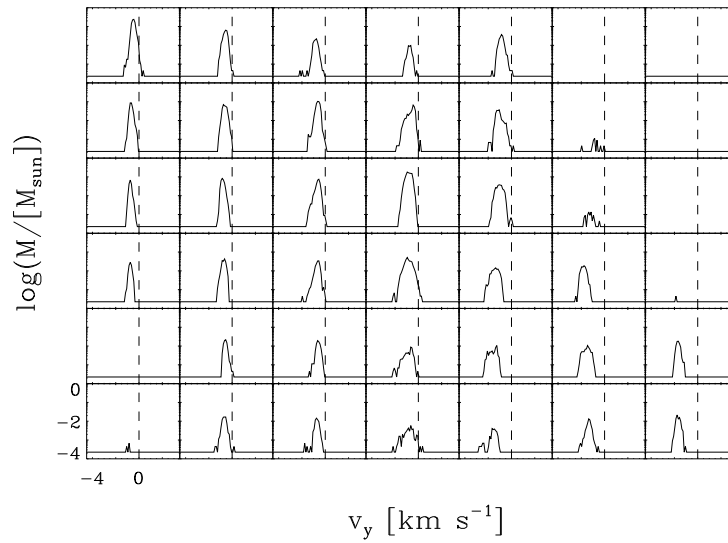


Figure 6.9: Line-of-sight velocities in the different segments in the z - x plane, chosen according to the ones in Fig. 6.5. Plotted is the mass inside each y -velocity bin against the y -velocity v_y .

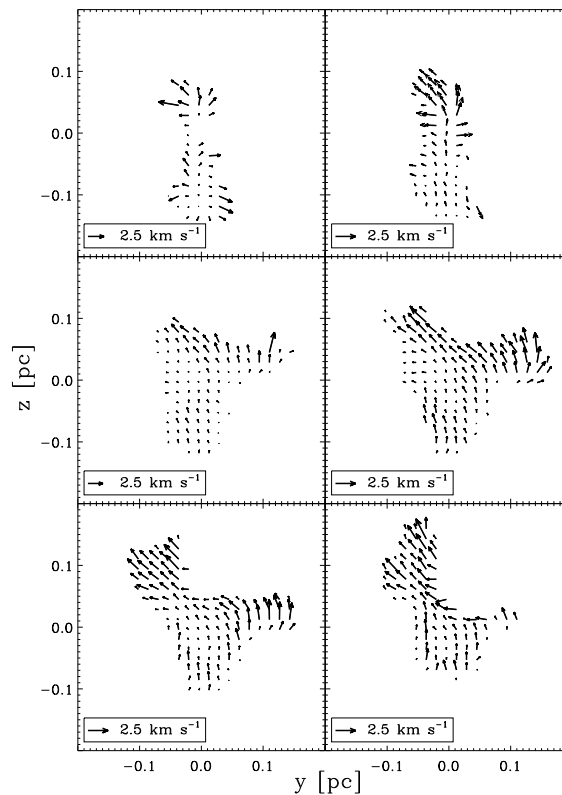


Figure 6.10: Velocity field in the y - z plane. The velocities are taken in the slices in the x -direction indicated in Fig. 6.5

6.5 Discussion

We perform a wide range parameter study on the influence of ionizing radiation on the turbulent ISM with iVINE, a tree-SPH code including ionization. First we show that our simulations are converged and the choice of boundary conditions does not affect the outcome significantly. The results of the parameter study match the observations, in shape, mass assembly, density range and velocity profiles closely. We thus conclude:

1. The formation of any structures depends critically on the initial density contrast. Structures and therefore stars only form if the density contrast is greater than the temperature contrast between the hot and the cold gas: $\Delta\rho_{\text{init}} \leq \frac{2T_{\text{ion}}}{T_{\text{nion}}}$ (see §6.3.3).
2. The evolution of the ionized mass, density and the front position in a turbulent medium under the influence of different initial fluxes is remarkably similar to the evolution in a homogeneous case. Thus, the size and density inside a HII-region solely depends on the initial flux, density and the time since the ignition of a star or the distance from the star and follows the simplified analytical prescriptions(see §6.3.4).
3. The density of the resulting pillars is determined by a pressure equilibrium between the hot and the cold gas. Therefore, the expected density of the structures can be calculated as well (see §6.3.1).
4. Varying the turbulent Mach number between 2 – 7 changes the morphology. The higher the Mach number, the more prominent the structures are. However, it does not alter the physical quantities such as the mass assembled and the column density significantly (see §6.3.5). The formation of structures depends mainly on the temperature difference between the two gas phases.
5. The size of the structures evolving depends critically on the driving modes of the turbulence. Smaller driving modes lead to smaller structures. In our simulations the relation is roughly $d_{\text{pil}} \approx x_{\text{driving}}/40$ (see §6.3.6).
6. Core and star formation is likely to occur. The higher the mass in the structures and the higher the initial flux, the earlier cores form (see §6.3.7).

Combining 2. and 3. allows us directly to determine the density of the forming structures as

$$\rho_{\text{pillar}} \approx \frac{2T_{\text{ion}}}{T_{\text{nion}}} \rho_{\text{ion}} \approx \frac{2T_{\text{ion}}}{T_{\text{nion}}} \rho_0 \left(1 + \frac{5}{4} \frac{c_{\text{s,hot}}}{x_{\text{s}}} (t - t_0) \right)^{-\frac{2}{5}}, \quad (6.18)$$

where x_{s} depends on the initial density and the impinging flux.

Of course one has to keep in mind that this is still a simplified approach. First of all, no scattering is taken into account. Once a electron recombines, the emitted photon is assumed to be absorbed in the direct neighborhood (on the spot approximation). Thus, the reheating of shadowed regions by the adjacent hot gas is not taken into account. In addition, we focus on

atomic hydrogen only, which makes it impossible to follow the precise temperature evolution as well as the photodissociation regions (PDRs). On the other hand, our simulations indicate, that the pillars are in pressure equilibrium with the hot gas. Therefore, the PDRs might be transition regions comparable to a thin shock layer which is not resolved. Furthermore, we do not take magnetic fields into account. These might have implications on the global shapes of the HII region (see e.g. Krumholz et al., 2007). Nevertheless, we are able to reproduce the cork-screw morphologies in the pillars which were up to now attributed to magnetic fields (see §6.4.2). Another aspect we neglect are stellar winds. Up to now it is still unclear how the fast winds of a massive star affect its surroundings. From our simulations we would estimate that stellar winds are of minor importance, maybe mainly enhancing the shock front as soon as a lower density in the hot gas enables the effective driving of winds.

Altogether, our simulations are able to reproduce almost all observed quantities. Besides, they give a deeper insight on the tight correlation between the parental molecular clouds size, density and turbulence and the structures excavated by the ionizing radiation. The ionization acts as a magnifying glass, revealing the condition of the molecular cloud previous to the ignition of the massive star.

Acknowledgements

This research was founded by the DFG cluster of excellence 'Origin and Structure of the Universe'. All simulations were performed on a SGI Altix 3700 Bx2 supercomputer that was partly funded by the DFG cluster of excellence 'Origin and Structure of the Universe'.

Chapter 7

Conclusions and Outlook

In this thesis a new, highly efficient, parallel implementation of ionizing radiation in the tree-SPH code VINE is presented. SPH is a Lagrangian method, which renders it extremely suitable to cover several orders of magnitude in density as well as in spatial scale. An adaptive spatial resolution is crucial, since the process of the formation of pillars and young stellar objects from the initial molecular cloud (MC) covers at least ten orders of magnitude in density. Ionizing radiation was implemented in the VINE code in a highly portable way, which can be easily implemented into any other SPH code. The effect of ionization is included under the assumption of plane-parallel irradiation, which is valid as long as the simulated volume is far enough away from the source of radiation. This approach allows for simulations at, up to now, unmatched high resolution. As the radiation is impinging, the simulation volume is decomposed in equally spaced subregions or rays, along which the ionization is then calculated. Each of these rays can be refined up to eight times, leading to a typical spatial resolution of the radiation as high as 10^{-4} pc in our simulations. The new implementation is fully parallelized and is called iVINE (Ionization+VINE).

As we aim for a deeper understanding of the main effects of ionization and do not try to reproduce a specific observation, we include a number of simplifications. The optical depth and thus the ionization degree is calculated under the assumption of a monochromatic flux. Furthermore, scattering of photons from one ray to another and collisional ionizations of hydrogen are neglected as they should only give minor contributions compared to the flux from an O star. In addition, we assume the gas to be purely consisting of hydrogen. This is a natural simplification, as hydrogen is the most abundant element in the universe. On the other hand, this neglects the absorption of ionizing photons by heavier elements and dust. Thus, our simulations provide an upper limit for the efficiency of ionization. Nevertheless, since the simulated area is further away from the star, this could also be corrected by placing the simulated volume closer to the star or increasing the flux of the star. The maybe most important simplification is the 'On-The-Spot'-approximation. Any photons emitted by recombinations of electrons and protons are assumed to be absorbed in the immediate surrounding again. This neglects the indirect heating of the pillar-like substructures by the adjacent hot gas. Besides, any hot gas moving in the shaded region is assumed to cool instantaneously to the temperature of the cold gas. Another simplification is the negligence of the magnetic field. This is due to the fact that it is very complex to calculate

a field on the moving integration grid as provided by SPH. The first steps of an inclusion of magnetic fields into SPH have been done, but a successful treatment for the highly dynamical situation in HII regions has yet to be implemented. On the physical side, grid-code simulations with magnetic fields show that this fields have no strong effect on the small-scale structures, if any. Altogether, we present a simplified prescription of ionizing radiation which avoids the inclusion of physics like dust absorption, since this would introduce new free parameters (e.g. a dust absorption coefficient and a gas-to-dust ratio).

First, the correct behavior of the algorithm is ensured by several analytical tests (§4). Then, the radiation driven implosion of preexisting MCs is studied. These are parameterized by marginally stable Bonnor-Ebert spheres (BES). Three different simulations are performed. They are distinguished by the impinging initial UV-flux, corresponding to placing the BES either inside or at the border or outside of the Strömgren radius, respectively. In all simulations an elongated, pillar-like filament evolves with a collapsing core being close to the ionization front, as it is observed. A clear trend can be seen: the higher the initial UV-flux, the earlier the filament forms and the earlier the core collapses ($t_{\text{collapse}} = 200 - 600 \text{ kyr}$, $M_{\text{core}} = 2.8 - 7.4 M_{\odot}$). In the velocities of the cores the same trend is visible. Cores forming in a simulation with a higher flux obtain a higher radial velocity away from the source of radiation ($v_{\text{core}} = 5.1 - 8.4 \text{ km s}^{-1}$). However, in the core masses no such trend is visible. Altogether, this shows that the radiation driven implosion of preexisting stable BES can very well reproduce singular filamentary structures.

Another approach is suitable to explain the formation of multiple filamentary structures like the pillars of creation in M16 (§5). To mimic the observed turbulence, a highly supersonic velocity field (Mach 10) with a turbulent power-law is set up. This setup is allowed to decay freely under the influence of hydrodynamics. After $\approx 1 \text{ Myr}$ a Kolmogorov-like power-law has evolved on all resolvable scales. The velocities now correspond to Mach 5. When exposing this setup to ionizing radiation, the ionization can penetrate much deeper into the regions of lower density. These regions then exert pressure on the adjacent cold gas, which is compressed into pillar-like substructures and a morphology remarkably similar to the pillars of creation evolves after $t = 500 \text{ kyr}$. At the tip of the pillars gravitational collapse occurs ($M_{\text{core}} \approx 0.7 M_{\odot}$). We like to call this process 'radiative round-up'. When comparing the turbulent spectra in the rear part of the simulation box (further away from the ionization front) to a control run without ionization a clear effect can be seen. In the control run the turbulence decays freely. In contrast, turbulence is driven in the cold gas at all resolvable scales, when ionization is included. This leads to a final kinetic energy that is an order of magnitude higher than in the control case and suggests a very effective mechanism to sustain turbulence in MCs. In this simulation, the efficiency of driving the turbulence by ionizing radiation is one order of magnitude higher than it was previously estimated by analytical calculations.

To disentangle the effects of different initial conditions we perform an entire parameter study (§6). The fiducial setup explained above is compared to several other simulations with different temperatures, Mach numbers, incident flux, levels of turbulence and turbulent scales. In almost all simulations pillars are formed after $t = 500 \text{ kyr}$. Their densities are of the order of $\rho \approx 5 \times 10^5 \text{ cm}^{-3}$, the corresponding H_2 column density is $\log_{10}[N(\text{H}_2)/\text{cm}^{-2}] \approx 20.5$, which is similar to the observations. The only way to hinder the formation of these structures is increasing the temperature of the cold gas, thus lowering the pressure difference between the hot and the cold

gas. If pillars form, they are in rough thermal equilibrium with the hot surrounding gas. As a consequence, the structures in simulations with higher flux are smaller because the density in the hot gas is higher. Furthermore, the size of the structures depends linearly on the input scale of the turbulence. The largest structures form in the simulation with the largest driving mode. Gravitational collapse is detected frequently and is in agreement with the observed age-spread. In the case of higher flux the core forms earlier, is less heavy and moves away faster from the source than in the case of intermediate flux ($t_{\text{high}} \approx 430 \text{ kyr}$, $M_{\text{high}} = 0.6 M_{\odot}$, $v_{\text{high}} \approx 11 \text{ km s}^{-1}$ and $t_{\text{im}} \approx 494 \text{ kyr}$, $M_{\text{im}} = 0.7 M_{\odot}$, $v_{\text{im}} \approx 3.9 \text{ km s}^{-1}$). In addition, the density in the hot gas in the turbulent case is on average the same as given by analytical predictions for the homogeneous case. This gives the unique opportunity to predict the size, density and number of structures from the initial properties of the molecular cloud. Of course, this can be used backwards in time and enables us to estimate the original size (i.e. the driving scale of the turbulence) as well as the original mean density of the MC from the time since the ignition of the O star, the density and amount of structures as well as the flux of the star.

As a next step in the future, the predictive power of the model described above could be tested with further simulations. In addition, there is still more information to be obtained from the simulations. The cores in the simulations form at the tip of the structures. They all show disk-like accretion features. Initially, they seem to be aligned with the pillars. This corresponds to the observations, which show jets of newly born stars perpendicular to the pillar. However, these disks form very close to the resolution limit of our simulations. Therefore, we will perform simulations with an even higher resolution in the future to follow this process precisely. Future improvements of the code will include a more precise treatment of the balance of heating and cooling, especially the cooling of hot gas, which gets shaded by the tips of the pillars. This could be done by using an adiabatic equation of state in combination with a cooling function. Furthermore, the implementation of point sources was already started and will be further optimized in the future. This will enable us to put the high resolution simulations presented in this thesis into the context of the entire HII region. After that, the next step could be the implementation of stellar winds into SPH.

Bibliography

- Agertz, O. et al. 2007, MNRAS, 380, 963
- Altay, G., Croft, R. A. C., & Pelupessy, I. 2008, MNRAS, 386, 1931
- Andersen, M., Knude, J., Reipurth, B., Castets, A., Nyman, L. Å., McCaughrean, M. J., & Heathcote, S. 2004, A&A, 414, 969
- Attwood, R. E., Goodwin, S. P., & Whitworth, A. P. 2007, A&A, 464, 447
- Ballesteros-Paredes, J., Hartmann, L., & Vázquez-Semadeni, E. 1999, ApJ, 527, 285
- Bate, M. R., & Burkert, A. 1997, MNRAS, 288, 1060
- Benz, W. 1990, in Numerical Modelling of Nonlinear Stellar Pulsations Problems and Prospects, ed. J. R. Buchler, 269+
- Benz, W., Cameron, A. G. W., Press, W. H., & Bowers, R. L. 1990, ApJ, 348, 647
- Bertoldi, F. 1989, ApJ, 346, 735
- Bisbas, T. G., Wunsch, R., Whitworth, A. P., & Hubber, D. A. 2009, A&A, 497, 649
- Bodenheimer, P., Laughlin, G. P., Rózycka, M., & Yorke, H. W., eds. 2007, Numerical Methods in Astrophysics: An Introduction. (Taylor Francis Group, Boca Raton, FL USA, 2007.)
- Bonnor, W. B. 1956, MNRAS, 116, 351
- Bowler, B. P., Waller, W. H., Megeath, S. T., Patten, B. M., & Tamura, M. 2009, AJ, 137, 3685
- Carroll, B. W., & Ostlie, D. A. 2006, An introduction to modern astrophysics and cosmology (San Francisco: Pearson Addison Wesley)
- Chauhan, N., Pandey, A. K., Ogura, K., Ojha, D. K., Bhatt, B. C., Ghosh, S. K., & Rawat, P. S. 2009, ArXiv e-prints, arXiv:0903.2122
- Comerón, F., & Schneider, N. 2007, A&A, 473, 149
- Dale, J. E., Bonnell, I. A., Clarke, C. J., & Bate, M. R. 2005, MNRAS, 358, 291

- Dale, J. E., Bonnell, I. A., & Whitworth, A. P. 2007a, MNRAS, 375, 1291
- Dale, J. E., Clark, P. C., & Bonnell, I. A. 2007b, MNRAS, 377, 535
- Deharveng, L., Zavagno, A., & Caplan, J. 2005, A&A, 433, 565
- Deharveng, L., Zavagno, A., Schuller, F., Caplan, J., Pomarès, M., & De Breuck, C. 2009, A&A, 496, 177
- Dopita, M. A., & Sutherland, R. S. 2003, *Astrophysics of the diffuse universe* (Springer)
- Elmegreen, B. G. 1998, in *Astronomical Society of the Pacific Conference Series*, Vol. 148, *Origins*, ed. C. E. Woodward, J. M. Shull, & H. A. Thronson, Jr., 150–+
- Elmegreen, B. G., Kimura, T., & Tosa, M. 1995, ApJ, 451, 675+
- Elmegreen, B. G., & Lada, C. J. 1977, ApJ, 214, 725
- Elmegreen, B. G., & Scalo, J. 2004, ARA&A, 42, 211
- Fukuda, N., Hanawa, T., & Sugitani, K. 2002, ApJ, 568, L127
- Gahm, G. F., Carlqvist, P., Johansson, L. E. B., & Nikolić, S. 2006, A&A, 454, 201
- Getman, K. V., Feigelson, E. D., Garmire, G., Broos, P., & Wang, J. 2007, ApJ, 654, 316
- Gingold, R. A., & Monaghan, J. J. 1983, MNRAS, 204, 715
- Glover, S. C. O., & Mac Low, M.-M. 2007, ApJS, 169, 239
- Gouliermis, D. A., Henning, T., Brandner, W., Chu, Y.-H., Hennekemper, E., & Hormuth, F. 2007a, ArXiv e-prints, 710, arXiv:0710.1352
- Gouliermis, D. A., Quanz, S. P., & Henning, T. 2007b, ApJ, 665, 306
- Gritschneder, M., Naab, T., Burkert, A., Walch, S., Heitsch, F., & Wetzstein, M. 2009a, MNRAS, 393, 21
- Gritschneder, M., Naab, T., Heitsch, F., & Burkert, A. 2007, in *IAU Symposium*, Vol. 237, *IAU Symposium*, ed. B. G. Elmegreen & J. Palous, 246–250
- Gritschneder, M., Naab, T., Walch, S., Burkert, A., & Heitsch, F. 2009b, ApJ, 694, L26
- Hartmann, L., Megeath, S. T., Allen, L., Luhman, K., Calvet, N., D’Alessio, P., Franco-Hernandez, R., & Fazio, G. 2005, ApJ, 629, 881
- Hester, J. J. et al. 1996, AJ, 111, 2349
- Hillenbrand, L. A. 1997, AJ, 113, 1733

- Ikeda, H. et al. 2008, *AJ*, 135, 2323
- Iliev, I. T. et al. 2006, *MNRAS*, 371, 1057
- Indebetouw, R., Robitaille, T. P., Whitney, B. A., Churchwell, E., Babler, B., Meade, M., Watson, C., & Wolfire, M. 2007, *ApJ*, 666, 321
- Jiang, Z. et al. 2002, *ApJ*, 577, 245
- Kessel-Deynet, O. 1999, PhD thesis, AA(Max-Planck-Institut für Astronomie, Königstuhl 17, D-69117 Heidelberg, Germany)
- Kessel-Deynet, O., & Burkert, A. 2000, *MNRAS*, 315, 713
- . 2003, *MNRAS*, 338, 545
- Kitsionas, S. et al. 2008, ArXiv e-prints, 810, arXiv:0810.4599
- Klein, R. I., Sandford, II, M. T., & Whitaker, R. W. 1980, *Space Science Reviews*, 27, 275
- Kolmogorov, A. 1941, *Akademiia Nauk SSSR Doklady*, 30, 301
- Krumholz, M. R., Matzner, C. D., & McKee, C. F. 2006, *ApJ*, 653, 361
- Krumholz, M. R., Stone, J. M., & Gardiner, T. A. 2007, *ApJ*, 671, 518
- Lada, C. J., Muench, A. A., Rathborne, J., Alves, J. F., & Lombardi, M. 2008, *ApJ*, 672, 410
- Landau, L. D., & Lifshitz, E. M. 1966, *Hydrodynamik* (Berlin: Akademie-Verlag)
- Larson, R. B. 1981, *MNRAS*, 194, 809
- Lee, H.-T., & Chen, W. P. 2007, *ApJ*, 657, 884
- Lee, H.-T., Chen, W. P., Zhang, Z.-W., & Hu, J.-Y. 2005, *ApJ*, 624, 808
- Lefloch, B., Cernicharo, J., Rodríguez, L. F., Miville-Deschênes, M. A., Cesarsky, D., & Heras, A. 2002, *ApJ*, 581, 335
- Lefloch, B., & Lazareff, B. 1994, *A&A*, 289, 559
- Lifshitz, E. M., & Pitaevskii, L. P. 1981, *Physical kinetics* (Oxford: Pergamon Press)
- Lombardi, M., & Alves, J. 2001, *A&A*, 377, 1023
- Mac Low, M.-M. 2007, ArXiv e-prints, 711, arXiv:0711.4047
- Mac Low, M.-M., & Klessen, R. S. 2004, *Reviews of Modern Physics*, 76, 125
- Mac Low, M.-M., Toraskar, J., Oishi, J. S., & Abel, T. 2007, *ApJ*, 668, 980

- Matzner, C. D. 2002, *ApJ*, 566, 302
- McCaughrean, M. J., & Andersen, M. 2002, *A&A*, 389, 513
- Mellema, G., Arthur, S. J., Henney, W. J., Iliev, I. T., & Shapiro, P. R. 2006, *ApJ*, 647, 397
- Miao, J., White, G. J., Nelson, R., Thompson, M., & Morgan, L. 2006, *MNRAS*, 369, 143
- Miao, J., White, G. J., Thompson, M. A., & Nelson, R. P. 2009, *ApJ*, 692, 382
- Monaghan, J. J. 1989, *Journal of Computational Physics*, 82, 1
- . 1992, *ARA&A*, 30, 543
- Monaghan, J. J., & Lattanzio, J. C. 1985, *A&A*, 149, 135
- Motte, F., & André, P. 2001, *A&A*, 365, 440
- Nelson, A. F., Wetzstein, M., Naab, T., & . 2008, *ArXiv e-prints*, 802, arXiv:0802.4253
- O'Dell, C. R., Henney, W. J., Abel, N. P., Ferland, G. J., & Arthur, S. J. 2009, *AJ*, 137, 367
- Oliveira, J. M. 2008, *Star Formation in the Eagle Nebula (Handbook of Star Forming Regions, Volume II: The Southern Sky ASP Monograph Publications, Vol. 5. Edited by Bo Reipurth)*, 599+
- Osterbrock, D. E. 1989, *Astrophysics of gaseous nebulae and active galactic nuclei (University Science Books)*
- Padoan, P., & Nordlund, Å. 1999, *ApJ*, 526, 279
- Pawlik, A. H., & Schaye, J. 2008, *MNRAS*, 389, 651
- Peters, T., Banerjee, R., Klessen, R. S., & Mac Low, M. 2009, in *American Astronomical Society Meeting Abstracts, Vol. 213, American Astronomical Society Meeting Abstracts*, 441.03
- Pomarès, M. et al. 2009, *A&A*, 494, 987
- Press, W. H. 1986, in *Lecture Notes in Physics, Berlin Springer Verlag, Vol. 267, The Use of Supercomputers in Stellar Dynamics*, ed. P. Hut & S. L. W. McMillan, 184+
- Price, D. 2005, *ArXiv e-prints*, arXiv:0507.7472
- Reach, W. T. et al. 2004, *ApJS*, 154, 385
- Sandford, II, M. T., Whitaker, R. W., & Klein, R. I. 1982, *ApJ*, 260, 183
- Scalo, J., Vazquez-Semadeni, E., Chappell, D., & Passot, T. 1998, *ApJ*, 504, 835

- Shu, F. H. 1991a, *Physics of Astrophysics, Vol. I: Radiation* (University Science Books, New York)
- . 1991b, *Physics of Astrophysics, Vol. II: Gas Dynamics* (University Science Books, New York)
- Smith, N., Egan, M. P., Carey, S., Price, S. D., Morse, J. A., & Price, P. A. 2000, *ApJ*, 532, L145
- Snider, K. D., Hester, J. J., Desch, S. J., Healy, K. R., & Bally, J. 2007, *ArXiv e-prints*, 711, arXiv:0711.1515
- Spitzer, L. 1962, *Physics of Fully Ionized Gases* (New York: Interscience (2nd edition))
- . 1978, *Physical processes in the interstellar medium* (Wiley-Interscience, New York)
- Springel, V., Yoshida, N., & White, S. D. M. 2001, *New Astronomy*, 6, 79
- Stanke, T., Smith, M. D., Gredel, R., & Szokoly, G. 2002, *A&A*, 393, 251
- Strömgren, B. 1939, *ApJ*, 89, 526
- Sugitani, K., Fukui, Y., Mizuni, A., & Ohashi, N. 1989, *ApJ*, 342, L87
- Sugitani, K., Fukui, Y., & Ogura, K. 1991, *ApJS*, 77, 59
- Sugitani, K. et al. 2002, *ApJ*, 565, L25
- . 2007, *PASJ*, 59, 507
- Thompson, M. A., White, G. J., Morgan, L. K., Miao, J., Fridlund, C. V. M., & Hultgren-White, M. 2004, *A&A*, 414, 1017
- Thompson, R. I., Smith, B. A., & Hester, J. J. 2002, *ApJ*, 570, 749
- Urquhart, J. S., Morgan, L. K., & Thompson, M. A. 2009, *ArXiv e-prints*, arXiv:0902.4751
- Walborn, N. R., Maíz-Apellániz, J., & Barbá, R. H. 2002, *AJ*, 124, 1601
- Walch, S. 2008, PhD thesis, AA(Universitäts-Sternwarte München, Scheinerstr. 1, D-81679 München, Germany)
- Ward-Thompson, D., Nutter, D., Bontemps, S., Whitworth, A., & Attwood, R. 2006, *MNRAS*, 369, 1201
- Wetzstein, M., Nelson, A. F., Naab, T., & Burkert, A. 2008, *ArXiv e-prints*, 802, arXiv:0802.4245
- Yorke, H. W., Bodenheimer, P., & Tenorio-Tagle, G. 1982, *A&A*, 108, 25
- Zavagno, A., Deharveng, L., Comerón, F., Brand, J., Massi, F., Caplan, J., & Russeil, D. 2006, *A&A*, 446, 171

Acknowledgments / Danksagung

First of all, I would like to thank my supervisor, Andreas Burkert. I guess without your continuous financial support I would have never started a career in astrophysics. In addition, your inspiring and enthusiastic attitude always encouraged me to search for an even more fundamental correlation.

Second, I am very grateful to Thorsten Naab. Thank you for being the perfect mixture between a supervisor and an office mate. Without your help I might still not have published anything.

In addition, I would like to thank

Steffi Walch, who has been one of my best friends and colleagues since the very first day of my studies. I believe I never had such pugnacious albeit rewarding discussions with anyone else. Thank you for making ten years in physics enjoyable.

The Boys, Michael Hilz, Simon Karl and Ludwig Oser not only for providing 'haute cuisine', but also for lunch times to remember. Keep making some noise for the Astroboys!

The Girls, Michaela Hirschmann, Hanna Kotarba, Eva Ntormousi and Rhea Remus for cheering me up whenever I felt a bit less motivated.

Peter Johansson for always listening to my Altix-complaints and simply for being 'the Finn'.

Fabian Heitsch for his support and constructive ideas during the first years of my PhD.

Harald Lesch for inspiring me to start in astrophysics and for all the continuous advice.

Markus Wetzstein for answering thousands of questions about the VINE code.

The entire rest of the CAST group for encouraging group meetings and outings.

Furthermore, I would like to thank everybody else who helped me on my way. First off all my parents, who supported me during my entire life in every possible way. Thank you so much!

The same is true for my sisters, Nanni, Vreni and Lilli. And for my brother-cousin Max - special thanks to you for playing the game (and playing it loud). Thanks to my brother-in-law Dani for his last-minute corrections and to Lukas and Teresa for making me 'proudest uncle alive'. In addition, I would like to thank all my friends, especially Anna for unforgettable nights out, Jasmin for always being there when she is needed, Heidi for being an extra sister, Sabine for tolerating nightly sessions, Andi for providing the sound-track, Ingo for providing the lyrics and the entire 'Teestube' for providing the rhythm of my life. I will definitely miss you all in Beijing!

Last but not least I would like to thank the entire USM for the wonderful working atmosphere, the fruitful coffee breaks and barbecues to remember.

Curriculum Vitae Resume

Matthias Gritschneider

ADDRESS

Matthias Gritschneider
Universitäts-Sternwarte München
Lehrstuhl: Computational Astrophysics
Scheinerstr. 1
D-81679 München
Germany

Doktorand
Email: gritschm@usm.uni-muenchen.de
Telefon: +49-89-2180-5994
Telefax: +49-89-2180-6003

PERSONAL DATA

Date of birth: August, 7th, 1978
Place of birth: Munich, Germany
Nationality: German

EDUCATION

- 2004-2009: PhD Thesis:
Research at the University Observatory Munich, Munich:
"Ionization and Triggered Star Formation in Turbulent Molecular Clouds"
Supervisor: Prof. Dr. Andreas Burkert
- 2004: Diploma in Physics, Ludwig-Maximilians University, Munich
Diploma Thesis research at the University Observatory Munich, Munich
- 2000: Vordiplom in Physics, University of Regensburg, Regensburg
- 1997: High School "Humanistisches Wilhelmsgymnasium", Munich

LANGUAGES

German (native), English (fluent), Spanish (intermediate), Italian (basic)